



**HAL**  
open science

## Goldstone Cosmology

Philippe Brax, Patrick Valageas

► **To cite this version:**

| Philippe Brax, Patrick Valageas. Goldstone Cosmology. 2016. cea-01460119

**HAL Id: cea-01460119**

**<https://cea.hal.science/cea-01460119>**

Preprint submitted on 7 Feb 2017

**HAL** is a multi-disciplinary open access archive for the deposit and dissemination of scientific research documents, whether they are published or not. The documents may come from teaching and research institutions in France or abroad, or from public or private research centers.

L'archive ouverte pluridisciplinaire **HAL**, est destinée au dépôt et à la diffusion de documents scientifiques de niveau recherche, publiés ou non, émanant des établissements d'enseignement et de recherche français ou étrangers, des laboratoires publics ou privés.

# Goldstone Cosmology

Philippe Brax and Patrick Valageas

*Institut de Physique Théorique,*

*CEA, IPhT, F-91191 Gif-sur-Yvette, Cédex, France*

*CNRS, URA 2306, F-91191 Gif-sur-Yvette, Cédex, France*

(Dated: November 28, 2016)

We investigate scalar-tensor theories where matter couples to the scalar field via a kinetically dependent conformal coupling. These models can be seen as the low-energy description of invariant field theories under a global Abelian symmetry. The scalar field is then identified with the Goldstone mode of the broken symmetry. It turns out that the properties of these models are very similar to the ones of ultralocal theories where the scalar-field value is directly determined by the local matter density. This leads to a complete screening of the fifth force in the Solar System and between compact objects, through the ultralocal screening mechanism. On the other hand, the fifth force can have large effects in extended structures with large-scale density gradients, such as galactic halos. Interestingly, it can either amplify or damp Newtonian gravity, depending on the model parameters. We also study the background cosmology and the linear cosmological perturbations. The background cosmology is hardly different from its  $\Lambda$ -CDM counterpart whilst cosmological perturbations crucially depend on whether the coupling function is convex or concave. For concave functions, growth is hindered by the repulsiveness of the fifth force whilst it is enhanced in the convex case. In both cases, the departures from the  $\Lambda$ -CDM cosmology increase on smaller scales and peak for galactic structures. For concave functions, the formation of structure is largely altered below some characteristic mass, as smaller structures are delayed and would form later through fragmentation, as in some warm dark matter scenarios. For convex models, small structures form more easily than in the  $\Lambda$ -CDM scenario. This could lead to an over-abundance of small clumps. We use a thermodynamic analysis and show that although convex models have a phase transition between homogeneous and inhomogeneous phases, on cosmological scales the system does not enter the inhomogeneous phase. On the other hand, for galactic halos, the coexistence of small and large substructures in their outer regions could lead to observational signatures of these models.

PACS numbers: 98.80.-k

## I. INTRODUCTION

The acceleration of the cosmic expansion [1, 2] in the recent past of the Universe could be due to a nearly massless field on large scales. One of the most natural ways of generating such a field is via the breaking of a global symmetry. At energies below the symmetry breaking scale, there are a number of Goldstone modes which are massless [3]. The potential energy of these modes after symmetry breaking is constant and could serve as vacuum energy, i.e. potentially generating the cosmic acceleration [4]. Another large-scale effect of such modes is to modify the way massive bodies interact as the Goldstone modes propagate a new type of fifth force. The residual Abelian symmetry at low energy translates into a shift symmetry of the scalar field which prevents the existence of direct Yukawa interactions between the Goldstone modes and matter, such as  $\frac{\beta}{M_{\text{Pl}}} m_\psi \varphi \bar{\psi} \psi$ . This implies that Goldstone fields evade the stringent tests of extra gravitational forces in the Solar System [5]. On the other hand, effects in extended structures such as galaxy halos for instance are present due to the derivative nature of the coupling of the Goldstone modes to matter.

More generally, models of modified gravity have very different properties depending on the type of couplings between the scalar field and matter. Conformal couplings, i.e. leading to Yukawa interactions to matter,

have been thoroughly investigated and require a screening of fifth-force effects in our local environment [6]. They appear in four different guises, i.e. the chameleon [7–9] and Damour-Polyakov [10] mechanisms, the K-mouflage [11, 12] and the Vainshtein [13] effects. No other mechanism is necessary for models with second-order equations of motion. A fifth mechanism, the ultralocal scenario [14], has been recently introduced whereby the field does not propagate, i.e. there are no derivative terms in its equation of motion therefore going beyond the previous classification. Another coupling called disformal can also be relevant and plays a crucial role in the Horndeski and beyond-Horndeski models [15–17], i.e. the most general field theories of one scalar with second-order equations of motion [18, 19]. These two types of couplings cover almost all the possibilities which have been unravelled by Bekenstein [20]. The most general coupling between matter and a scalar field that preserves Lorentz invariance and causality depends on the Jordan frame metric

$$g_{\mu\nu} = A^2(\varphi, X) \tilde{g}_{\mu\nu} + B^2(\varphi, X) \partial_\mu \varphi \partial_\nu \varphi \quad (1)$$

where  $\tilde{g}_{\mu\nu}$  appears in the Einstein-Hilbert term of gravity, i.e. when the action is written in such a way that the Einstein-Hilbert action is normalized with a constant Planck scale. The disformal term  $B^2(\varphi, X)$  and the conformal one  $A^2(\varphi, X)$  are functions of the field  $\varphi$  and of its kinetic term  $X = -\frac{1}{2} \tilde{g}^{\mu\nu} \partial_\mu \varphi \partial_\nu \varphi$  only. In this paper

we shall concentrate on the kinetic coupling where

$$A(\varphi, X) \equiv A(X), \quad B(\varphi, X) \equiv 0, \quad (2)$$

and assume that the scalar field has no potential term. Hence the full dynamics of the models are solely due to the coupling function  $A(X)$ . This is exactly the setting that can be derived for Goldstone models, i.e. they are equivalent to modified gravity models with the coupling (2) and a constant vacuum energy. As such they offer a relevant and well-motivated scenario where consequences of both the cosmic acceleration and modified gravity can be combined.

These Goldstone models are hardly different from  $\Lambda$ -CDM cosmology at the background level (because the coupling function  $A$  must remain very close to unity, otherwise the dynamics of perturbations would strongly differ from the Newtonian predictions). At the linear perturbation level, models differ according to whether the function  $\ln[A(X)]$  is concave or convex. For concave functions, the growth of structure is hampered by the repulsiveness of the scalar interaction. This would lead to a scenario whereby, below some characteristic mass, larger structures would form first and then smaller ones would appear by fragmentation. On the other hand, for convex functions growth is largely increased on shorter scales. This could lead to a high-redshift phase with a catastrophic over-abundance of small clumps. We use a thermodynamical approach to analyze this possibility and show that this is not the case for models of interest.

The paper is arranged as follows. In section II, we define the models. In section III, we show that at low energy these models are best considered as classical field theories for distances larger than a small cutoff scale. In section IV, we study the models in the Einstein frame whilst the same is done in the Jordan frame in section V. In section VI, we analyze the global solutions of the equations of motion and the formation of defect surfaces in space. In section VII, we introduce explicit models. The stability and validity of the solution is studied in section VIII, the cosmological background and the linear perturbations in section IX, and the spherical collapse in section X. In section XI, we consider the effects of the models on extended dense structures, such as galactic and cluster halos, and the screening of the fifth force in the Solar System. Finally, in section XII we perform an analysis of the thermodynamics of the models that enhance the formation of large-scale structures (i.e. with a convex coupling function). We conclude then and have an appendix on the coupling to fermions

## II. KINETIC CONFORMAL COUPLING

### A. The Models

We consider scalar field models where the action has the form

$$S = \int d^4x \sqrt{-\tilde{g}} \left[ \frac{\tilde{M}_{\text{Pl}}^2}{2} \tilde{R} + \tilde{\mathcal{L}}_\varphi(\varphi) \right] + \int d^4x \sqrt{-g} \mathcal{L}_m(\psi_m^{(i)}, g_{\mu\nu}), \quad (3)$$

where  $\tilde{g}$  is the determinant of the Einstein-frame metric tensor  $\tilde{g}_{\mu\nu}$ , and  $\psi_m^{(i)}$  are various matter fields. The additional scalar field  $\varphi$  is explicitly coupled to matter through the Jordan-frame metric  $g_{\mu\nu}$ , with determinant  $g$ , which is given by the conformal rescaling

$$g_{\mu\nu} = A^2(\tilde{\chi}) \tilde{g}_{\mu\nu}, \quad \text{with} \quad \tilde{\chi} = -\frac{1}{2\mathcal{M}^4} \tilde{g}^{\mu\nu} \partial_\mu \varphi \partial_\nu \varphi. \quad (4)$$

Here  $\tilde{\chi} = X/\mathcal{M}^4$  is the normalized kinetic term of the scalar field, and  $\mathcal{M}^4$  is an energy scale, of the order of the current cosmological energy density, that is a parameter of the model. Throughout this paper we use the signature  $(-, +, +, +)$  for the metric and we denote Einstein-frame quantities with a tilde  $\sim$ , to distinguish them from Jordan-frame quantities (without a tilde).

This model is similar to standard scalar-tensor models, except that the conformal mapping (4) is taken as a function of the derivative term  $\tilde{\chi}$  instead of the scalar field value itself  $\varphi$ . Since in this paper we are interested in the qualitative features associated with this new coupling form, we do not consider the mixed dependence  $A(\varphi, \tilde{\chi})$  and we focus on the  $\tilde{\chi}$ -dependence of the coupling function  $A$ . We also take the scalar field Lagrangian to be governed by its standard kinetic term,

$$\tilde{\mathcal{L}}_\varphi(\varphi) = -\frac{1}{2} \tilde{g}^{\mu\nu} \partial_\mu \varphi \partial_\nu \varphi - \mathcal{M}^4 = \mathcal{M}^4(\tilde{\chi} - 1), \quad (5)$$

where the factor  $-\mathcal{M}^4$  can be identified with a cosmological constant as in the  $\Lambda$ -CDM scenario, or with the value of the potential  $V(\varphi)$  that we assume to be flat on the scales of interest. Thus, in this paper we neglect the impact of possible variations of the potential  $V(\varphi)$ . This is to simplify the model, to avoid introducing a second arbitrary function  $V(\varphi)$ , and to focus on the properties associated with the kinetic conformal coupling.

### B. Goldstone Models

#### 1. Shift symmetry

This class of derivatively coupled models is not artificial and in fact belongs to a class of very well motivated ones: the Goldstone models. Indeed, let us consider a global

$U(1)$  symmetry broken at a scale  $f$  by the vacuum expectation value (vev) of a complex scalar field  $\Phi$ . Let us consider the simple model

$$S = \int d^4x \sqrt{-\tilde{g}} \left[ -\tilde{g}^{\mu\nu} \partial_\mu \bar{\Phi} \partial_\nu \Phi - V(|\Phi|^2) \right] \quad (6)$$

in the Einstein frame. Let us assume that the potential has a minimum  $f$  such that

$$\partial_v V(v^2) = 0 \quad \text{at} \quad v = f. \quad (7)$$

Because of the global  $U(1)$  invariance of the model  $\Phi \rightarrow e^{i\theta} \Phi$ , at low energy, the breaking of the global  $U(1)$  symmetry leads to the presence of one Goldstone mode  $\varphi$  such that

$$\Phi = f e^{i\varphi/(\sqrt{2}f)}, \quad (8)$$

whose low-energy Lagrangian follows from

$$-\tilde{g}^{\mu\nu} \partial_\mu \bar{\Phi} \partial_\nu \Phi \rightarrow -\frac{1}{2} \tilde{g}^{\mu\nu} \partial_\mu \varphi \partial_\nu \varphi \quad (9)$$

and represents a massless scalar field. Moreover, at the minimum of the potential we have

$$V(|\Phi|^2) \rightarrow V(f^2), \quad (10)$$

which acts as a cosmological constant. Hence at energies below  $f$ , the model is described by a massless scalar field with a cosmological constant term  $V(f^2)$ . This would correspond to the constant factor  $\mathcal{M}^4$  in the scalar-field Lagrangian (5). The scale  $f$  should also be thought to be close to  $\mathcal{M}$ . Here we have in mind models such as  $V(v^2) = -\mu^2 v^2 + \lambda v^4 + V_0$ , where we expect  $\lambda \sim 1$  as it is dimensionless and  $V_0$  is taken to be of order  $\mu^4$  as we assume that only one scale appears in the model. The mass term is corrected by its interaction with other fields and the thermal mass becomes  $m^2(T) = \alpha T^2 - \mu^2$  where  $\alpha$  is a model-dependent constant, see [21] for instance. At high temperature, the minimum of the potential is at the origin whereas at low temperature the symmetry is broken below the critical temperature where the thermal mass vanishes. This gives at low temperature  $T \ll T_c$  the minimum  $f = \mu/\sqrt{2\lambda}$ , whilst the transition occurs at the critical temperature  $T_c = \mu/\sqrt{\alpha} = \sqrt{2\lambda}f/\sqrt{\alpha}$ . The minimum of the potential in the low-temperature phase is  $V(f^2) = V_0 - \mu^4/(4\lambda)$ , which is of order  $\mu^4$ .

## 2. Coupling to matter and conformal gravitational coupling

Let us now consider the coupling between  $\Phi$  and matter. The global symmetry implies that the only couplings to matter must be shift symmetric  $\varphi \rightarrow \varphi + c$  and therefore arise from derivative interactions such as

$$\frac{\tilde{g}^{\mu\nu} \partial_\mu \bar{\Phi} \partial_\nu \Phi}{\mathcal{M}^4} m_\psi \bar{\psi} \tilde{\psi}, \quad (11)$$

where the fermion  $\tilde{\psi}$  of mass  $m_\psi$  could represent dark matter fields and  $\mathcal{M}$  is a suppression scale. At low energy this gives rise to the term

$$\frac{\tilde{g}^{\mu\nu} \partial_\mu \varphi \partial_\nu \varphi}{2\mathcal{M}^4} m_\psi \bar{\psi} \tilde{\psi}. \quad (12)$$

This interaction can equivalently be obtained from a derivative conformal coupling with

$$A(X) = 1 + \tilde{\chi}, \quad (13)$$

where  $\tilde{\chi}$  was defined in Eq.(4). More generally we have the correspondence

$$A \left( -\frac{\tilde{g}^{\mu\nu} \partial_\mu \bar{\Phi} \partial_\nu \Phi}{\mathcal{M}^4} \right) m_\psi \bar{\psi} \tilde{\psi} \rightarrow A(\tilde{\chi}) m_\psi \bar{\psi} \tilde{\psi}, \quad (14)$$

where  $A(\tilde{\chi})$  is the conformal derivative coupling in Bekenstein's metric with

$$g_{\mu\nu} = A^2(\tilde{\chi}) \tilde{g}_{\mu\nu}, \quad (15)$$

as in Eq.(4). Hence the derivative coupling models are in one to one correspondence with Abelian Goldstone models coupled to matter where the coupling function is directly related to the interaction terms between fermions and the complex scalar  $\Phi$ . Indeed upon the identification between the Jordan- and Einstein-frame fermions

$$\tilde{\psi} = A^{3/2}(\tilde{\chi}) \psi, \quad (16)$$

we have the equality between the actions

$$\begin{aligned} S_\psi &= - \int d^4x \sqrt{-g} (i\bar{\psi} \gamma^\mu \nabla_\mu \psi + m_\psi \bar{\psi} \psi) \\ &= - \int d^4x \sqrt{-\tilde{g}} (i\bar{\tilde{\psi}} \tilde{\gamma}^\mu \tilde{\nabla}_\mu \tilde{\psi} + A(\tilde{\chi}) m_\psi \bar{\tilde{\psi}} \tilde{\psi}), \end{aligned} \quad (17)$$

where  $\nabla_\mu$  (respectively  $\tilde{\nabla}_\mu$ ) are the covariant derivatives including the spin connections in the two frames, see appendix A. In particular, the Einstein-frame mass can be identified with  $\tilde{m}_\psi = A m_\psi$ .

## C. Total action and equation of motion for the scalar field

### 1. Coupling to fermions

For the scalar field  $\varphi$ , associated for instance with the Goldstone mode in the Goldstone models, the total action that includes both the scalar-field Lagrangian (5) and the coupling to fermions through the fermionic action (17) reads in Einstein frame as

$$\begin{aligned} S_\varphi &= \int d^4x \sqrt{-g} \left[ -\frac{1}{2} \tilde{g}^{\mu\nu} \partial_\mu \varphi \partial_\nu \varphi - A(\tilde{\chi}) m_\psi \bar{\tilde{\psi}} \tilde{\psi} \right] \\ &= \int d^4x \sqrt{-\tilde{g}} \left[ \mathcal{M}^4 \tilde{\chi} - A(\tilde{\chi}) m_\psi \bar{\tilde{\psi}} \tilde{\psi} \right], \end{aligned} \quad (18)$$

where we did not include the cosmological constant, which does not contribute to the equation of motion of the scalar field. Using

$$\frac{\delta\tilde{\chi}(x)}{\delta\varphi(x')} = -\frac{1}{\mathcal{M}^4}\tilde{g}^{\mu\nu}(x)\frac{\partial\varphi}{\partial x^\nu}\frac{\partial}{\partial x^\mu}\delta_D(x-x'), \quad (19)$$

the Klein-Gordon equation in the Einstein frame reads as

$$\begin{aligned} & \tilde{\nabla}_\mu \left[ \left( 1 - \frac{d\ln A}{d\tilde{\chi}} A \frac{m_\psi \bar{\psi} \tilde{\psi}}{\mathcal{M}^4} \right) \tilde{\nabla}^\mu \varphi \right] \\ & = \tilde{\nabla}_\mu \left[ \left( 1 - \frac{d\ln A}{d\tilde{\chi}} A^4 \frac{m_\psi \bar{\psi} \psi}{\mathcal{M}^4} \right) \tilde{\nabla}^\mu \varphi \right] = 0. \end{aligned} \quad (20)$$

Now in the Jordan frame, onshell and for any fermion field we have that the trace of the energy-momentum tensor is given by

$$T_\psi = -m_\psi \bar{\psi} \psi, \quad (21)$$

implying that the Klein-Gordon equation becomes

$$\tilde{\nabla}_\mu \left[ \left( 1 + \frac{d\ln A}{d\tilde{\chi}} A^4 \frac{T_\psi}{\mathcal{M}^4} \right) \tilde{\nabla}^\mu \varphi \right] = 0. \quad (22)$$

We will see that this is the general Klein-Gordon equation for any derivatively coupled scalar model.

Let us now assume that the fermions condense and acquire an occupation number at low momentum

$$n_\psi = \langle 0 | \bar{\psi} \psi | 0 \rangle. \quad (23)$$

We can identify the conserved matter density as

$$\rho_\psi = m_\psi n_\psi, \quad (24)$$

and  $T_\psi = -\rho_\psi$ . This could be what happens for dark matter and therefore we have derived the Klein-Gordon equation for the scalar  $\varphi$  in the presence of Cold Dark Matter

$$\tilde{\nabla}_\mu \left[ \left( 1 - \frac{d\ln A}{d\tilde{\chi}} A^4 \frac{\rho_\psi}{\mathcal{M}^4} \right) \tilde{\nabla}^\mu \varphi \right] = 0, \quad (25)$$

whose solutions will be studied below. In the following, we will only work in the low energy regime below the symmetry breaking scale  $f$ . The Abelian model involving both fermions  $\psi$  and the scalar  $\Phi$  should be seen as the UV completion of the model.

Going back to the action (18), we can see that the effective action for the scalar field, which recovers the equation of motion of the scalar field, reads as

$$S_\varphi^{\text{eff}} = \int d^4x \sqrt{-\tilde{g}} \left[ -\frac{1}{2}(\tilde{\partial}\varphi)^2 + A(\tilde{\chi})\check{T}_\psi \right], \quad (26)$$

with

$$\check{T}_\psi = A^3 T_\psi. \quad (27)$$

In other words, the term associated with the coupling to matter that enters the effective action (26) is  $A(\tilde{\chi})\check{T}_\psi$ , where the quantity that is kept fixed when we look for the extremum with respect to  $\varphi$  of the action is neither the Jordan-frame  $T_\psi$  nor the Einstein-frame-like quantity  $A^4 T_\psi$ , but the intermediate quantity  $\check{T}_\psi$ .

## 2. Coupling to classical point-particles

Here we note that the same effective action (26) holds when we have a coupling to classical point-particles, described by the Jordan-frame action

$$S = - \int d^4x m \sum_{i=1}^N \sqrt{-g_{\mu\nu} \frac{dx^\mu}{d\tau} \frac{dx^\nu}{d\tau}} \delta_D^3(\vec{x} - \vec{y}_i). \quad (28)$$

This gives for the trace of the energy-momentum tensor

$$T = - \frac{m}{\sqrt{-g}} \sum_{i=1}^N \sqrt{-g_{\mu\nu} \frac{dx^\mu}{d\tau} \frac{dx^\nu}{d\tau}} \delta_D^3(\vec{x} - \vec{y}_i). \quad (29)$$

In the Einstein frame, we can write the action (28) as

$$S = - \int d^4x m A \sum_{i=1}^N \sqrt{-\tilde{g}_{\mu\nu} \frac{dx^\mu}{d\tau} \frac{dx^\nu}{d\tau}} \delta_D^3(\vec{x} - \vec{y}_i), \quad (30)$$

and as for the fermions we can identify  $\tilde{m} = Am$ . The total action for the scalar field  $\varphi$  is the sum of the scalar-field Lagrangian (5) and of the action (30), which explicitly involves the factor  $A(\tilde{\chi})$ . This gives again the Klein-Gordon equation (22), where  $T_\psi$  is replaced by the trace  $T$  of Eq.(29). Therefore, we recover the effective action (26) for the scalar field, where  $\check{T}_\psi$  is replaced by  $\check{T}$  with

$$\begin{aligned} \check{T} &= - \frac{m}{\sqrt{-\tilde{g}}} \sum_{i=1}^N \sqrt{-\tilde{g}_{\mu\nu} \frac{dx^\mu}{d\tau} \frac{dx^\nu}{d\tau}} \delta_D^3(\vec{x} - \vec{y}_i) \\ &= A^3 T. \end{aligned} \quad (31)$$

Again, the coupling to matter is described by the simple term  $A(\tilde{\chi})\check{T}$ , where  $\check{T}$  is neither the Jordan-frame nor Einstein-frame trace of the matter energy-momentum tensor, but the intermediate quantity  $\check{T} = A^3 T$ .

## D. Ultralocal models

The kinetic conformal coupling models defined by Eqs.(3)-(4) are closely related to the ultralocal models introduced in [14]. These ultralocal models are defined by the same action as Eq.(3) but the conformal transformation involves the scalar field  $\varphi$  instead of its kinetic term,

$$\text{ultralocal: } g_{\mu\nu} = A^2(\varphi)\tilde{g}_{\mu\nu}, \quad (32)$$

and the scalar-field Lagrangian is dominated by its potential term, instead of its kinetic term,

$$\text{ultralocal: } \tilde{\mathcal{L}}_\varphi(\varphi) = -V(\varphi). \quad (33)$$

Then, making the field redefinition

$$\tilde{\chi} \equiv -\frac{V(\varphi)}{\mathcal{M}^4} \quad \text{and} \quad A(\tilde{\chi}) \equiv A(\varphi), \quad (34)$$

the scalar-field Lagrangian becomes

$$\text{ultralocal: } \tilde{\mathcal{L}}_{\tilde{\chi}}(\tilde{\chi}) = \mathcal{M}^4 \tilde{\chi}, \quad (35)$$

that is, the Lagrangian is only a linear potential. Apart from the factor  $-1$ , we recover the Lagrangian (5) and the conformal coupling  $A(\tilde{\chi})$ . However, for the ultralocal models  $\tilde{\chi}$  is a standard scalar field, whereas for the models (3) that we study in this paper, it is the kinetic term (4) of an underlying scalar field  $\varphi$ .

The total action for the scalar field  $\tilde{\chi}$  is again

$$\text{ultralocal: } S_{\tilde{\chi}}^{\text{eff}} = \int d^4x \sqrt{-\tilde{g}} \left[ \mathcal{M}^4 \tilde{\chi} + A(\tilde{\chi})\check{\mathbb{T}} \right], \quad (36)$$

with  $\check{\mathbb{T}} = A^3 T$ , and the equation of motion reads as

$$\text{ultralocal: } 1 + \frac{d \ln A}{d \tilde{\chi}} A^4 \frac{T}{\mathcal{M}^4} = 0. \quad (37)$$

We recover the expression within the inner brackets in Eq.(22). This means that, apart from the trivial solution  $\varphi = \text{constant}$ , the other solution of the kinetic conformal coupling model associated with the vanishing of the inner brackets in Eq.(22) corresponds to the solution of the ultralocal model with the same  $A(\tilde{\chi})$ . We shall see that we indeed recover the same equations of motion for both models in the Jordan frame, both for the scalar field and matter.

### III. QUANTUM PROPERTIES

#### A. Ultralocal models

We first consider whether the simpler ultralocal models can have a quantum description. From the effective action (36), working in Minkowski spacetime (i.e., we neglect metric fluctuations) and performing a Wick rotation, the Euclidian generating functional of these models reads as

$$Z[j] = \int \mathcal{D}\tilde{\chi} e^{\int d^4x [j\tilde{\chi} + \mathcal{M}^4 \tilde{\chi} + A(\tilde{\chi})\check{\mathbb{T}}]}. \quad (38)$$

If we use a lattice regularization, we write Eq.(38) as

$$Z[j] = \lim_{\epsilon \rightarrow 0} \int \prod_k d\tilde{\chi}_k e^{\epsilon \sum_k [j_k \tilde{\chi}_k + \mathcal{M}^4 \tilde{\chi}_k + A(\tilde{\chi}_k)\check{\mathbb{T}}_k]}, \quad (39)$$

where  $\epsilon$  is the spacetime volume of each lattice cell. Because of the ultralocal character of the model, the lattice field variables  $\tilde{\chi}_k$  are decoupled and we can write

$$Z[j] = \lim_{\epsilon \rightarrow 0} [Z_{(\epsilon)}(\epsilon j)]^N = \lim_{\epsilon \rightarrow 0} e^{N \sum_{n=1}^{\infty} (\epsilon j)^n \langle \tilde{\chi}^n \rangle_{c(\epsilon)} / n!}, \quad (40)$$

where we take the source  $j$  to be constant over some finite spacetime volume  $VT$  that covers  $N$  lattice points,

$VT = N\epsilon$ , and zero elsewhere. The one-cell generating function is

$$Z_{(\epsilon)}(j) = \frac{\int d\tilde{\chi} e^{j\tilde{\chi} + \epsilon [\mathcal{M}^4 \tilde{\chi} + A(\tilde{\chi})\check{\mathbb{T}}]}}{\int d\tilde{\chi} e^{\epsilon [\mathcal{M}^4 \tilde{\chi} + A(\tilde{\chi})\check{\mathbb{T}}]}} = \langle e^{j\tilde{\chi}} \rangle_{(\epsilon)}, \quad (41)$$

where the subscript “ $(\epsilon)$ ” denotes the dependence on the lattice discretization  $\epsilon$ . In the second equality in Eq.(40) we used the expansion over cumulants of the generating function  $Z_{(\epsilon)}$ . In [14] and [22] we considered ultralocal models where  $\tilde{\chi}$  is restricted to a finite or half-bounded interval. If the variable  $\tilde{\chi}$  is restricted to a finite interval  $[\tilde{\chi}_{\min}, \tilde{\chi}_{\max}]$ , the cumulants  $\langle \tilde{\chi}^n \rangle_{c(\epsilon)}$  are finite for all  $n$  and  $\epsilon$ , and in the limit  $\epsilon \rightarrow 0$  they converge to the finite cumulants associated with the uniform distribution over  $[\tilde{\chi}_{\min}, \tilde{\chi}_{\max}]$ . Then, there is no need for renormalization and in the continuum limit  $\epsilon \rightarrow 0$  only the first term  $n = 1$  is nonzero in the sum in the exponential in Eq.(40), which gives

$$Z[j] = e^{VT j \langle \tilde{\chi} \rangle_{(0)}}. \quad (42)$$

For a non-constant source  $j(x)$  this yields

$$Z[j] = e^{\int d^4x j(x) \langle \tilde{\chi} \rangle_{(0)}}. \quad (43)$$

This is the generating functional of a field  $\tilde{\chi}(x)$  that has vanishing fluctuations, with a Dirac distribution  $\delta_D(\tilde{\chi}(x) - \langle \tilde{\chi} \rangle_{(0)})$ . However, the mean  $\langle \tilde{\chi} \rangle_{(0)}$  is not set by the saddle point  $\tilde{\chi}_c$  of the effective potential  $V^{\text{eff}}(\tilde{\chi}) = -\mathcal{M}^4 \tilde{\chi} - A(\tilde{\chi})\check{\mathbb{T}}$ , but by the mean  $(\tilde{\chi}_{\min} + \tilde{\chi}_{\max})/2$  of the uniform distribution over the interval  $[\tilde{\chi}_{\min}, \tilde{\chi}_{\max}]$ . Thus, we find that in the continuum limit the ultralocal models with a finite range for the field  $\tilde{\chi}$  have a trivial limit that is independent of the coupling function  $A(\tilde{\chi})$  (apart from the value of the boundaries  $[\tilde{\chi}_{\min}, \tilde{\chi}_{\max}]$ ).

This is reminiscent of the case where the field  $\tilde{\chi}$  is unbounded. Then, the analysis is more complex and may involve a renormalization of the potential, but one again finds a trivial limit, the Gaussian field [23, 24]. In both cases, this is due to the central limit theorem (in our case the variance of the Gaussian goes to zero because the lattice field was bounded). In the unbounded case, one might obtain nontrivial results by introducing a non-conventional quantization procedure, associated with a nonstandard choice for the measure  $\mathcal{D}\tilde{\chi}$  of the path integral [23]. We do not consider such an approach here, as we do not wish to have different path-integral measures for ordinary matter fields and the  $\tilde{\chi}$  field.

We also note that because there is no kinetic term the action is very different from the standard harmonic oscillator case. In particular, if the Hamiltonian reads at quadratic order as  $H = \int dx \frac{m^2}{2} \tilde{\chi}^2$ , it reads as  $H = \int \frac{d\mathbf{k}}{(2\pi)^3} \frac{m^2}{4\omega_k} [a_{\mathbf{k}}^\dagger a_{\mathbf{k}} + a_{\mathbf{k}} a_{\mathbf{k}}^\dagger + a_{-\mathbf{k}}^\dagger a_{\mathbf{k}}^\dagger e^{2i\omega_k t} + a_{-\mathbf{k}} a_{\mathbf{k}} e^{-2i\omega_k t}]$  in terms of the usual creation and annihilation operators, instead of  $H = \int \frac{d\mathbf{k}}{(2\pi)^3} \frac{\omega_k}{2} [a_{\mathbf{k}}^\dagger a_{\mathbf{k}} + a_{\mathbf{k}} a_{\mathbf{k}}^\dagger]$ . Besides, the plane waves  $e^{\pm i\mathbf{k}x}$  are not solutions of the equation of motion of the scalar field,  $\tilde{\chi} = 0$ , which is not a wave

equation and does not propagate. Thus we cannot expect ultralocal models to follow the standard quantization.

On the other hand, if the lattice cell  $\epsilon$  is kept fixed, as for standard quantum field theories we recover the usual classical limit on macroscopic scales, where the action  $S = N\epsilon S_{(\epsilon)}$  is much greater than 1, with  $N \gg 1$ .

In practice, we consider the ultralocal Lagrangian to be an effective theory, which only applies on time and length scales greater than some UV cutoff  $\epsilon^{1/4}$ , in a manner similar to the hydrodynamic approximation for fluids. Then, we cannot use the ultralocal Lagrangian for quantum studies and it only makes sense at the classical level, as a macroscopic theory. Since the only dimensional scale that enters this effective Lagrangian is  $\mathcal{M}^4 \sim \bar{\rho}_{\text{de}0}$ , with  $\mathcal{M} \sim 10^{-3}\text{eV}$  and  $\mathcal{M}^{-1} \sim 0.1\text{mm}$ , it is natural to expect this cutoff to be around the millimeter scale, which allows one to study cosmological and astrophysical structures. An alternative is to consider the ultralocal field  $\tilde{\chi}$  to be a truly classical field, without any quantum fluctuations.

## B. Kinetic conformal coupling models

Going back to the kinetic conformal coupling models, which are the focus of this paper, we can see that these models share some difficulties with the ultralocal models. From the effective action (26) the generating functional reads as

$$Z[j] = \int \mathcal{D}\varphi e^{i \int d^4x [j\varphi + \mathcal{M}^4 \tilde{\chi} + A(\tilde{\chi})\tilde{\Gamma}]}, \quad (44)$$

where we consider Minkowski spacetime. As we shall see below in section VI, it is natural to restrict the kinetic term  $\tilde{\chi}$  to the positive semiaxis,  $\tilde{\chi} \geq 0$ , and in practice we shall consider finite intervals  $[0, \gamma]$  with  $\gamma > 0$ . [The restriction to  $\tilde{\chi} \geq 0$  is required to avoid multivalued solutions to the equation of motion of the scalar field.] This means that the coupling function  $A(\tilde{\chi})$  is not necessarily defined on the negative semiaxis  $\tilde{\chi} < 0$ , and may show a branch cut at  $\tilde{\chi} = 0$  as in the simple explicit model (168) (where  $\mathcal{X} = \tilde{\chi}/\gamma$ ). In such cases we cannot perform a Wick rotation to Euclidian space, which transforms  $\tilde{\chi}$  to  $\tilde{\chi}_E < 0$ . Because of the constraint  $\tilde{\chi} > 0$ , and the fact that the equations of motion (at the classical level) can be written in terms of  $\tilde{\chi}$  only, as we shall see in the following sections, it is tempting to change variable from  $\varphi$  to  $\tilde{\chi}$  in the path integral (44). From the solution (149), which gives  $\varphi$  in terms of  $\tilde{\chi}$ , where  $\psi = \sqrt{2\mathcal{M}^4 \tilde{\chi}}$  from Eq.(136) (with  $a = 1$  in the Minkowski case), we have

$$\frac{\mathcal{D}\varphi(x)}{\mathcal{D}\psi(x')} = - \int_0^\tau ds \sqrt{1 - v^2(s)} \delta_D(x' - q(s)). \quad (45)$$

Here we used that due to the maximization in Eq.(149) the perturbations  $\delta\varphi$  are quadratic in the perturbations  $\delta q(s)$  with respect to the maximizing path  $q(s)$ . As the paths  $q(s)$  that enter Eq.(45) are global functions of the field  $\psi$ , the Jacobian  $|\mathcal{D}\varphi/\mathcal{D}\psi|$  is not a constant that can

be absorbed in the normalization of the path integral. However, if we choose to define the path integral (44) with the measure  $\int \mathcal{D}\psi$  instead of  $\int \mathcal{D}\varphi$ , we recover ultralocal models (taking  $j\psi$  for the source term) and the lack of standard quantization. This suggests that the kinetic conformal coupling models cannot be considered at the quantum level.

A simpler and rigorous argument comes from the study of the cosmological background. From Eq.(26) the effective scalar-field Lagrangian is

$$\mathcal{L}_\varphi^{\text{eff}} = \mathcal{M}^4 \tilde{\chi} - \check{\rho} A(\tilde{\chi}), \quad (46)$$

with  $\check{\Gamma} = -\check{\rho}$ . Expanding around the cosmological background  $\bar{\varphi}$ ,  $\tilde{\chi} = (d\bar{\varphi}/d\tau)^2 / (2\mathcal{M}^4 a^2)$ , with  $\varphi = \bar{\varphi} + \delta\varphi$ ,  $\tilde{\chi} = \bar{\chi} + \delta\tilde{\chi}$ , we have

$$\delta\tilde{\chi} = \frac{1}{2\mathcal{M}^4 a^2} \left[ 2 \frac{d\bar{\varphi}}{d\tau} \frac{\partial \delta\varphi}{\partial \tau} + \left( \frac{\partial \delta\varphi}{\partial \tau} \right)^2 - (\nabla \delta\varphi)^2 \right]. \quad (47)$$

If the background is given by the nontrivial solution of the equation of motion (22),

$$1 - \frac{\check{\rho}}{\mathcal{M}^4} \frac{dA}{d\tilde{\chi}} = 0, \quad (48)$$

the Lagrangian (46) reads up to quadratic order as

$$\delta\mathcal{L}_{\delta\varphi}^{\text{eff}} = - \frac{\check{\rho} \bar{\chi}}{\mathcal{M}^4 a^2} \frac{d^2 \bar{A}}{d\bar{\chi}^2} \left( \frac{\partial \delta\varphi}{\partial \tau} \right)^2 + \dots \quad (49)$$

This corresponds to a massless and vanishing-speed Gaussian field. If we try to apply the canonical quantization to this field, adding a nonzero velocity term  $c_\varphi^2 (\nabla \delta\varphi)^2$  to the quadratic Lagrangian, we find divergences in inverse powers of  $c_\varphi$  in the limit  $c_\varphi \rightarrow 0$  in the perturbative expansions.

For instance, let us consider scattering diagrams between photons, gravitons and the scalar field. Higher-order contributions to the Lagrangian  $\delta\mathcal{L}_\varphi^{\text{eff}}$  include terms of the form  $[(\partial \delta\varphi)^2]^\ell$ , which give rise to a linear coupling to the graviton of the form

$$\mathcal{L}_{\delta\varphi}^{(2\ell)} \supset \frac{h_{\mu\nu}}{M_{\text{Pl}}} \frac{\partial^\mu \delta\varphi \partial^\nu \delta\varphi (\partial \delta\varphi)^{2(\ell-1)}}{M_\ell^{4(\ell-1)}}, \quad (50)$$

where  $h_{\mu\nu} = M_{\text{Pl}} \delta g_{\mu\nu}$  and  $M_\ell \sim \mathcal{M}$ . Taking into account the vertex between one graviton and two photons of the type (we only pick one part)

$$\mathcal{L}_\gamma = \frac{h_{\mu\nu}}{M_{\text{Pl}}} \partial^\mu A^\rho \partial^\nu A_\rho, \quad (51)$$

we can draw a scattering diagram associated with the creation of  $(2\ell)$  scalars from two photons, with the exchange of a graviton. The cross section reads as

$$d\sigma_{(2\ell)} = \frac{1}{2E_{\text{CM}}^2} \left( \prod_{i=1}^{2\ell} \frac{d^3 p_i}{(2\pi)^3 2p_i c_\varphi} \right) |\mathcal{M}_{(2\ell)}|^2 (2\pi)^4 \times \delta_D^{(3)} \left( \sum_i \mathbf{p}_i \right) \delta_D \left( \sum_i E_i - E_{\text{CM}} \right), \quad (52)$$

where  $E_{\text{CM}} = E'_1 + E'_2$  is the total energy in the center-of-mass frame of the two incoming photons  $p'_1$  and  $p'_2$ . The matrix element is symbolically

$$\mathcal{M}_{(2\ell)} \sim \frac{p'_1 p'_2 (\prod_{i=1}^{2\ell} p_i)}{M_{\text{Pl}}^2 M_\ell^{4(\ell-1)} p^2}, \quad (53)$$

i.e., one momentum appears for each scalar and each photon, and there is one graviton propagator, with  $p = p'_1 + p'_2$ . For each scalar we have the dispersion relation

$$E_i = p_i c_\varphi. \quad (54)$$

We can integrate at once over  $\mathbf{p}_{2\ell}$  with the momentum Dirac function, which gives  $\mathbf{p}_{2\ell} = -\sum_{i=1}^{2\ell-1} \mathbf{p}_i$  and

$$d\sigma_{(2\ell)} = \frac{\pi}{2E_{\text{CM}}^2 c_\varphi^{2\ell+1}} \left( \prod_{i=1}^{2\ell-1} \frac{d^3 p_i}{(2\pi)^3 2p_i} \right) \frac{1}{p_{2\ell}} \times \delta_D \left( \sum_{i=1}^{2\ell} p_i - \frac{E_{\text{CM}}}{c_\varphi} \right) |\mathcal{M}_{(2\ell)}|^2. \quad (55)$$

If only one of the  $p_i$  is of order  $1/c_\varphi$  among  $1 \leq i \leq 2\ell - 1$  (and  $p_{2\ell} \sim 1/c_\varphi$  as well), we have  $\sigma \sim c_\varphi^{-2\ell-5}$ . If all momenta are of the same order  $1/c_\varphi$ , we have  $\sigma \sim c_\varphi^{-10\ell+3}$ . Thus, perturbative diagrams with  $N$  scalars typically diverge as  $1/c_\varphi^N$  or faster, when  $c_\varphi \rightarrow 0$ . This is due to the increasingly large phase space volume when  $c_\varphi \rightarrow 0$ , as greater numbers of modes fall in a given energy range. This means that perturbative expansions are not well defined in this approach.

This can also be seen from the change of variable required to make the small-velocity quadratic Lagrangian canonical. Indeed, writing the quadratic part of the action as

$$S^{(2)} = \frac{1}{2} \int d^4 x \left[ \left( \frac{\partial \delta \varphi}{\partial t} \right)^2 - c_\varphi^2 (\nabla \delta \varphi)^2 \right] = \frac{1}{2} \int d^4 \tilde{x} \left[ \left( \frac{\partial \tilde{\phi}}{\partial \tilde{t}} \right)^2 - (\nabla \tilde{\phi})^2 \right], \quad (56)$$

where we made the change of variables

$$t = \tilde{t}/c_\varphi, \quad \delta \varphi = \tilde{\phi}/\sqrt{c_\varphi}, \quad (57)$$

we find that higher-order terms of the Lagrangian, such as  $(\nabla \delta \varphi)^{2n}$ , diverge as  $1/c_\varphi^n$  for  $c_\varphi \rightarrow 0$  (higher-order gradients are not suppressed by  $c_\varphi$ ). Then, there is no perturbative regime and the limit  $c_\varphi \rightarrow 0$  is singular.

Alternatively, if we only keep the quadratic part of the Lagrangian (49), we recover a situation similar to the ultralocal models considered in the previous section. As the Lagrangian only involves the time derivative  $(\partial \delta \varphi / \partial \tau)^2$ , different space locations are decoupled. Therefore, if we consider a lattice regularization, similar to Eq.(39), the generating functional now factorizes as a product of 1D generating functionals, associated with each spatial grid

point. Again, for bounded fields the distribution of each grid variable becomes flat in the continuum limit and we recover a Dirac distribution for the field averaged over a finite spatial volume. For unbounded fields one again recovers the Gaussian field in the continuum limit [23], in relation with the central limit theorem. Again it is possible to obtain a nontrivial theory by using a non-conventional quantization [23], but we do not investigate this approach here. Since at the quadratic level, around the cosmological background, conventional quantization fails, we cannot develop the quantization of these models.

Then, as for the ultralocal models, we consider the kinetic conformal coupling models to be effective theories, which only apply on time and length scales greater than some UV cutoff, as the hydrodynamic approximation for fluids. Since the dimensional scale that enters the Lagrangian (5) is again  $\mathcal{M}^4 \sim \bar{\rho}_{\text{de}0}$ , it is natural to expect this cutoff not to be far from the millimeter scale, which allows us to study cosmological and astrophysical structures. Within the framework of the Goldstone models described in section II B, we wish the phase transition to occur in this classical regime. As the minimum of the potential  $V(f^2)$  plays the role of the cosmological constant  $\mathcal{M}^4$ , it is sufficient that the cutoff should be somewhat above  $10^{-3}\text{eV}$ , i.e. somewhat below 0.1 mm. The background scalar-field energy density reads as  $\bar{\rho}_\varphi \simeq \mathcal{M}^4(\tilde{\chi} + 1) \sim \mathcal{M}^4$  as we shall see in Eq.(94) below (for models where  $\tilde{\chi}$  is bounded as in this paper). Therefore, at all redshifts the energy density of the scalar field remains below the UV cutoff as soon as the latter is somewhat greater than  $\mathcal{M}$ . An alternative is again to consider the scalar field  $\varphi$  to be a truly classical field, without any quantum fluctuations.

#### IV. EQUATIONS OF MOTION IN THE EINSTEIN FRAME

Here and in the following sections we investigate the cosmological behavior of the kinetic conformal coupling models defined by Eqs.(3)-(5). We first derive in this section the equations of motion in the Einstein frame, where gravity is easier to handle as it is given by the standard Einstein-Hilbert term. We next express these results in the Jordan frame in the following section V, which is better suited to the analysis of matter dynamics. Then, we work in the Jordan frame in the subsequent sections.

##### A. Matter component

The Einstein-frame and Jordan-frame matter energy-momentum tensors are defined by

$$\tilde{T}_{\mu\nu} = \frac{-2}{\sqrt{-\tilde{g}}} \frac{\delta S_{\text{m}}}{\delta \tilde{g}^{\mu\nu}}, \quad T_{\mu\nu} = \frac{-2}{\sqrt{-g}} \frac{\delta S_{\text{m}}}{\delta g^{\mu\nu}}, \quad (58)$$

where we omit the subscript “m” (for matter) in  $\tilde{T}_{m;\mu\nu}$  and  $T_{m;\mu\nu}$  to simplify notations. Because the conformal coupling function  $A$  of Eq.(4) involves the derivative term  $\tilde{\chi}$ , it depends on both the scalar field  $\varphi(x)$  and the metric  $\tilde{g}_{\mu\nu}(x)$ . Then, in contrast with the standard scalar-tensor models, the relation between the Einstein-frame and Jordan-frame matter energy-momentum tensors is no longer  $\tilde{T}_{\mu\nu} = A^2 T_{\mu\nu}$ . Indeed, the derivative conformal mapping (4) yields  $g^{\mu\nu} = A^{-2} \tilde{g}^{\mu\nu}$  and

$$\frac{\delta g^{\mu\nu}}{\delta \tilde{g}^{\alpha\beta}} = A^{-2} \left[ \delta_{\alpha}^{\mu} \delta_{\beta}^{\nu} + \tilde{g}^{\mu\nu} \frac{d \ln A}{d \tilde{\chi}} \frac{\partial_{\alpha} \varphi \partial_{\beta} \varphi}{\mathcal{M}^4} \right], \quad (59)$$

where  $\delta_{\alpha}^{\mu}$  is the Kronecker symbol, while  $\sqrt{-g} = A^4 \sqrt{-\tilde{g}}$ . Then, the definition (58) gives

$$\tilde{T}_{\mu\nu} = A^2 T_{\mu\nu} + A^4 T \frac{d \ln A}{d \tilde{\chi}} \frac{\partial_{\mu} \varphi \partial_{\nu} \varphi}{\mathcal{M}^4}, \quad (60)$$

where we defined the traces of the Einstein-frame and Jordan-frame energy-momentum tensors as

$$\tilde{T} = \tilde{T}_{\mu}^{\mu} = \tilde{g}^{\mu\nu} \tilde{T}_{\mu\nu}, \quad T = T_{\mu}^{\mu} = g^{\mu\nu} T_{\mu\nu}, \quad (61)$$

i.e., operations on Einstein-frame (resp. Jordan-frame) tensors only involve the Einstein-frame (resp. Jordan-frame) metric  $\tilde{g}_{\mu\nu}$  (resp.  $g_{\mu\nu}$ ). The relation (60) also yields

$$\tilde{T} = A^4 T \left[ 1 - 2 \tilde{\chi} \frac{d \ln A}{d \tilde{\chi}} \right], \quad (62)$$

so that Eq.(60) can be inverted as

$$T_{\mu\nu} = A^{-2} \tilde{T}_{\mu\nu} - A^{-2} \tilde{T} \frac{\frac{d \ln A}{d \tilde{\chi}}}{1 - 2 \tilde{\chi} \frac{d \ln A}{d \tilde{\chi}}} \frac{\partial_{\mu} \varphi \partial_{\nu} \varphi}{\mathcal{M}^4}. \quad (63)$$

In the Jordan frame, the matter energy-momentum tensor satisfies the usual conservation law,  $\nabla_{\mu} T_{\nu}^{\mu} = 0$ . From the expression (60) this implies for the Einstein-frame energy-momentum tensor the “nonconservation” law

$$\tilde{\nabla}_{\mu} \tilde{T}_{\nu}^{\mu} = \partial_{\nu} \varphi \tilde{\nabla}_{\mu} \left[ A^4 \frac{T}{\mathcal{M}^4} \frac{d \ln A}{d \tilde{\chi}} \tilde{\nabla}^{\mu} \varphi \right]. \quad (64)$$

[It is the Jordan-frame trace  $T$  that appears within the brackets but it can be expressed in terms of  $\tilde{T}$  through Eq.(62).]

## B. Radiation component

If we consider a radiation component with a pressure  $p_{\text{rad}} = \rho_{\text{rad}}/3$ , instead of a matter component with a small pressure  $p \ll \rho$ , we have  $T_{\text{rad}} = 0$ . Then,  $\tilde{T}_{\text{rad}} = 0$  and  $\tilde{T}_{\text{rad};\mu\nu} = A^2 T_{\text{rad};\mu\nu}$ , and as in standard dilaton models, both Einstein-frame and Jordan-frame radiation energy-momentum tensors satisfy the usual conservation law,  $\tilde{\nabla}_{\mu} \tilde{T}_{\text{rad};\nu}^{\mu} = 0$  and  $\nabla_{\mu} T_{\text{rad};\nu}^{\mu} = 0$ .

## C. Scalar field

The functional derivative of the Jordan-frame metric with respect to the scalar field  $\varphi$  reads as

$$\frac{\delta g^{\mu\nu}(x')}{\delta \varphi(x)} = \frac{2}{\mathcal{M}^4} A^{-2}(x') \frac{d \ln A}{d \tilde{\chi}}(x') \tilde{g}^{\mu\nu}(x') \tilde{g}^{\alpha\beta}(x') \times \partial_{\alpha} \varphi(x') \frac{\partial}{\partial x'^{\beta}} \delta_D(x - x'), \quad (65)$$

and the Klein-Gordon equation of motion of the scalar field  $\varphi$ , obtained from the variation of the action (3) with respect to  $\varphi$ , writes as

$$\tilde{\nabla}_{\mu} \left[ \left( 1 + A^4 \frac{T}{\mathcal{M}^4} \frac{d \ln A}{d \tilde{\chi}} \right) \tilde{\nabla}^{\mu} \varphi \right] = 0. \quad (66)$$

We recover the equation of motion of the scalar field that we obtained in Eq.(22) for the explicit case of fermionic matter and in section II C 2 for matter classical point-particles. The result (66) is general and  $T$  is the sum of the traces of the energy-momentum tensors of all matter components.

The Einstein-frame energy-momentum tensor of the scalar field reads as

$$\begin{aligned} \tilde{T}_{\varphi;\mu\nu} &= \frac{-2}{\sqrt{-\tilde{g}}} \frac{\delta S_{\varphi}}{\delta \tilde{g}^{\mu\nu}} \\ &= \mathcal{M}^4 (\tilde{\chi} - 1) \tilde{g}_{\mu\nu} + \partial_{\mu} \varphi \partial_{\nu} \varphi. \end{aligned} \quad (67)$$

Using the Klein-Gordon equation (66) we obtain the non-conservation law

$$\tilde{\nabla}_{\mu} \tilde{T}_{\varphi;\nu}^{\mu} = \partial_{\nu} \varphi \tilde{\nabla}_{\mu} \tilde{\nabla}^{\mu} \varphi, \quad (68)$$

while the matter nonconservation law (64) simplifies as

$$\tilde{\nabla}_{\mu} \tilde{T}_{\nu}^{\mu} = -\partial_{\nu} \varphi \tilde{\nabla}_{\mu} \tilde{\nabla}^{\mu} \varphi. \quad (69)$$

Then, we can check that the full Einstein-frame energy-momentum tensor obeys the usual conservation law,

$$\tilde{\nabla}_{\mu} \left[ \tilde{T}_{\nu}^{\mu} + \tilde{T}_{\text{rad};\nu}^{\mu} + \tilde{T}_{\varphi;\nu}^{\mu} \right] = 0, \quad (70)$$

which ensures consistency with the Bianchi identity for the Einstein tensor,  $\tilde{\nabla}_{\mu} \tilde{G}_{\nu}^{\mu} = 0$ .

A constant scalar field,  $\varphi = \text{constant}$ , is always a solution of the Klein-Gordon equation (66). Then, the scalar field plays no role; its kinetic energy vanishes, the conformal transformation (4) is an irrelevant rescaling of coordinates by a constant factor, and we recover the  $\Lambda$ -CDM scenario. In the following, we focus on the nontrivial solution of the Klein-Gordon equation (66),

$$1 + A^4 \frac{T}{\mathcal{M}^4} \frac{d \ln A}{d \tilde{\chi}} = 0. \quad (71)$$

This is a constraint equation for the kinetic term  $\tilde{\chi}$ , which becomes a function of the Jordan-frame matter density when  $T = -\rho$ , and we have  $\tilde{\chi}(x) = \tilde{\chi}[\rho(x)]$ .

Then, the relation (60) between the Einstein- and Jordan-frame matter energy-momentum tensors simplifies as

$$\tilde{T}_{\mu\nu} = A^2 T_{\mu\nu} - \partial_\mu \varphi \partial_\nu \varphi. \quad (72)$$

Combining with Eq.(67) we find that the sum of the matter and scalar-field tensors is

$$\tilde{T}_{\mu\nu} + \tilde{T}_{\varphi;\mu\nu} = A^2 T_{\mu\nu} + \mathcal{M}^4 (\tilde{\chi} - 1) \tilde{g}_{\mu\nu}. \quad (73)$$

#### D. Background dynamics

For the cosmological background, which is homogeneous and isotropic, both the Einstein-frame and Jordan-frame metrics are of the Friedman-Lemaitre-Robertson-Walker type, with

$$d\tilde{s}^2 = \tilde{g}_{\mu\nu} dx^\mu dx^\nu = \tilde{a}^2 [-d\tau^2 + d\mathbf{x}^2], \quad (74)$$

$$ds^2 = g_{\mu\nu} dx^\mu dx^\nu = a^2 [-d\tau^2 + d\mathbf{x}^2], \quad (75)$$

where  $\tau$  is the conformal time. The conformal transformation (4) means that the line elements transform as  $ds^2 = A^2 d\tilde{s}^2$ . At the background level, this means that the scale factor, physical time and distance transform as

$$a = \bar{A}\tilde{a}, \quad dt = \bar{A}d\tilde{t}, \quad \mathbf{r} = \bar{A}\tilde{\mathbf{r}}. \quad (76)$$

Throughout this paper we denote with an overbar background quantities.

As we found in Eq.(60), in contrast with models where the conformal transformation (4) only depends on the value of the scalar field  $A(\varphi)$ , the Einstein and Jordan matter energy-momentum tensors are not proportional through a factor  $A^2$ . They also differ by an additive factor that explicitly depends on the scalar field kinetic factor  $\partial_\mu \varphi \partial_\nu \varphi$ . As the matter Lagrangian  $\mathcal{L}_m$  is given in the Jordan frame, in the action (3), it is the Jordan matter energy-momentum tensor that takes the standard form, e.g. the perfect fluid form with an equation of state between matter pressure and density, while the Einstein energy-momentum tensor takes a nonstandard form with contributions from both the matter and scalar field sectors. Moreover, the matter particles follow the geodesics defined by the Jordan-frame metric  $g_{\mu\nu}$  so that they obey standard continuity equations in the fluid limit. At the background level, we write the Jordan- and Einstein-frame energy-momentum tensors as  $\tilde{T}_\nu^\mu = \text{diag}(-\tilde{\rho}, \tilde{p}, \tilde{p}, \tilde{p})$  and  $\tilde{T}_\nu^\mu = \text{diag}(-\tilde{\rho}, \tilde{p}, \tilde{p}, \tilde{p})$ . As usual, we work in the nonrelativistic limit and we neglect the matter pressure,  $p \ll \rho$ . Then, Eq.(60) gives

$$\tilde{\rho} = \bar{A}^4 \bar{\rho} \left[ 1 - 2 \frac{d \ln \bar{A}}{d \ln \tilde{\chi}} \right], \quad \tilde{p} = \bar{A}^4 \bar{p} = 0, \quad (77)$$

where the scalar field kinetic term is

$$\tilde{\chi} = \frac{1}{2\mathcal{M}^4 \tilde{a}^2} \left( \frac{d\tilde{\varphi}}{d\tau} \right)^2 \geq 0. \quad (78)$$

The radiation energy-momentum tensors are proportional, with

$$\tilde{\rho}_{\text{rad}} = \bar{A}^4 \bar{\rho}_{\text{rad}}, \quad \tilde{p}_{\text{rad}} = \bar{A}^4 \bar{p}_{\text{rad}}. \quad (79)$$

The Einstein-frame scalar-field energy-momentum tensor (67) takes its standard form, with

$$\tilde{\rho}_\varphi = \mathcal{M}^4 (\tilde{\chi} + 1), \quad \tilde{p}_\varphi = \mathcal{M}^4 (\tilde{\chi} - 1). \quad (80)$$

In the Einstein frame, we recover the usual Friedmann equation,

$$3\tilde{M}_{\text{Pl}}^2 \tilde{\mathcal{H}}^2 = \tilde{a}^2 (\tilde{\rho} + \tilde{\rho}_{\text{rad}} + \tilde{\rho}_\varphi), \quad (81)$$

where  $\tilde{\mathcal{H}} = d \ln \tilde{a} / d\tau$  is the Einstein-frame conformal expansion rate.

The Klein-Gordon equation (71) reads as

$$\frac{d \ln \bar{A}}{d \tilde{\chi}} = \frac{\mathcal{M}^4}{\bar{A}^4 \tilde{\rho}}, \quad (82)$$

which can be written in terms of the Einstein-frame matter density as

$$\frac{\frac{d \ln \bar{A}}{d \tilde{\chi}}}{1 - 2 \frac{d \ln \bar{A}}{d \ln \tilde{\chi}}} = \frac{\mathcal{M}^4}{\tilde{\rho}}. \quad (83)$$

This equation determines the scalar field kinetic term as a function of the Einstein-frame background matter density,  $\tilde{\chi}(\tau) = \tilde{\chi}[\tilde{\rho}(\tau)]$ . This gives the value of the background scalar field by integrating Eq.(78),

$$\tilde{\varphi}(\tau) = - \int_0^\tau d\tau \sqrt{2\mathcal{M}^4 \tilde{a}^2 \tilde{\chi}}. \quad (84)$$

Here we choose without a loss of generality the boundary condition  $\tilde{\varphi}(\tau = 0) = 0$  and the negative sign for the square-root of Eq.(78), because the action (3) is invariant through the transformations  $\varphi \rightarrow \varphi + \text{constant}$  and  $\varphi \rightarrow -\varphi$ . [We choose more specifically the negative sign as it will correspond to the positive convex Hamiltonian (135) when we obtain  $\varphi$  through the Hamilton-Jacobi equation (132) below. Choosing the positive solution for  $\varphi$  would lead to nonconventional signs in this context.] The scalar-field energy density evolves as

$$\frac{d\tilde{\rho}_\varphi}{d\tau} = \mathcal{M}^4 \frac{d\tilde{\chi}}{d\tau}. \quad (85)$$

The matter nonconservation equation (69) yields

$$\frac{d\tilde{\rho}}{d\tau} = -3\tilde{\mathcal{H}}\tilde{\rho} - 6\tilde{\mathcal{H}}\mathcal{M}^4 \tilde{\chi} - \mathcal{M}^4 \frac{d\tilde{\chi}}{d\tau}. \quad (86)$$

Combining with Eq.(85) we recover the usual conservation law for the sum of the matter and scalar-field components,  $d(\tilde{\rho} + \tilde{\rho}_\varphi) / d\tau = -3\tilde{\mathcal{H}}(\tilde{\rho} + \tilde{\rho}_\varphi + \tilde{p}_\varphi)$ . The radiation density obeys the standard evolution equation

$$\frac{d\tilde{\rho}_{\text{rad}}}{d\tau} = -4\tilde{\mathcal{H}}\tilde{\rho}_{\text{rad}}. \quad (87)$$

## E. Perturbations

In the Einstein frame we write the perturbed metric in the Newtonian gauge as

$$ds^2 = \tilde{a}^2[-(1 + 2\tilde{\Phi})d\tau^2 + (1 - 2\tilde{\Psi})d\mathbf{x}^2], \quad (88)$$

At the linear order in the metric potentials and for scales much below the Hubble radius, the  $(0, 0)$ -component of the Einstein equations,  $\tilde{M}_{\text{Pl}}^2 \tilde{G}_{\nu}^{\mu} = \tilde{T}_{\nu}^{\mu} + \tilde{T}_{\text{rad};\nu}^{\mu} + \tilde{T}_{\varphi;\nu}^{\mu}$ , gives

$$2\tilde{M}_{\text{Pl}}^2 \frac{\nabla^2 \tilde{\Psi}}{\tilde{a}^2} = \delta(A^4 \rho) - \mathcal{M}^4 \delta\tilde{\chi}, \quad (89)$$

where we used the nonrelativistic limit,  $v^2 \ll c^2$ , we neglected fluctuations of the radiation component, and  $\rho$  is again the Jordan-frame density. Hereafter we denote with a  $\delta$  perturbed quantities, such as  $\delta\tilde{\chi} \equiv \tilde{\chi} - \bar{\tilde{\chi}}$ . The nondiagonal  $(i, j)$ -components of the Einstein equations give

$$\frac{\tilde{M}_{\text{Pl}}^2}{\tilde{a}^2} \partial_i \partial_j (\tilde{\Psi} - \tilde{\Phi}) = \bar{A}^4 \rho v_i v_j, \quad (90)$$

at linear order over  $\delta A$ , and in the nonrelativistic limit we obtain

$$\tilde{\Phi} = \tilde{\Psi}. \quad (91)$$

## V. EQUATIONS OF MOTION IN THE JORDAN FRAME

We now express in the Jordan frame the results obtained in the previous section. We study both the background dynamics and the growth of linear perturbations.

### A. Background dynamics

From Eq.(76) the conformal expansion rates in the Jordan and Einstein frames are related by

$$\tilde{\mathcal{H}} = (1 - \epsilon_2)\mathcal{H} \quad \text{with} \quad \epsilon_2(\tau) = \frac{d \ln \bar{A}}{d \ln a}. \quad (92)$$

From Eq.(72) the Einstein- and Jordan-frame background matter densities are related by

$$\bar{\tilde{\rho}} = \bar{A}^4 \bar{\rho} - 2\mathcal{M}^4 \bar{\tilde{\chi}}. \quad (93)$$

We also define the effective Jordan-frame scalar-field density and pressure by a simple rescaling by  $\bar{A}^4$ ,

$$\bar{\tilde{\rho}}_{\varphi} \equiv \frac{\bar{\tilde{\rho}}_{\varphi}}{\bar{A}^4} = \mathcal{M}^4 \frac{\bar{\tilde{\chi}} + 1}{\bar{A}^4}, \quad \bar{\tilde{p}}_{\varphi} \equiv \frac{\bar{\tilde{p}}_{\varphi}}{\bar{A}^4} = \mathcal{M}^4 \frac{\bar{\tilde{\chi}} - 1}{\bar{A}^4}. \quad (94)$$

Then, the Friedmann equation (81) yields

$$3M_{\text{Pl}}^2 \mathcal{H}^2 = (1 - \epsilon_2)^{-2} a^2 (\bar{\rho} + \bar{\rho}_{\text{rad}} - \bar{p}_{\varphi}), \quad (95)$$

where we defined the time-dependent Jordan-frame Planck mass as

$$M_{\text{Pl}}^2(\tau) \equiv \bar{A}^{-2} \tilde{M}_{\text{Pl}}^2. \quad (96)$$

It is the scalar-field pressure with a negative sign,  $-\bar{p}_{\varphi}$ , instead of the density  $\bar{\rho}_{\varphi}$ , that enters the Friedmann equation (95), because of the second term in Eq.(93). To recover the Friedmann equation in its standard form, we can define an effective dark-energy density by

$$3M_{\text{Pl}}^2 \mathcal{H}^2 = a^2 (\bar{\rho} + \bar{\rho}_{\text{rad}} + \bar{\rho}_{\text{de}}), \quad (97)$$

which gives

$$\bar{\rho}_{\text{de}} \equiv -\bar{p}_{\varphi} + \frac{2\epsilon_2 - \epsilon_2^2}{(1 - \epsilon_2)^2} (\bar{\rho} + \bar{\rho}_{\text{rad}} - \bar{p}_{\varphi}). \quad (98)$$

In the Jordan frame the matter obeys the standard conservation equations,  $\nabla_{\mu} T_{\nu}^{\mu} = 0$ , and the background matter and radiation densities evolve as

$$\bar{\rho} = \frac{\bar{\rho}_0}{a^3}, \quad \bar{\rho}_{\text{rad}} = \frac{\bar{\rho}_{\text{rad}0}}{a^4}. \quad (99)$$

The scalar-field is given by Eq.(82), which reads as

$$\bar{A}^4 \frac{d \ln \bar{A}}{d \tilde{\chi}} = \frac{\mathcal{M}^4}{\bar{\rho}}. \quad (100)$$

This determines the scalar field kinetic term as a function of the Jordan-frame background matter density,  $\bar{\tilde{\chi}}(\tau) = \bar{\tilde{\chi}}[\bar{\rho}(\tau)]$ , and the integrated equation (84) becomes

$$\bar{\varphi} = - \int_0^{\tau} d\tau' \frac{\sqrt{2\mathcal{M}^4 a^2 \bar{\tilde{\chi}}}}{\bar{A}}. \quad (101)$$

We also have from Eq.(100)

$$\frac{d \bar{\tilde{\chi}}}{d\tau} = \epsilon_2 \mathcal{H} \frac{\bar{A}^4 \bar{\rho}}{\mathcal{M}^4}. \quad (102)$$

### B. Perturbations

In the Jordan frame we write the Newtonian gauge metric as

$$ds^2 = a^2[-(1 + 2\Phi)d\tau^2 + (1 - 2\Psi)d\mathbf{x}^2]. \quad (103)$$

Using  $ds^2 = A^2 d\tilde{s}^2$ , the comparison with Eq.(88) leads to

$$\Phi = \tilde{\Phi} + \delta \ln A, \quad \Psi = \tilde{\Psi} - \delta \ln A, \quad (104)$$

at linear order in  $\delta A$ , while the Einstein-frame Poisson equation (89) also reads as

$$2M_{\text{Pl}}^2 \frac{\nabla^2 \tilde{\Psi}}{a^2} = \frac{\delta(A^4 \rho) - \mathcal{M}^4 \delta\tilde{\chi}}{A^4}. \quad (105)$$

Since we wish the deviations from General Relativity and the  $\Lambda$ -CDM cosmology to be small, at most of the order

of ten percent, the potentials  $\Phi$  and  $\Psi$  cannot deviate too much from the Jordan-frame Newtonian potential,  $\Phi \simeq \Psi \simeq \Psi_N$ . From Eq.(104) this implies that  $\delta \ln A$  is smaller than the typical value of the Newtonian potential. Since  $|\Psi_N|$  is typically of order  $10^{-5}$ , over cosmological and astrophysical scales, we can indeed linearize in  $\delta A$  and we must have

$$|\delta \ln A| \lesssim 10^{-6}, \quad \text{hence} \quad |A - 1| \lesssim 10^{-6}, \quad (106)$$

where we choose unity as the reference value of  $A$ . Then, we can simplify the Poisson equation (105) as,

$$\frac{\nabla^2 \Psi_N}{a^2} = \frac{\delta \rho - \mathcal{M}^4 \delta \tilde{\chi}}{2M_{\text{Pl}}^2}, \quad (107)$$

which defines a modified Newtonian potential, and the Jordan metric potentials read from Eq.(104) as

$$\Phi = \Psi_N + \delta \ln A, \quad \Psi = \Psi_N - \delta \ln A. \quad (108)$$

In the Jordan frame, both the matter and radiation components obey the standard equations of motion. This gives for the matter component the continuity and Euler equations

$$\frac{\partial \rho}{\partial \tau} + (\mathbf{v} \cdot \nabla) \rho + (3\mathcal{H} + \nabla \cdot \mathbf{v}) \rho = 0, \quad (109)$$

and

$$\frac{\partial \mathbf{v}}{\partial \tau} + (\mathbf{v} \cdot \nabla) \mathbf{v} + \mathcal{H} \mathbf{v} = -\nabla \Phi. \quad (110)$$

The scalar field equation of motion (71) simplifies as

$$\frac{d \ln A}{d \tilde{\chi}} = \frac{\mathcal{M}^4}{\rho}, \quad (111)$$

which also gives

$$\nabla \ln A = \frac{d \ln A}{d \tilde{\chi}} \nabla \tilde{\chi} = \frac{\mathcal{M}^4}{\rho} \nabla \tilde{\chi}, \quad (112)$$

and the Euler equation also writes as

$$\frac{\partial \mathbf{v}}{\partial \tau} + (\mathbf{v} \cdot \nabla) \mathbf{v} + \mathcal{H} \mathbf{v} = -\nabla \Psi_N - \frac{\nabla p_A}{\rho}, \quad (113)$$

with

$$p_A = \mathcal{M}^4 c^2 \tilde{\chi}, \quad (114)$$

where we explicitly wrote the factor  $c^2$ .

Thus, in terms of the matter dynamics, the modified-gravity effects appear through two factors, a) the modification of the Poisson equation (107), due to the additional source associated with the scalar-field energy density fluctuations, but this effect will turn out to be negligible, and b) the new pressure-like term  $p_A$  in the Euler equation (113). This pressure  $p_A$  corresponds to a polytropic equation of state, as it only depends on the matter density (the sum of cold dark matter and baryons), through Eq.(111) which implicitly determines  $\tilde{\chi}$  as a function of  $\rho$ .

### C. Linear growing mode

On large scales or at early times we may linearize the equations of motion. Expanding the coupling function  $A(\tilde{\chi})$  as

$$\ln A(\tilde{\chi}) = \ln \bar{A} + \sum_{n=1}^{\infty} \frac{\beta_n(\tau)}{n!} (\delta \tilde{\chi})^n, \quad (115)$$

the scalar field equation (111) gives at the background and linear orders

$$\beta_1 = \frac{\mathcal{M}^4}{\bar{\rho}} > 0, \quad \delta \tilde{\chi} = -\frac{\beta_1}{\beta_2} \delta, \quad (116)$$

where we note  $\delta \equiv \delta \rho / \bar{\rho}$  the matter density contrast. The continuity equation (109) reads as  $\partial_\tau \delta + \nabla \cdot [(1 + \delta) \mathbf{v}] = 0$  in terms of the density contrast. Combining with the Euler equation at linear order, this gives

$$\frac{\partial^2 \delta}{\partial \tau^2} + \mathcal{H} \frac{\partial \delta}{\partial \tau} + \epsilon_1 c^2 \nabla^2 \delta = \frac{\bar{\rho} a^2}{2M_{\text{Pl}}^2} (1 + \epsilon_1) \delta, \quad (117)$$

where we introduced

$$\epsilon_1(\tau) \equiv \frac{\beta_1}{\beta_2} \frac{\mathcal{M}^4}{\bar{\rho}} = \frac{\beta_1^2}{\beta_2}. \quad (118)$$

As compared with the  $\Lambda$ -CDM cosmology, the pressure-like term  $\nabla^2 \delta$  introduces an explicit scale dependence. Going to Fourier space, the linear modes  $D(k, \tau)$  now depend on the wave number  $k$  and obey the evolution equation

$$\frac{\partial^2 D}{\partial (\ln a)^2} + \left( 2 + \frac{1}{H^2} \frac{dH}{dt} \right) \frac{\partial D}{\partial \ln a} - \frac{3\Omega_m}{2} (1 + \epsilon) D = 0, \quad (119)$$

where  $H = d \ln a / dt$  is the Jordan-frame expansion rate (with respect to the Jordan-frame cosmic time  $t$ ) and the factor  $\epsilon(k, t)$ , which describes the deviation from the  $\Lambda$ -CDM cosmology, is given by

$$\epsilon(k, \tau) = \epsilon_1(\tau) \left( 1 + \frac{2}{3\Omega_m} \frac{c^2 k^2}{a^2 H^2} \right). \quad (120)$$

Thus, the two effects of the scalar field, the contribution to the gravitational potential from  $\delta \rho_{\tilde{\chi}}$  and the pressure-like term associated with the conformal transformation (4), modify the growth of structures in the same direction, given by the sign of  $\epsilon_1$ . A positive  $\epsilon_1$  gives a scale-dependent amplification of the gravitational force and an acceleration of gravitational clustering. The  $k$ -dependent pressure-like term dominates when  $ck/aH > 1$ , that is, on subhorizon scales. Moreover, we have  $(ck/aH)^2 \sim 10^7$  today at scales of about  $1 h^{-1} \text{Mpc}$ . Therefore, we must have

$$|\epsilon_1| \lesssim 10^{-7} \quad (121)$$

to ensure that the growth of large-scale structures is not too significantly modified. Moreover, the fluctuations of

the scalar field energy density in the Poisson equations are negligible, as the factor  $\epsilon_1$  is negligible with respect to unity in the right-hand side in Eq.(117).

From the definitions of  $\beta_1$  and  $\beta_2$ , taking the derivative with respect to the scale factor  $a$  of the first Eq.(116) gives

$$\epsilon_2 = \frac{3\beta_1^2}{\beta_2} = 3\epsilon_1, \quad (122)$$

where  $\epsilon_2$  was defined in Eq.(92). Therefore, we find from the condition (121) that  $\epsilon_2$  is also very small,  $|\epsilon_2| \lesssim 10^{-7}$ ,

$$|\epsilon_2| = \left| \frac{d \ln \bar{A}}{d \ln a} \right| \lesssim 10^{-7}. \quad (123)$$

We recover the condition (106) that  $A$  remains very close to unity. This also implies that the Einstein and Jordan frames are very close.

#### D. Comparison with ultralocal models

The equations of motion that we have obtained in section V in the Jordan frame are identical to those associated with the ultralocal models introduced in [14], if we make the change  $\tilde{\chi} - 1 \rightarrow \tilde{\chi}$ . The factor  $-1$  comes from the explicit introduction of a cosmological constant in the Lagrangian (5), which was not needed for the ultralocal models as any constant shift could be absorbed within the definition of  $\tilde{\chi}$ .

We have recalled the definition of the ultralocal models in section IID. In particular, we noticed that apart from the factor  $-1$ , we recover the Lagrangian (5),  $\tilde{\mathcal{L}}_{\tilde{\chi}}(\tilde{\chi}) = \mathcal{M}^4 \tilde{\chi}$ , and the conformal coupling  $A(\tilde{\chi})$ . However, whereas for the kinetic conformal coupling models that we study in this paper  $\tilde{\chi}$  is the kinetic term (4) of an underlying scalar field  $\varphi$ , for the ultralocal models  $\tilde{\chi}$  is a standard scalar field on its own. These two different meanings of  $\tilde{\chi}$  lead to some differences in the detailed behavior of some quantities. First, for the ultralocal models the relation between the Einstein- and Jordan-frame matter energy-momentum tensors takes the standard form,

$$\text{ultralocal: } \tilde{T}_{\mu\nu} = A^2 T_{\mu\nu}, \quad (124)$$

and the nonconservation equation for the Einstein-frame matter energy-momentum tensor also takes the standard form

$$\text{ultralocal: } \tilde{\nabla}_\mu \tilde{T}_\nu^\mu = \tilde{T} \partial_\nu \ln A, \quad (125)$$

in contrast with Eqs.(60) and (64). Second, the Einstein-frame scalar-field energy-momentum tensor reads as

$$\text{ultralocal: } \tilde{T}_{\varphi;\mu\nu} = \mathcal{M}^4 \tilde{\chi} \tilde{g}_{\mu\nu}, \quad (126)$$

instead of Eq.(67), where we can see a sign of the change  $\tilde{\chi} - 1 \rightarrow \tilde{\chi}$  between both models, and the equation of motion of the scalar field reads as

$$\text{ultralocal: } 1 + \frac{\tilde{T}}{\mathcal{M}^4} \frac{d \ln A}{d \tilde{\chi}} = 0, \quad (127)$$

instead of Eq.(66). The latter equation admits the new solution  $\varphi = \text{constant}$ , and the other solution (71) is only identical to Eq.(127) if we replace in the latter  $\tilde{T}$  by  $A^4 T$  [and not if we express  $T$  in terms of  $\tilde{T}$  in Eq.(71)]. On the other hand, this remark already shows that the two models are more closely related if we work in Jordan frame. Third, in the Einstein-frame Friedmann equation (81) it is  $-\mathcal{M}^4 \tilde{\chi}$  instead of  $\mathcal{M}^4 (\tilde{\chi} + 1)$  that enters the right-hand side. However, the Poisson equation (89) takes the same form, because of a cancellation between the changes of the matter and scalar-field energy densities between the two models, related to the simplification (73).

Despite these differences between both models in the Einstein frame, we recover almost the same equations of motion in the Jordan frame. For the ultralocal models we recover the Friedmann equation (98), where  $-\bar{p}_\varphi = \mathcal{M}^4 (1 - \tilde{\chi})$  is replaced by  $-\mathcal{M}^4 \tilde{\chi}$  and the background scalar-field equation of motion is again given by Eq.(100). At the perturbative level we obtain the same Poisson equation (107), which implies that the equations of motion of matter particles and of fluids are the same because they follow the geodesics of the Jordan metric  $g_{\mu\nu}$  in both models.

Therefore, if we work in the Jordan frame, the only difference between the two models is that for the kinetic conformal coupling case studied in this paper we have the additional constraint that  $\tilde{\chi}$  must be interpreted as the kinetic term of an underlying scalar field  $\varphi$ . Neglecting the metric fluctuations this reads as

$$\text{kinetic coupling: } \tilde{\chi} = \frac{1}{2\mathcal{M}^4 a^2} \left[ \left( \frac{\partial \varphi}{\partial \tau} \right)^2 - (\nabla \varphi)^2 \right], \quad (128)$$

where we used again  $\bar{A} \simeq 1$ . Even though the field  $\varphi$  does not appear in the Jordan-frame equations of motion, it cannot be ignored as the requirement that  $\tilde{\chi}$  can be written in the form (128) entails new constraints on the model. Indeed, Eq.(128) implies at once that at the background level we have  $\tilde{\chi} \geq 0$ , as in Eq.(78). This is actually the reason why we had to introduce an explicit cosmological constant in the Lagrangian (5) through the factor  $-\mathcal{M}^4$ . Indeed, the scalar-field contribution to the Friedmann equation (95) is  $-\bar{p}_\varphi = \mathcal{M}^4 (1 - \tilde{\chi})$ . Without the unit factor we obtain the contribution  $-\mathcal{M}^4 \tilde{\chi} \leq 0$ , which can never give rise to an accelerated expansion as it is negative. In contrast, in the ultralocal models there is no *a priori* restriction on the sign of  $\tilde{\chi}$  [any constant shift can actually be absorbed by a change of the coupling function  $A(\tilde{\chi})$ ], and we could obtain an accelerated expansion by building models where  $\tilde{\chi}$  is negative in the late Universe. For the kinetic conformal coupling model studied in this paper we need the unit factor in Eq.(5), which can be interpreted as a standard cosmological constant or as the value of the potential  $V(\varphi)$ , which is approximated as a constant on the scales of interest, or is exactly constant at low energy within the Goldstone models described in section IIB 1.

## VI. THE SCALAR FIELD $\varphi$ AS A FUNCTION OF ITS KINETIC TERM $\tilde{\chi}$

We have seen above that the behavior of the system can be written in terms of  $\tilde{\chi}$  only. This also allows us to recover the dynamics of the ultralocal models. However, to be considered as a solution associated with the kinetic conformal coupling action (3), we must check that the field  $\tilde{\chi}(\tau, \mathbf{x})$  obtained from these equations of motion can also be written as the kinetic term of a scalar field  $\varphi(\tau, \mathbf{x})$ . Therefore, we must integrate Eq.(128) for  $\varphi$ . This was done in Eq.(101) at the background level, but we must generalize this result to the perturbed Universe.

We recall that at the background level we have from Eq.(78) the condition  $\tilde{\chi} \geq 0$ , while the equation of motion of the background scalar field (100) simplifies as

$$\frac{d \ln \bar{A}}{d \tilde{\chi}} = \frac{\mathcal{M}^4}{\bar{\rho}}, \quad (129)$$

where we used  $\bar{A} \simeq 1$  from Eq.(106). We require that this equation always has a solution, for any density  $\bar{\rho}$ . This means that  $d \ln A / d \tilde{\chi}$  covers the full positive semiaxis over some range  $]\tilde{\chi}_-, \tilde{\chi}_+[$  of  $\tilde{\chi}$  with  $\tilde{\chi}_- \geq 0$ ,

$$\frac{d \ln A}{d \tilde{\chi}} (]\tilde{\chi}_-, \tilde{\chi}_+[) = ]0, +\infty[ \quad \text{with} \quad \tilde{\chi}_- \geq 0. \quad (130)$$

Then, to avoid multiple solutions and discontinuities, we restrict the general solution  $\tilde{\chi}(\rho)$  of the scalar-field equation of motion (111) to this interval  $]\tilde{\chi}_-, \tilde{\chi}_+[$ . Thus, we require that  $\tilde{\chi}(\rho)$  is an invertible function of  $\rho$  from  $]0, +\infty[$  to  $]\tilde{\chi}_-, \tilde{\chi}_+[$  with  $\tilde{\chi}_- \geq 0$ . Then, the constraint  $\tilde{\chi} \geq 0$  implies from Eq.(128)

$$\tilde{\chi} \geq 0 \quad \text{and} \quad \left| \frac{\partial \varphi}{\partial \tau} \right| \geq |\nabla \varphi|. \quad (131)$$

Therefore, in contrast with most scalar-field modified-gravity models, the scalar field can never reach a quasi-static limit (defined as  $|\partial \varphi / \partial \tau| \ll |\nabla \varphi|$ ), even on small astrophysical scales such as the Solar System.

We can write the solution of equation (128) as

$$\frac{\partial \varphi}{\partial \tau} = -\sqrt{2\mathcal{M}^4 a^2 \tilde{\chi} + (\nabla \varphi)^2}. \quad (132)$$

Here we can choose the negative sign because Eq.(128) is invariant under the transformation  $\varphi \rightarrow -\varphi$ . We can also choose the boundary condition,

$$\varphi(\tau = 0, \mathbf{x}) = 0, \quad (133)$$

which is consistent with the background solution (101) that applies at early times when perturbations can be neglected. Thus, we obtain the well-known Hamilton-Jacobi equation

$$\frac{\partial \varphi}{\partial \tau} + H(\tau, \mathbf{x}, \nabla \varphi) = 0, \quad (134)$$

where we introduced the time-dependent Hamiltonian

$$H(\tau, \mathbf{x}, \mathbf{p}) = \sqrt{\psi^2(\tau, \mathbf{x}) + \mathbf{p}^2}, \quad (135)$$

with

$$\psi(\tau, \mathbf{x}) = \sqrt{2\mathcal{M}^4 a^2 \tilde{\chi}}. \quad (136)$$

### A. Method of characteristics

The nonlinear partial differential equation (134) can be solved by the method of characteristics, see [25]. This allows us to compute  $\varphi$  along curves  $x(s) = (\tau(s), \mathbf{x}(s))$ , with the parametric coordinate  $s$ . Defining

$$p_0(s) = \frac{\partial \varphi}{\partial \tau}[x(s)], \quad \mathbf{p}(s) = \nabla \varphi[x(s)], \quad (137)$$

the characteristic curves of Eq.(134) are given by

$$\frac{d\tau}{ds} = 1, \quad \frac{d\mathbf{x}}{ds} = \frac{\partial H}{\partial \mathbf{p}} \quad (138)$$

and

$$\frac{dp_0}{ds} = -\frac{\partial H}{\partial \tau}, \quad \frac{d\mathbf{p}}{ds} = -\frac{\partial H}{\partial \mathbf{x}}. \quad (139)$$

Thanks to the first equation (138) we can identify  $s$  with the time  $\tau$ ,  $\tau(s) = s$ . Then, the characteristic curves are given by the Hamilton equations,

$$\frac{d\mathbf{x}}{d\tau} = \frac{\partial H}{\partial \mathbf{p}}, \quad \frac{d\mathbf{p}}{d\tau} = -\frac{\partial H}{\partial \mathbf{x}}, \quad (140)$$

while the scalar field along the curve is given by the integration of

$$\frac{d\varphi}{d\tau} = p_0 + \frac{\partial H}{\partial \mathbf{p}} \cdot \mathbf{p} = -H + \frac{\partial H}{\partial \mathbf{p}} \cdot \mathbf{p}, \quad (141)$$

with the boundary condition (133). For the Hamiltonian (135) the characteristic curves read as

$$\frac{d\mathbf{x}}{d\tau} = \frac{\mathbf{p}}{\sqrt{\psi^2 + \mathbf{p}^2}}, \quad \frac{d\mathbf{p}}{d\tau} = -\frac{\psi}{\sqrt{\psi^2 + \mathbf{p}^2}} \nabla \psi, \quad (142)$$

$$\frac{d\varphi}{d\tau} = -\frac{\psi^2}{\sqrt{\psi^2 + \mathbf{p}^2}}. \quad (143)$$

For any initial point  $\mathbf{x}(0)$ , with  $\mathbf{p}(0) = 0$ , at  $\tau = 0$ , this method allows us to obtain a local solution  $\varphi(\tau, \mathbf{x})$  around the starting point until some finite time  $\tau > 0$ . In particular, in the homogeneous case we recover the background solution (101) (where we took  $\bar{A} \simeq 1$ ), with  $\mathbf{x}(\tau) = \mathbf{x}(0)$  and  $\mathbf{p}(\tau) = 0$ . However, it is well-known that in the general case this procedure cannot extend to all space, as different characteristics may intersect, which would lead to different values of  $\varphi$  at those points. This means that the initial-value problem (134) does not in general have a smooth solution, existing for all times  $\tau > 0$  [25].

## B. Viscosity solution

Fortunately, it is possible to extend the local solutions obtained by the method of characteristics to a unique generalized or weak solution, also called “viscosity” solution [26, 27]. Indeed, the Hamiltonian (135) is bounded from below (by 0), we can also assume that  $H(\tau, \mathbf{x}, 0)$  is bounded from above (e.g., if  $\tilde{\chi}_+$  is finite) and that  $|\partial\psi/\partial x|$  is bounded. Then, as  $H(\tau, \mathbf{x}, \mathbf{p})$  is convex in  $\mathbf{p}$ , this ensures that there exists a unique viscosity solution of the Hamilton-Jacobi equation (134), which is given by the explicit expression [28, 29]

$$\varphi(\tau, \mathbf{x}) = \min_{\mathbf{q}(s)} \left\{ \int_0^\tau ds L(s, \mathbf{q}(s), \dot{\mathbf{q}}(s)) \mid \mathbf{q}(\tau) = \mathbf{x} \right\}, \quad (144)$$

where we used the boundary condition (133),  $\varphi(0, \mathbf{x}) = 0$ . Here we take the minimum over all paths  $\mathbf{q}(s)$  that are of class  $C^2$ , start at any point  $\mathbf{x}(0)$  on the boundary surface  $\tau = 0$ , and end at the point  $(\tau, \mathbf{x})$ . We also introduced the Lagrangian  $L(\tau, \mathbf{x}, \mathbf{v})$  defined by

$$L(\tau, \mathbf{x}, \mathbf{v}) = \sup_{\mathbf{p}} [\mathbf{v} \cdot \mathbf{p} - H(\tau, \mathbf{x}, \mathbf{p})]. \quad (145)$$

Thus, as could be expected the solution of the Hamilton-Jacobi equation (134) is the action, defined by the Hamiltonian  $H$  or the Lagrangian  $L$ . The viscosity solution (144) can also be obtained as the limit  $\epsilon \rightarrow 0$  when we add a small viscous term  $\epsilon \nabla^2 \varphi$  to the Hamilton-Jacobi equation (134) [28]. The viscosity solution (144) is Lipschitz continuous with a gradient that is piecewise smooth, undergoing jump discontinuities along surfaces of dimension three (in spacetime) [28, 29].

The Hamiltonian and the Lagrangian are related by the usual Legendre transform, with

$$\mathbf{v} = \frac{\partial H}{\partial \mathbf{p}}, \quad \mathbf{p} = \frac{\partial L}{\partial \mathbf{v}}. \quad (146)$$

Thanks to the convexity of  $H$  in  $\mathbf{p}$ , the Lagrangian is also convex in  $\mathbf{v}$ , both the Hamiltonian and the Lagrangian are actually Legendre transforms of each other, and from Eq.(135) we obtain the explicit expressions

$$|\mathbf{v}| < 1, \quad \mathbf{v} = \frac{\mathbf{p}}{\sqrt{\psi^2 + \mathbf{p}^2}}, \quad \mathbf{p} = \frac{\psi \mathbf{v}}{\sqrt{1 - \mathbf{v}^2}}, \quad (147)$$

$$L(\tau, \mathbf{x}, \mathbf{v}) = -\psi(\tau, \mathbf{x}) \sqrt{1 - \mathbf{v}^2}. \quad (148)$$

Whereas  $|\mathbf{p}|$  is unbounded we have  $|\mathbf{v}| < 1$ . This ensures that causality is satisfied as the paths in the minimization (144) cannot travel faster than light. The paths that minimize Eq.(144) also satisfy the Euler-Lagrange equations defined by the Lagrangian  $L$ . Since  $\psi \geq 0$  we can also write the solution (144) as

$$\varphi(\tau, \mathbf{x}) = -\max_{\mathbf{q}(s)} \left\{ \int_0^\tau ds \psi(s) \sqrt{1 - \mathbf{v}^2(s)} \mid \mathbf{q}(\tau) = \mathbf{x} \right\}, \quad (149)$$

where we wrote  $\psi(s) = \psi(s, \mathbf{q}(s))$  and  $\mathbf{v}(s) = \dot{\mathbf{q}}(s)$  for each path. We can intuitively figure out the behavior of  $\varphi(\mathbf{x})$  from the explicit maximization (149). Neglecting the time-dependence of  $\psi$ , we can see that for a given location  $\mathbf{x}$  the maximization selects the paths that spend most time over the maximum  $\psi_{\max}$  within the horizon. Local maxima  $\psi_{\max}^{(i)}$  (i.e., within the horizon scale) thus define attraction basins, or cells such as Voronoi diagrams. Within each cell  $\varphi(\mathbf{x})$  is regular, and at the boundary between two cells we change of attractor  $\psi_{\max}^{(i)}$ . Then,  $\varphi$  remains continuous at the boundary [this defines the boundary; if there were a jump, we could get a higher maximum in Eq.(149) on the lower side by extending paths that come from the upper side] but its gradient is discontinuous. Taking into account the finite velocity and the time dependence makes the solution more intricate than standard Voronoi diagrams, but theorems ensure that the viscosity solution is continuous with a piecewise smooth gradient that shows jump discontinuities [28, 29]. These are rather mild singularities, in particular the gradient does not show Dirac-type singularities. Moreover, the Lorentz kinetic term (128), from which we obtain  $\varphi$ , is as smooth as the density field and does not show jumps if we take the density to be continuous.

For the background case, we again recover the solution (101) and the path obtained below Eq.(143) by the method of characteristics. Indeed, since  $\psi(\tau)$  only depends on time and is positive, the maximization of Eq.(149) corresponds to  $\mathbf{v} = 0$  (to maximize the square-root factor at all intermediate times  $s$ ). This gives again the motionless path  $\mathbf{x}(s) = \mathbf{x}(\tau) = \mathbf{x}(0)$ ,  $\mathbf{v} = \mathbf{p} = 0$ , and the integral (101).

## VII. EXPLICIT MODELS

We have seen in section VD that we recover the equations of motion of the ultralocal models studied in [14]. Therefore, we can use their results and follow the same approach.

### A. Characteristic density $\rho_\alpha$ and redshift $z_\alpha$

To satisfy the constraints (106) we write the coupling function as

$$\ln A(\tilde{\chi}) = \alpha \lambda(\mathcal{X}) \quad \text{with} \quad \alpha \lesssim 10^{-6}, \quad 0 \leq \lambda \leq 1, \quad (150)$$

and

$$\tilde{\chi} = \gamma \mathcal{X} \quad \text{with} \quad \gamma > 0, \quad 0 \leq \mathcal{X} \leq 1. \quad (151)$$

Thus,  $\alpha$  is a small parameter that sets the magnitude of  $\ln A$ , while  $\gamma$  sets the magnitude of  $\tilde{\chi}$ . This corresponds to models where  $\tilde{\chi}$  ranges from 0 to a finite value  $\gamma > 0$ . We could also consider models where  $\tilde{\chi}$  goes up to infinity (see [14] for such a study in the case of ultralocal models),

but most of qualitative behaviors would not be modified. Then, the equation of motion (111) reads as

$$\frac{d\lambda}{d\mathcal{X}} = \frac{1}{\hat{\rho}} \quad \text{with} \quad \hat{\rho} = \frac{\alpha\rho}{\gamma\mathcal{M}^4}. \quad (152)$$

This implicitly defines the functions  $\lambda(\hat{\rho})$  and  $\mathcal{X}(\hat{\rho})$ , from the value of  $\mathcal{X}$  that solves Eq.(152) for a given density. The changes of variables  $\ln A \rightarrow \lambda$ ,  $\tilde{\chi} \rightarrow \mathcal{X}$ , and  $\rho \rightarrow \hat{\rho}$  have removed the explicit parameters  $\mathcal{M}^4 \sim \bar{\rho}_{\text{de}0}$ ,  $\alpha \lesssim 10^{-6}$ , and  $\gamma$ , so that the functions  $\lambda(\mathcal{X})$ ,  $\lambda(\hat{\rho})$  and  $\mathcal{X}(\hat{\rho})$  do not involve small nor large parameters. Therefore, in addition to the density  $\mathcal{M}^4 \sim \bar{\rho}_{\text{de}0}$ , these models automatically introduce another density scale  $\rho_\alpha$ ,

$$\rho_\alpha = \frac{\gamma\mathcal{M}^4}{\alpha} \sim \frac{\gamma\bar{\rho}_{\text{de}0}}{\alpha} \gtrsim 10^6 \gamma\bar{\rho}_{\text{de}0}, \quad \hat{\rho} = \frac{\rho}{\rho_\alpha}. \quad (153)$$

This implies that, from the point of view of the coupling function  $\ln A$ , the low-redshift mean density of the Universe is within its very low density regime if  $\gamma \gg \alpha$ . Moreover, as we shall check below, there is a cosmological transition between low-density and high-density regimes at the redshift  $z_\alpha$  where  $\bar{\rho} \sim \rho_\alpha$ , which corresponds to

$$a_\alpha \sim (\alpha/\gamma)^{1/3} \lesssim 0.01\gamma^{-1/3}, \quad z_\alpha \sim (\alpha/\gamma)^{-1/3} \gtrsim 100\gamma^{1/3}. \quad (154)$$

In the numerical computations presented in this paper, we will consider the case  $\alpha = 10^{-6}$  with  $\gamma \sim 1, 10^{-3}$ , and  $10^{-6}$ , to investigate scenarios where the transition redshift  $z_\alpha$  goes from 100 to 0.

## B. Coupling function

To define explicit models we simply need to give the explicit expression of the coupling function  $A(\tilde{\chi})$ , or of the rescaled function  $\lambda(\mathcal{X})$  of Eq.(150). From Eq.(152) we derive the properties

$$\frac{d\lambda}{d\mathcal{X}} > 0, \quad \left. \frac{d\lambda}{d\mathcal{X}} \right|_{\rho=0} = +\infty, \quad \left. \frac{d\lambda}{d\mathcal{X}} \right|_{\rho=\infty} = 0. \quad (155)$$

We also require an accelerated expansion in the late Universe, corresponding to the dark energy era. From Eqs.(98) and (94) this means that  $\bar{p}_\varphi(z=0) < 0$  and  $\tilde{\chi}(z=0) < 1$ . To have a unique and well-defined mapping  $\rho \leftrightarrow \mathcal{X}$ , the function  $d\lambda/d\mathcal{X}$  must be monotonic. Therefore, we have two choices, where  $\lambda(\mathcal{X})$  is either concave or convex.

### 1. Concave coupling function $\lambda(\mathcal{X})$

#### a. General concave case

If  $\lambda(\mathcal{X})$  is concave, the first derivative  $d\lambda/d\mathcal{X}$  is a decreasing function of  $\mathcal{X}$ , which implies that  $\mathcal{X}$  is an increasing function of  $\rho$ , and we have the asymptotic behaviors

$$\rho \rightarrow 0: \quad \tilde{\chi} \rightarrow 0, \quad \mathcal{X} \rightarrow 0, \quad \frac{d\lambda}{d\mathcal{X}} \rightarrow +\infty, \quad (156)$$

$$\rho \rightarrow \infty: \quad \tilde{\chi} \rightarrow \gamma, \quad \mathcal{X} \rightarrow 1, \quad \frac{d\lambda}{d\mathcal{X}} \rightarrow 0. \quad (157)$$

In the following we consider power-law behaviors at these boundaries,

$$\begin{aligned} \mathcal{X} \rightarrow 0: \quad & \frac{d\lambda}{d\mathcal{X}} \sim \mathcal{X}^{\mu_- - 1} \quad \text{with} \quad 0 < \mu_- < 1, \\ \hat{\rho} \ll 1: \quad & \mathcal{X} \sim \hat{\rho}^{1/(1-\mu_-)}, \end{aligned} \quad (158)$$

and

$$\begin{aligned} \mathcal{X} \rightarrow 1: \quad & \frac{d\lambda}{d\mathcal{X}} \sim (1-\mathcal{X})^{\mu_+ - 1} \quad \text{with} \quad \mu_+ > 1, \\ \hat{\rho} \gg 1: \quad & 1-\mathcal{X} \sim \hat{\rho}^{-1/(\mu_+ - 1)}. \end{aligned} \quad (159)$$

From Eqs.(94) and (98), we find that at early and late times the dark energy density behaves as

$$z \gg z_\alpha: \quad \tilde{\chi} \rightarrow \gamma, \quad \bar{\rho}_{\text{de}} \rightarrow (1-\gamma)\mathcal{M}^4, \quad (160)$$

$$z \ll z_\alpha: \quad \tilde{\chi} \rightarrow 0, \quad \bar{\rho}_{\text{de}} \rightarrow \mathcal{M}^4. \quad (161)$$

Thus, the dark energy density grows with time. If  $\gamma \gg \alpha$  we have seen that the transition redshift  $z_\alpha$  is very large, so that Eq.(161) implies  $\mathcal{M}^4 = \bar{\rho}_{\text{de}0}$ . If  $\gamma \lesssim \alpha \ll 1$  the dark energy density is almost constant and very close to  $\mathcal{M}^4$ . Therefore, in all cases we obtain

$$\text{concave:} \quad \mathcal{M}^4 = \bar{\rho}_{\text{de}0}, \quad \hat{\rho} = \frac{\alpha\rho}{\gamma\bar{\rho}_{\text{de}0}}, \quad (162)$$

and the dark energy density is almost constant and positive at low  $z$ . This sets the energy scale  $\mathcal{M}$  in terms of the dark energy density today.

To study the evolution of linear matter perturbations in Eq.(119) we need the factor  $\epsilon_1(\tau)$ . From the definitions (115) and (118) we have

$$\beta_1 = \frac{\alpha}{\gamma} \frac{d\lambda}{d\mathcal{X}}, \quad \beta_2 = \frac{\alpha}{\gamma^2} \frac{d^2\lambda}{d\mathcal{X}^2}, \quad \epsilon_1 = \alpha \frac{(d\lambda/d\mathcal{X})^2}{d^2\lambda/d\mathcal{X}^2}. \quad (163)$$

Like the coupling function  $\ln A$ , the amplitude  $\epsilon_1$  is proportional to  $\alpha$  and does not depend on  $\gamma$ . Thus, the small value of the parameter  $\alpha$  simultaneously ensures that the constraints (106) and (121) are satisfied. For a concave coupling function  $\lambda$  we have

$$\lambda \text{ concave:} \quad \beta_1 > 0, \quad \beta_2 < 0, \quad \epsilon_1 < 0. \quad (164)$$

This means that concave coupling functions imply a slower growth of large-scale structures than the  $\Lambda$ -CDM cosmology. At high redshift we obtain for the power-law models (159)

$$z \gg z_\alpha: \quad \epsilon_1 \sim -\alpha(1-\tilde{\chi})^{\mu_+} \sim -\alpha(a/a_\alpha)^{3\mu_+/(1-\mu_+)}, \quad (165)$$

while at low redshift the power-law models (158) give

$$z \ll z_\alpha: \quad \epsilon_1 \sim -\alpha\tilde{\chi}^{\mu_-} \sim -\alpha(a/a_\alpha)^{-3\mu_-/(1-\mu_-)}. \quad (166)$$

Thus, the amplitude  $|\epsilon_1(\tau)|$  peaks at the transition redshift  $z_\alpha$ , with power-law decays at higher and lower redshifts, and

$$\epsilon_1(z_\alpha) \sim -\max(|\epsilon_1|) \sim -\alpha. \quad (167)$$

b. *A simple explicit concave model*

For illustration, in the numerical computations presented in this paper we choose the simple coupling function

$$0 \leq \mathcal{X} \leq 1: \quad \lambda(\mathcal{X}) = \sqrt{\mathcal{X}(2 - \mathcal{X})}, \quad (168)$$

which we display in Fig. 1. This corresponds to the exponents

$$\mu_- = 1/2, \quad \mu_+ = 2, \quad (169)$$

the density and the scalar-field kinetic term are related by

$$\hat{\rho} = \frac{\sqrt{\mathcal{X}(2 - \mathcal{X})}}{1 - \mathcal{X}}, \quad \mathcal{X} = 1 - \frac{1}{\sqrt{\hat{\rho}^2 + 1}}, \quad (170)$$

which gives

$$\lambda = \frac{\hat{\rho}}{\sqrt{\hat{\rho}^2 + 1}}, \quad \frac{d\lambda}{d \ln \rho} = \frac{\hat{\rho}}{(\hat{\rho}^2 + 1)^{3/2}},$$

$$\epsilon_1 = -\alpha \frac{\hat{\rho}}{(\hat{\rho}^2 + 1)^{3/2}}. \quad (171)$$

2. *Convex coupling function  $\lambda(\tilde{\chi})$*

a. *General convex case*

If  $\lambda(\mathcal{X})$  is convex, the first derivative  $d\lambda/d\mathcal{X}$  is an increasing function of  $\mathcal{X}$ , which implies that  $\mathcal{X}$  is a decreasing function of  $\rho$ , and we have the asymptotic behaviors

$$\rho \rightarrow 0: \quad \tilde{\chi} \rightarrow \gamma, \quad \mathcal{X} \rightarrow 1, \quad \frac{d\lambda}{d\mathcal{X}} \rightarrow +\infty, \quad (172)$$

$$\rho \rightarrow \infty: \quad \tilde{\chi} \rightarrow 0, \quad \mathcal{X} \rightarrow 0, \quad \frac{d\lambda}{d\mathcal{X}} \rightarrow 0. \quad (173)$$

We again focus on power-law behaviors at these boundaries,

$$\mathcal{X} \rightarrow 0: \quad \frac{d\lambda}{d\mathcal{X}} \sim \mathcal{X}^{\mu_+ - 1} \quad \text{with } \mu_+ > 1,$$

$$\hat{\rho} \gg 1: \quad \mathcal{X} \sim \hat{\rho}^{-1/(\mu_+ - 1)}, \quad (174)$$

and

$$\mathcal{X} \rightarrow 1: \quad \frac{d\lambda}{d\mathcal{X}} \sim (1 - \mathcal{X})^{\mu_- - 1} \quad \text{with } 0 < \mu_- < 1,$$

$$\hat{\rho} \ll 1: \quad 1 - \mathcal{X} \sim \hat{\rho}^{1/(1 - \mu_-)}. \quad (175)$$

From Eqs.(94) and (98), we find that at early and late times the dark energy density behaves as

$$z \gg z_\alpha: \quad \tilde{\chi} \rightarrow 0, \quad \bar{\rho}_{\text{de}} \rightarrow \mathcal{M}^4, \quad (176)$$

$$z \ll z_\alpha: \quad \tilde{\chi} \rightarrow \gamma, \quad \bar{\rho}_{\text{de}} \rightarrow (1 - \gamma)\mathcal{M}^4. \quad (177)$$

Thus, the dark energy density decreases with time. If  $\gamma \gg \alpha$  the transition redshift  $z_\alpha$  is very large and Eq.(177) implies  $\mathcal{M}^4 = \bar{\rho}_{\text{de}0}/(1 - \gamma)$ . If  $\gamma \lesssim \alpha \ll 1$  the dark energy density is almost constant and very close to  $\mathcal{M}^4 \simeq (1 - \gamma)\mathcal{M}^4$ . Therefore, in all cases we obtain

$$\text{convex: } \mathcal{M}^4 = \frac{\bar{\rho}_{\text{de}0}}{1 - \gamma}, \quad \hat{\rho} = \frac{\alpha(1 - \gamma)\rho}{\gamma\bar{\rho}_{\text{de}0}}. \quad (178)$$

In particular, for the convex models we obtain an upper bound on the parameter  $\gamma$ ,

$$\lambda \text{ convex: } \quad \gamma < 1, \quad (179)$$

so that the dark energy density today is positive. Then, the dark energy density is almost constant and positive at low  $z$ .

For a convex coupling function  $\lambda$  we have

$$\lambda \text{ convex: } \quad \beta_1 > 0, \quad \beta_2 > 0, \quad \epsilon_1 > 0. \quad (180)$$

This means that convex coupling functions imply a faster growth of large-scale structures than the  $\Lambda$ -CDM cosmology. At high redshift we obtain for the power-law models (174)

$$z \gg z_\alpha: \quad \epsilon_1 \sim \alpha \bar{\mathcal{X}}^{\mu_+} \sim \alpha (a/a_\alpha)^{3\mu_+ / (\mu_+ - 1)}, \quad (181)$$

while at low redshift the power-law models (175) give

$$z \ll z_\alpha: \quad \epsilon_1 \sim \alpha (1 - \bar{\mathcal{X}})^{\mu_-} \sim \alpha (a/a_\alpha)^{-3\mu_- / (1 - \mu_-)}. \quad (182)$$

Thus,  $\epsilon_1(\tau)$  again peaks at the transition redshift  $z_\alpha$ , with power-law decays at higher and lower redshifts, and

$$\epsilon_1(z_\alpha) \sim \max(\epsilon_1) \sim \alpha. \quad (183)$$

b. *A simple explicit convex model*

For the numerical computations we choose the simple coupling function

$$0 \leq \mathcal{X} \leq 1: \quad \lambda(\mathcal{X}) = 1 - \sqrt{1 - \mathcal{X}^2}, \quad (184)$$

which we display in Fig. 1. This again corresponds to the exponents

$$\mu_- = 1/2, \quad \mu_+ = 2, \quad (185)$$

the density and the scalar-field kinetic term are related by

$$\hat{\rho} = \frac{\sqrt{1 - \mathcal{X}^2}}{\mathcal{X}}, \quad \mathcal{X} = \frac{1}{\sqrt{\hat{\rho}^2 + 1}}, \quad (186)$$

which gives

$$\lambda = 1 - \frac{\hat{\rho}}{\sqrt{\hat{\rho}^2 + 1}}, \quad \frac{d\lambda}{d \ln \rho} = -\frac{\hat{\rho}}{(\hat{\rho}^2 + 1)^{3/2}},$$

$$\epsilon_1 = \alpha \frac{\hat{\rho}}{(\hat{\rho}^2 + 1)^{3/2}}. \quad (187)$$

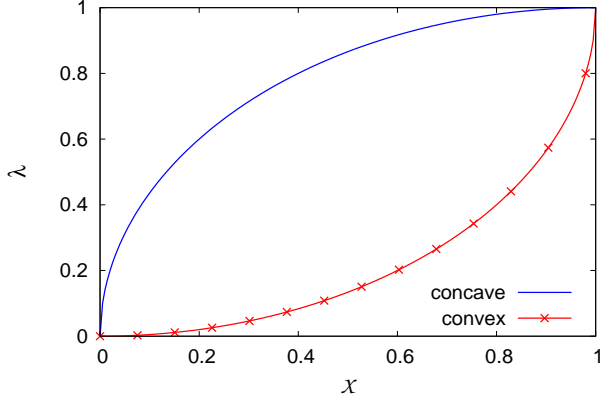


FIG. 1: Normalized coupling functions  $\lambda(\mathcal{X})$  for the concave and convex models of Eqs.(168) and (184) used in the numerical computations.

### 3. Common high-density and low-density behaviors

At high densities, which corresponds to

$$\rho \gg \rho_\alpha, \quad \hat{\rho} \gg 1, \quad \frac{d\lambda}{d\mathcal{X}} \ll 1, \quad (188)$$

in Eq.(152), both the concave and convex models introduced in Eqs.(159) and (174) satisfy

$$\frac{d\lambda}{d\mathcal{X}} \sim |\mathcal{X} - \mathcal{X}_+|^{\mu_+ - 1}, \quad \mu_+ > 1, \quad |\mathcal{X} - \mathcal{X}_+| \ll 1, \quad (189)$$

with  $\mathcal{X}_+ = 1$  or 0. This gives

$$|\mathcal{X} - \mathcal{X}_+| \sim \hat{\rho}^{-1/(\mu_+ - 1)}, \quad \left| \frac{d\lambda}{d \ln \rho} \right| \sim \hat{\rho}^{-\mu_+ / (\mu_+ - 1)}. \quad (190)$$

At low densities, which corresponds to

$$\rho \ll \rho_\alpha, \quad \hat{\rho} \ll 1, \quad \frac{d\lambda}{d\mathcal{X}} \gg 1, \quad (191)$$

in Eq.(152), both the concave and convex models introduced in Eqs.(158) and (175) satisfy

$$\frac{d\lambda}{d\mathcal{X}} \sim |\mathcal{X} - \mathcal{X}_-|^{\mu_- - 1}, \quad 0 < \mu_- < 1, \quad |\mathcal{X} - \mathcal{X}_-| \ll 1, \quad (192)$$

with  $\mathcal{X}_- = 0$  or 1. This gives

$$|\mathcal{X} - \mathcal{X}_-| \sim \hat{\rho}^{1/(1 - \mu_-)}, \quad \left| \frac{d\lambda}{d \ln \rho} \right| \sim \hat{\rho}^{\mu_- / (1 - \mu_-)}. \quad (193)$$

## VIII. STABILITY OF THE SCALAR-FIELD SOLUTION

As we explained in section IV C, we focus on the solution (71) of the scalar-field equation of motion (66). We

now check that this solution is stable, for the cosmological background. We consider a small perturbation  $\delta\varphi$  around the solution  $\bar{\varphi}$  of Eq.(71),

$$\varphi = \bar{\varphi} + \delta\varphi, \quad \tilde{\chi} = \bar{\tilde{\chi}} + \delta\tilde{\chi}, \quad (194)$$

with, at linear order,

$$\bar{\tilde{\chi}} = \frac{1}{2\mathcal{M}^4 \bar{a}^2} \left( \frac{d\bar{\varphi}}{d\tau} \right)^2, \quad \delta\tilde{\chi} = \frac{1}{\mathcal{M}^4 \bar{a}^2} \frac{d\bar{\varphi}}{d\tau} \frac{\partial \delta\varphi}{\partial \tau}. \quad (195)$$

Substituting into Eq.(66) gives at linear order

$$a^3 \sqrt{\bar{\mathcal{X}}} \left[ \frac{d\bar{\mathcal{X}}}{d\lambda} \frac{d^2 \bar{\lambda}}{d\bar{\mathcal{X}}^2} + 4\alpha \frac{d\bar{\lambda}}{d\bar{\mathcal{X}}} \right] \delta\mathcal{X} = \text{constant}, \quad (196)$$

where we used  $\bar{A} \simeq 1$ .

Let us first consider the evolution of  $\delta\mathcal{X}$  at high redshift, in the high-density regime  $\bar{\rho} \gg \rho_\alpha$  and  $z \gg z_\alpha$ . From Eq.(190) we obtain

$$|\bar{\mathcal{X}} - \mathcal{X}_+| \sim \bar{\rho}^{-1/(\mu_+ - 1)} \sim (a/a_\alpha)^{3/(\mu_+ - 1)}, \quad (197)$$

which grows with time but remains small in the high-density regime. Then, Eq.(196) yields

$$\delta\mathcal{X} \propto \frac{|\bar{\mathcal{X}} - \mathcal{X}_+|}{a^3 \sqrt{\bar{\mathcal{X}}}}. \quad (198)$$

If  $\mathcal{X}_+ \neq 0$  we have  $\sqrt{\bar{\mathcal{X}}} \simeq \sqrt{\mathcal{X}_+}$ , whereas if  $\mathcal{X}_+ = 0$  the factor  $\sqrt{\bar{\mathcal{X}}}$  grows with time. Thus,  $\delta\mathcal{X}$  becomes increasingly small as compared with  $|\bar{\mathcal{X}} - \mathcal{X}_+|$  as time grows. Therefore, in the high-density era,  $\bar{\rho} \gg \rho_\alpha$ , the perturbation to the solution (71) decays and that solution is stable.

At low redshift, in the low-density regime  $\bar{\rho} \ll \rho_\alpha$  and  $z \ll z_\alpha$ , we obtain from Eq.(193)

$$|\bar{\mathcal{X}} - \mathcal{X}_-| \sim \bar{\rho}^{1/(1 - \mu_-)} \sim (a/a_\alpha)^{-3/(1 - \mu_-)}, \quad (199)$$

which is small and decreases with time. Then, Eq.(196) yields

$$\delta\mathcal{X} \propto \frac{|\bar{\mathcal{X}} - \mathcal{X}_-|}{a^3 \sqrt{\bar{\mathcal{X}}}}. \quad (200)$$

If  $\mathcal{X}_- \neq 0$  we have  $\sqrt{\bar{\mathcal{X}}} \simeq \sqrt{\mathcal{X}_-}$ , and  $\delta\mathcal{X}$  becomes increasingly small as compared with  $|\bar{\mathcal{X}} - \mathcal{X}_-|$  as time grows. If  $\mathcal{X}_- = 0$ , which can only happen for the concave models, the perturbation only becomes negligible if  $a^3 \sqrt{\bar{\mathcal{X}}}$  grows with time. Using Eq.(199) this gives the condition

$$\text{concave models with } \mathcal{X}_- = 0: \quad \mu_- < \frac{1}{2}. \quad (201)$$

Thus, we find that the solution (71) of the scalar-field equation of motion (66) is stable at high redshift,  $z > z_\alpha$ . At low redshift,  $z < z_\alpha$ , it is stable if the low-density limit of  $\tilde{\chi}(\rho)$  is  $\tilde{\chi}_- > 0$ , or if the exponent  $\mu_- < 1/2$ . In practice, because the low-redshift era has a finite span

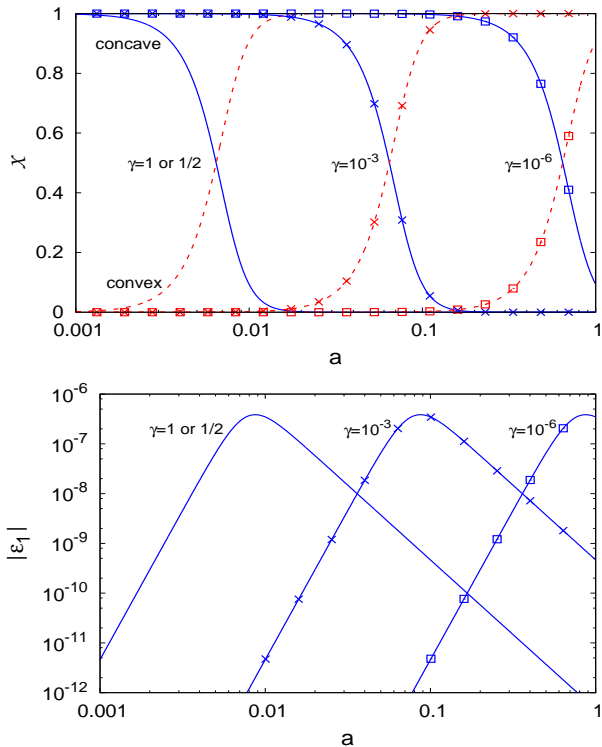


FIG. 2: *Upper panel:* normalized background scalar-field kinetic term  $\chi$  as a function of the scale factor for the concave (solid lines) and convex (dashed lines) models (168) and (184). We show the results for  $\gamma = 1, 10^{-3}, 10^{-6}$  for the concave models, and  $\gamma = 1/2, 10^{-3}, 10^{-6}$  for the convex models. *Lower panel:* amplitude  $|\epsilon_1(a)|$  of the fifth-force factor that enters the evolution of the linear growing mode, for the models shown in the upper panel. The concave and convex models have opposite signs but the same amplitude (exactly for  $\gamma = \{1, 1/2\}$  and approximately for  $\gamma = 10^{-3}$  and  $\gamma = 10^{-6}$ ).

until today, and the perturbation has had time to become negligible during the high-redshift era, we can slightly relax the condition (201). In particular, we can keep the marginal case  $\mu_- = 1/2$  in the model (158), which corresponds to a perturbation that remains small and constant in relative terms in the low-redshift era. In all these cases, the solution (71) is physical.

## IX. LINEAR PERTURBATIONS

### A. Cosmological background

As  $A(\tilde{\chi})$  remains very close to unity, and the factor  $\epsilon_2$  is very small, see Eqs.(106) and (123), the Einstein and Jordan frames are very close and the Jordan-frame Planck mass in Eq.(96) is constant within an accuracy of  $10^{-6}$ . The scalar-field energy density and pressure are almost constant in the dark energy era, evolving more slowly than the Hubble rate by a factor  $|\epsilon_2| \lesssim 10^{-6}$  from

Eq.(102), while they are subdominant at high redshift (they are actually bounded for the models introduced in section VII B whereas the matter and radiation densities keep increasing with redshift). Therefore, we recover the  $\Lambda$ -CDM background cosmology within an accuracy of  $10^{-6}$ .

For the numerical computations presented in this paper we take  $\alpha = 10^{-6}$ ,  $\gamma = \{1, 10^{-3}, 10^{-6}\}$  for the concave model (168), and  $\gamma = \{1/2, 10^{-3}, 10^{-6}\}$  for the convex model (184). We choose  $\gamma = 1/2$  instead of 1 for the convex model because of the condition (179).

We display in the upper panel in Fig. 2 the normalized background kinetic term  $\tilde{\chi}$ . We can check that it shows a transition at the scale factor  $a_\alpha = (\alpha/\gamma)^{1/3}$  between the high-density and low-density regimes. For  $\gamma \gg \alpha$ ,  $z_\alpha \gg 1$  and both  $\tilde{\chi}$  and  $\tilde{\rho}_{\text{de}}$  are very close to a constant at low  $z$ . For  $\gamma = \alpha = 10^{-6}$ , the transition occurs at  $z \sim 1$ , but the dark energy density still remains close to a constant because  $\tilde{\rho}_{\text{de}} \simeq \mathcal{M}^4(1 - \tilde{\chi})$  and  $0 \leq \tilde{\chi} \leq \gamma \ll 1$ . Therefore, in all cases we recover the  $\Lambda$ -CDM background cosmology.

We display in the lower panel in Fig. 2 the factor  $\epsilon_1(a)$  of Eq.(118) [hence  $\epsilon_2(a)$  also as  $\epsilon_2 = 3\epsilon_1$ ]. It remains very small, with a peak of order  $10^{-6}$  at  $a_\alpha$ , in agreement with Eqs.(165)-(167) and (181)-(183). This again means that  $\tilde{A}$  remains very close to unity, from the definition (92).

The curves  $|\epsilon_1(a)|$  are the same for the concave and convex models used in our numerical computations. Indeed, in terms of the rescaled density  $\hat{\rho}$ , the functions  $\epsilon_1(\hat{\rho})$  of Eqs.(171) and (187) happen to have exactly the same amplitude, and opposite signs. Then, comparing Eqs.(162) and (178), we find that  $\gamma_{\text{concave}} = 1$  and  $\gamma_{\text{convex}} = 1/2$  give the same normalized density  $\hat{\rho}$  for a given physical density  $\rho$ . For  $\gamma = 10^{-3}$  and  $\gamma = 10^{-6}$ , we obtain approximately the same value  $\hat{\rho}$ , within an accuracy of  $10^{-3}$  or  $10^{-6}$ , as  $\gamma \ll 1$ . This means that, for a given matter background, whether the cosmological background or the density profile of virialized halos, the three pairs of concave and convex models computed in this paper have the same amplitude for the fifth force but opposite signs.

### B. Concave models

We first consider the case of concave coupling functions, introduced in section VII B 1. This leads to a negative  $\epsilon_1$  and the fifth force decreases the Newtonian gravity. The linear modes  $D_\pm(k, a)$  of the matter density contrast obey the evolution equation (119), where the departure from the  $\Lambda$ -CDM cosmology only comes from the factor  $\epsilon(k, a)$ . Because  $|\epsilon_1| \lesssim \alpha \ll 1$ , the factor 1 in Eq.(120) gives a negligible contribution to  $(1 + \epsilon)$  and we can write

$$\epsilon(k, a) = \epsilon_1(a) \frac{2}{3\Omega_m} \left( \frac{ck}{aH} \right)^2. \quad (202)$$

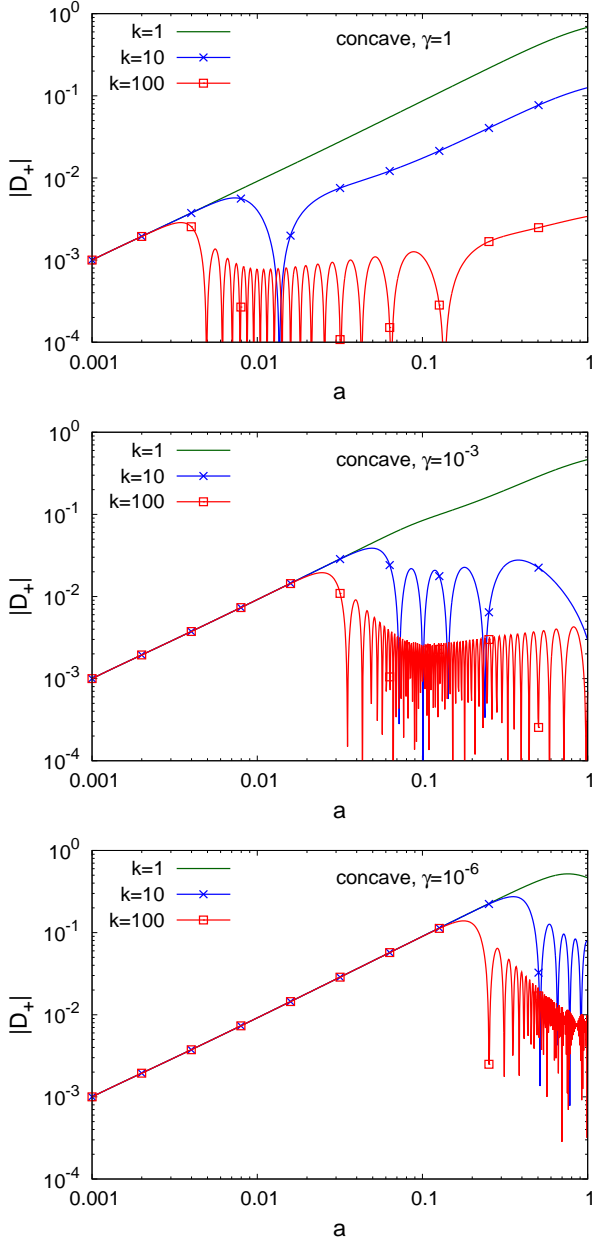


FIG. 3: Linear growing mode  $D_+(k, a)$  as a function of the scale factor for  $k = 1, 10$  and  $100 h\text{Mpc}^{-1}$ , from top to bottom. The different panels are the concave models with  $\gamma = 1, 10^{-3}$ , and  $10^{-6}$ , from top to bottom.

On Hubble scales we have  $\epsilon \sim \epsilon_1$ , hence  $|\epsilon| \lesssim \alpha \ll 1$  and we recover the  $\Lambda$ -CDM growth of structures. On smaller scales  $|\epsilon(k, a)|$  grows as  $k^2$  and it reaches unity at a wavenumber

$$k_\alpha(a) \simeq \frac{aH}{c\sqrt{|\epsilon_1|}} \simeq \frac{3 \times 10^{-4}}{\sqrt{a|\epsilon_1|}} h\text{Mpc}^{-1}, \quad (203)$$

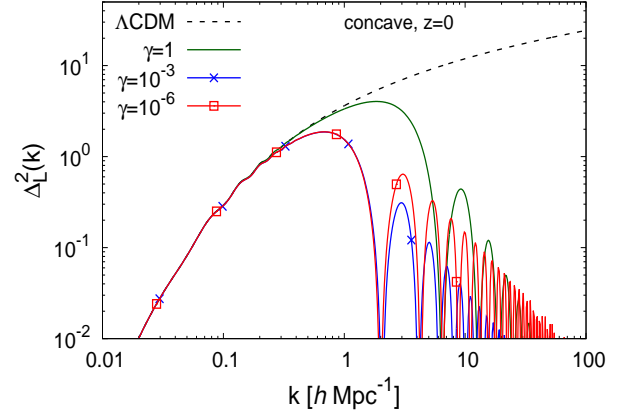


FIG. 4: Logarithmic linear power spectrum  $\Delta_L^2(k, a) = 4\pi k^3 P_L(k, a)$  for the concave models at redshift  $z = 0$ .

where we used  $H^2 \propto a^{-3}$  in the matter era. From Eqs.(165)-(166) we have

$$a \ll a_\alpha : k_\alpha(a) \simeq \frac{H_0}{c} \alpha^{-2/3} \gamma^{1/6} \left( \frac{a}{a_\alpha} \right)^{-(4\mu_+ - 1)/[2(\mu_+ - 1)]}, \quad (204)$$

$$a \gg a_\alpha : k_\alpha(a) \simeq \frac{H_0}{c} \alpha^{-2/3} \gamma^{1/6} \left( \frac{a}{a_\alpha} \right)^{(4\mu_- - 1)/[2(1 - \mu_-)]}. \quad (205)$$

Thus,  $k_\alpha(a)$  decreases with time in the high-redshift era  $a < a_\alpha$ , which means that increasingly large comoving scales enter the regime where the fifth force dominates over Newtonian gravity and stops the growth of matter perturbations. In the low-redshift era,  $a > a_\alpha$ ,  $k_\alpha(a)$  increases with time if  $\mu_- > 1/4$  and decreases if  $\mu_- < 1/4$ . Thus, we find that the minimum value of  $k_\alpha$  until today is given by

$$\mu_- > \frac{1}{4} : k_\alpha^{\min} = k_\alpha(a_\alpha) = \frac{H_0}{c} \alpha^{-2/3} \gamma^{1/6}, \quad (206)$$

$$\mu_- < \frac{1}{4} : k_\alpha^{\min} = k_\alpha(1) = \frac{H_0}{c} \alpha^{-1/[2(1 - \mu_-)]} \gamma^{\mu_-/[2(1 - \mu_-)]}. \quad (207)$$

Wavenumbers below  $k_\alpha^{\min}$ , i.e. comoving scales greater than  $1/k_\alpha^{\min}$ , have never entered the fifth-force regime yet. Higher wavenumbers have entered the fifth-force regime at the scale factor  $a_-(k)$  given by

$$a_-(k) = \alpha^{1/(4\mu_+ - 1)} \gamma^{-\mu_+/(4\mu_+ - 1)} \left( \frac{ck}{H_0} \right)^{-2(\mu_+ - 1)/(4\mu_+ - 1)}, \quad (208)$$

if  $\mu_- > 1/4$  or  $k > k_\alpha(a_\alpha)$ , and by

$$a_-(k) = \alpha^{-1/(1 - 4\mu_-)} \gamma^{\mu_-/(1 - 4\mu_-)} \left( \frac{ck}{H_0} \right)^{-2(1 - \mu_-)/(1 - 4\mu_-)}, \quad (209)$$

if  $\mu_- < 1/4$  and  $k_\alpha(1) < k < k_\alpha(a_\alpha)$ . If  $\mu_- > 1/4$  they have left the fifth-force regime at the scale factor  $a_+(k)$  given by (if  $a_+ < 1$ )

$$\mu_- > \frac{1}{4} : a_+(k) = \alpha^{1/(4\mu_- - 1)} \gamma^{-\mu_-/(4\mu_- - 1)} \times \left( \frac{ck}{H_0} \right)^{2(1-\mu_-)/(4\mu_- - 1)}, \quad (210)$$

while if  $\mu_- < 1/4$  they have never left the fifth-force regime yet,  $a_+(k) > 1$ . In the time interval  $[a_-, a_+]$ , the factor  $(1 + \epsilon)$  in the linear evolution equation (119) is dominated by  $\epsilon$  and becomes negative. This means that the density fluctuations no longer feel an attractive gravity but a pressure-like force. Then, the linear growing mode  $D_+(k, a)$  stops growing and develops an oscillatory behavior. As the fifth-force regime starts earlier and ends later for higher wavenumbers,  $D_+(k, a)$  is more strongly suppressed for higher wavenumbers as compared with the  $\Lambda$ -CDM growing mode. At low wavenumbers,  $k < k_\alpha^{\min}$ , the fifth force was never relevant and we recover the  $\Lambda$ -CDM prediction. We refer to [14] for a more detailed analysis, for the case  $\gamma = 1$ .

This agrees with the results shown in Fig. 3. For  $k \ll 10h\text{Mpc}^{-1}$  we recover the  $\Lambda$ -CDM steady growth of matter perturbations, while for  $k \gg 10h\text{Mpc}^{-1}$  we have an oscillatory phase around  $a_\alpha$ . For smaller  $\gamma$  the transition scale factor  $a_\alpha$  increases and the oscillatory phase occurs at lower redshifts.

These behaviors lead to a sharp falloff in the logarithmic linear power spectrum  $\Delta_L(k)$  at high  $k$ , shown in Fig. 4. The dependence of the power spectrum at  $z = 0$  on  $\gamma$  is not simple, because of the interplay between the mean redshift and the duration of the oscillatory phase. We find that  $\gamma = 10^{-3}$  and  $10^{-6}$  give similar cutoffs, which appear at somewhat larger scales than for  $\gamma = 1$ . The larger-scale cutoff for  $\gamma = 10^{-3}$  as compared with  $\gamma = 1$  agrees with Eq.(206). The cutoff does not decrease further for  $\gamma = 10^{-6}$  because the fifth-force factor  $|\epsilon_1|$  has just peaked and the Hubble rate in Eq.(203) is somewhat higher in the dark-energy era than predicted by the matter-era scaling that we used here.

### C. Convex models

We now consider the case of convex coupling functions, introduced in section VII B 2. This leads to a positive  $\epsilon_1$  and the fifth force increases the Newtonian gravity. We can again use the approximation (202) for  $\epsilon(k, a)$ , define the transition wavenumber  $k_\alpha(a)$  to the fifth-force regime as in Eq.(203), with the asymptotic behaviors (204)-(205), and the minimum values (206)-(207). For a given comoving wavenumber  $k$ , the fifth-force regime extends over the time range  $[a_-, a_+]$  given by Eqs.(208)-(210).

In the time interval  $[a_-, a_+]$ , the factor  $(1 + \epsilon)$  in the linear evolution equation (119) is dominated by  $\epsilon$  and

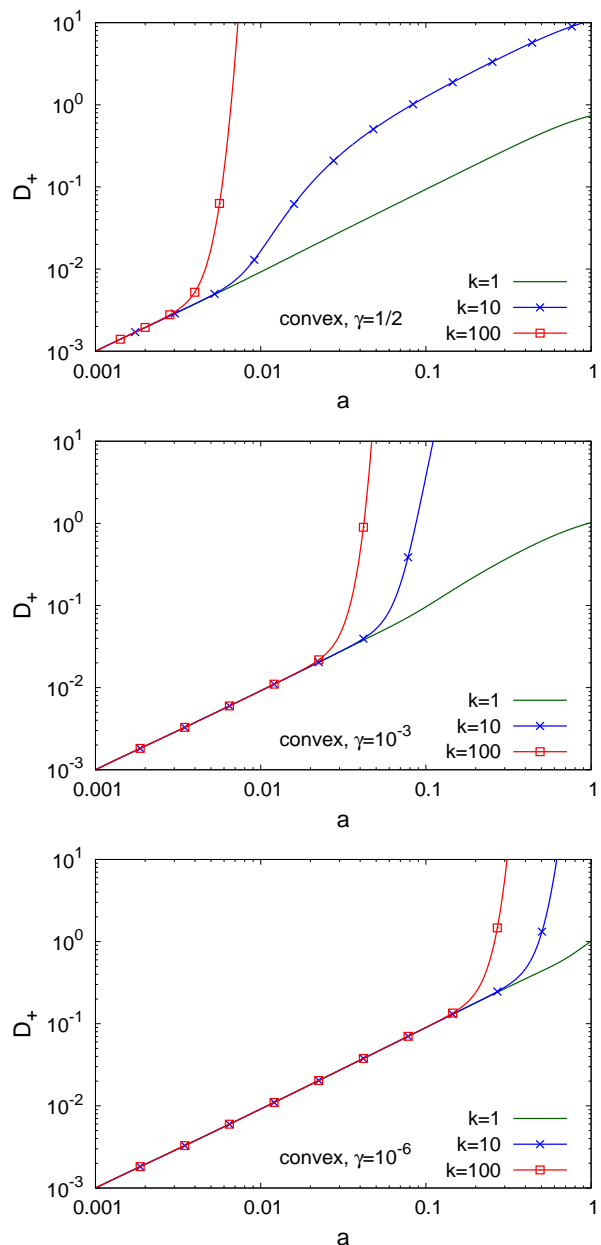


FIG. 5: Linear growing mode  $D_+(k, a)$  as a function of the scale factor for  $k = 1, 10$  and  $100h\text{Mpc}^{-1}$ , from bottom to top. The different panels are the convex models with  $\gamma = 1/2, 10^{-3}$ , and  $10^{-6}$ , from top to bottom.

becomes large and positive. This means that the linear growing mode  $D_+(k, a)$  grows much faster than in the  $\Lambda$ -CDM scenario, and increasingly so for higher  $k$  because of the  $k^2$  dependence of  $\epsilon(k, a)$  in Eq.(202). Moreover, this fifth-force regime starts earlier and ends later for higher wavenumbers. Therefore,  $D_+(k, a)$  is more strongly amplified for higher wavenumbers. At low wavenumbers,  $k < k_\alpha^{\min}$ , the fifth force was never relevant and we again recover the  $\Lambda$ -CDM prediction. We refer to [14] for a more detailed analysis, for the case  $\gamma = 1$ .

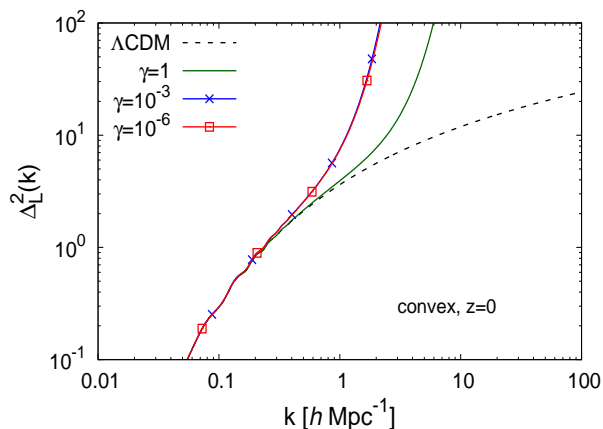


FIG. 6: Logarithmic linear power spectrum  $\Delta_L^2(k, a) = 4\pi k^3 P_L(k, a)$  for the convex models at redshift  $z = 0$ .

This agrees with the results shown in Fig. 5. For  $k \ll 10h\text{Mpc}^{-1}$  we recover the slow  $\Lambda$ -CDM growth of matter perturbations, while for  $k \gg 10h\text{Mpc}^{-1}$  we have a very fast amplification phase around  $a_\alpha$ . This leads to a sharp increase in the logarithmic linear power spectrum  $\Delta_L(k)$  at high  $k$ , shown in Fig. 6. In a fashion similar to the concave case,  $\gamma = 10^{-3}$  and  $10^{-6}$  give similar departures from the  $\Lambda$ -CDM power, with now a strong amplification that appears at somewhat larger scales than for  $\gamma = 1$ .

## X. SPHERICAL COLLAPSE

### A. Equation of motion

As can be seen from Eq.(110), on large scales where the baryonic pressure is negligible the particle trajectories  $\mathbf{r}(t)$  are given by

$$\frac{d^2\mathbf{r}}{dt^2} - \frac{1}{a} \frac{d^2a}{dt^2} \mathbf{r} = -\nabla_{\mathbf{r}} (\Psi_N + \Psi_A), \quad (211)$$

where  $\mathbf{r} = a\mathbf{x}$  is the physical coordinate,  $\nabla_{\mathbf{r}} = \nabla/a$  the gradient operator in physical coordinates, and  $\Psi_A = c^2 \ln A$  is the fifth force contribution to the metric potential  $\Phi$  in Eq.(108). As in [14], to study the spherical collapse before shell crossing it is convenient to label each shell by its Lagrangian radius  $q$  or enclosed mass  $M$ , and to introduce its normalized radius  $y(t)$  by

$$y(t) = \frac{r(t)}{a(t)q} \quad \text{with} \quad q = \left( \frac{3M}{4\pi\bar{\rho}_0} \right)^{1/3}, \quad y(t=0) = 1. \quad (212)$$

In particular, the matter density contrast within radius  $r(t)$  reads as  $1 + \delta_{<}(r) = y(t)^{-3}$ . Then, the equation of

motion of the normalized radius  $y$  reads as [14]

$$\frac{d^2y}{d(\ln a)^2} + \left( 2 + \frac{1}{H^2} \frac{dH}{dt} \right) \frac{dy}{d \ln a} + \frac{\Omega_m}{2} y(y^{-3} - 1) = -y \left( \frac{c}{Hr} \right)^2 \frac{d \ln A}{d \ln \rho} \frac{r}{1 + \delta} \frac{\partial \delta}{\partial r}. \quad (213)$$

In contrast with the  $\Lambda$ -CDM case, where the dynamics of different shells are decoupled before shell crossing, the fifth force introduces a coupling as it depends on the density profile, through the local density contrast  $\delta(r)$  and its first derivative  $\partial\delta/\partial r$ . As in [14], to bypass this difficulty we decouple the motion of the shell of mass  $M$  of interest by assuming a constant shape for the density profile, which is then fully parameterized by the density contrast  $\delta_{<}$  within the mass shell  $M$  [more precisely, we choose the typical profile associated with a Gaussian field of power spectrum  $P_L(k)$ ].

### B. Concave models

We show in Fig. 7 the evolution of the matter density contrast  $\delta_{<}$  within a spherical shell  $M$ , given by the spherical collapse dynamics. We consider several mass scales  $M$ . All curves follow the same behavior at very high redshift, before the fifth-force becomes important, as we choose the same initial conditions, which corresponds to a linear density contrast today of  $\delta_{<L}^{\Lambda\text{-CDM}} = 1.6$  in the  $\Lambda$ -CDM cosmology. In agreement with the results found in section IX B, large masses, associated with large scales, follow the  $\Lambda$ -CDM behavior, whereas small masses show an oscillatory phase around  $a_\alpha$ . This significantly delays the collapse of small scales. Moreover, because of the change of signs due to the oscillations, an initial overdensity may turn underdense at the end of the oscillatory phase, which means that it will never collapse after the fifth force becomes negligible (within the spherical no-shell-crossing approximation). We refer to [14] for a more detailed analysis of the case  $\gamma = 1$ , where we also study the spherical dynamics for different values of the initial density contrast.

We show in Fig. 8 the linear density contrast threshold, measured by  $\delta_{<L}^{\Lambda\text{-CDM}}$  (i.e., the extrapolation up to  $z = 0$  of the initial density contrast by the  $\Lambda$ -CDM growth rate), required to reach a nonlinear density contrast  $\delta_{<} = 200$  today. Again, at large mass we recover the  $\Lambda$ -CDM linear density threshold,  $\delta_{<L}^{\Lambda\text{-CDM}} \simeq 1.6$ , whereas at small mass we obtain a much greater linear density threshold  $\delta_{<L}^{\Lambda\text{-CDM}} \sim 100$ . This is required to compensate the slower growth at low mass found in Fig. 7.

For  $\gamma = 1$  we find a non-monotonic curve, which is due to the oscillation phase and the complex behavior found in Fig. 7. Indeed, as explained above, some overdensities become underdensities at the end of the oscillation phase and never collapse. This implies that such initial conditions cannot contribute to the curve  $\delta_{<L}^{\Lambda\text{-CDM}}$  of the linear density threshold, and that only initial conditions

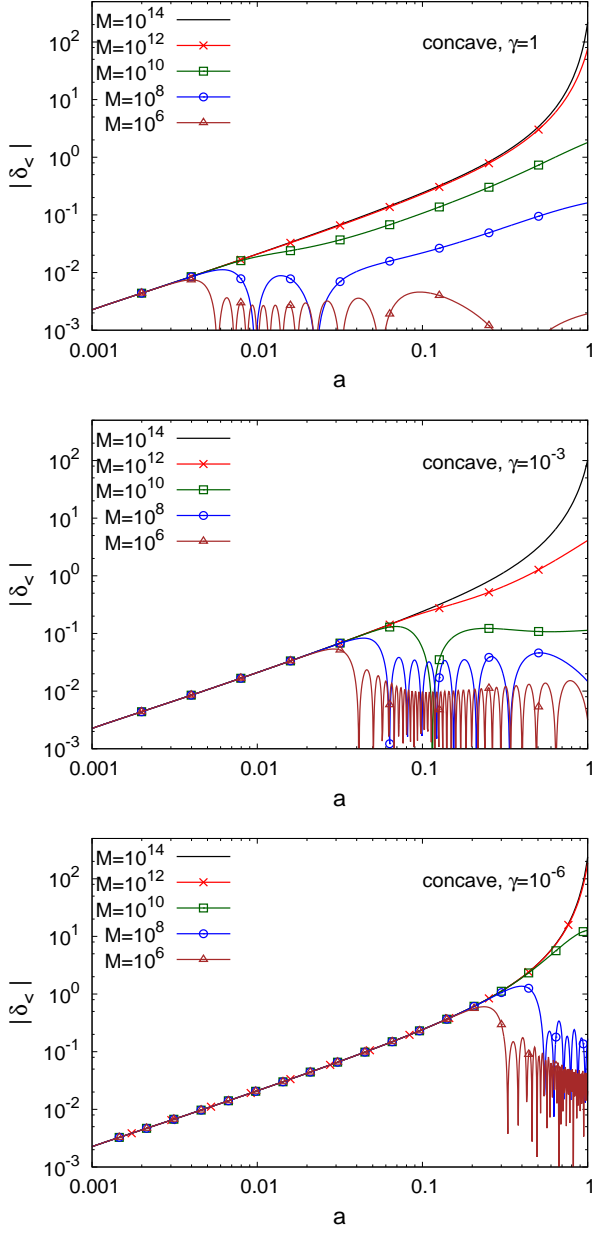


FIG. 7: Evolution with time of the nonlinear density contrast  $\delta_{<}(a)$  for several masses, from  $M = 10^{14}$  to  $10^6 h^{-1} M_{\odot}$  from top to bottom, with the same initial condition that corresponds to the  $\Lambda$ -CDM linear density threshold today  $\delta_{<L}^{\Lambda\text{-CDM}} = 1.6$ . The different panels are the concave models with  $\gamma = 1, 10^{-3}$ , and  $10^{-6}$ , from top to bottom.

associated with an even number of oscillations are relevant. These jumps from one even number to the next, skipping the odd number in-between, lead to the jumps found for  $\gamma = 1$ , see also the discussion in Ref. [14]. For  $\gamma = 10^{-3}$  and  $10^{-6}$  these jumps or steps are beyond the mass range shown in the figure.

In any case, the formation of low mass halos is strongly suppressed as compared with the  $\Lambda$ -CDM scenario. In

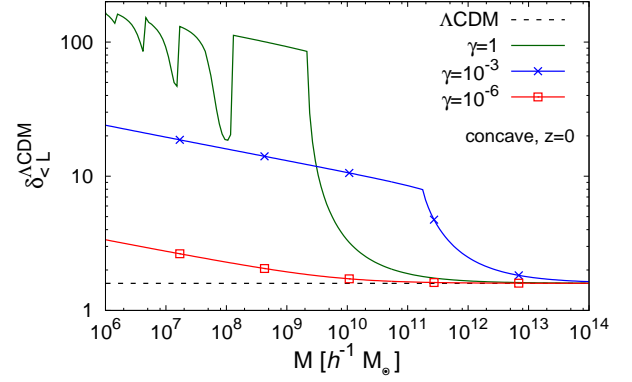


FIG. 8: Initial linear density contrast, as measured by  $\delta_{<L}^{\Lambda\text{-CDM}}$ , that gives rise to a nonlinear density contrast  $\delta_{<} = 200$  at  $z = 0$ , as a function of the halo mass  $M$ .

fact, rather than forming in the usual bottom-up hierarchical fashion of CDM models, low-mass halos may form later in a top-down fashion, by fragmentation of larger-mass halos, as in Warm Dark Matter (WDM) scenarios. For  $\gamma = 10^{-6}$  the oscillatory phase only takes place at low redshift. Then, for relevant cosmological masses,  $M \gtrsim 10^6 h^{-1} M_{\odot}$ , the threshold  $\delta_{<L}^{\Lambda\text{-CDM}}$  is not so much higher than in the  $\Lambda$ -CDM cosmology, as it is sufficient that the collapse was already sufficiently advanced at  $z \sim 1$ . As compared with the linear power spectrum shown in Fig. 4, where the cases  $\gamma = 10^{-3}$  and  $10^{-6}$  gave similar results, they now give very different results for  $\delta_{<L}^{\Lambda\text{-CDM}}$ . Moreover, at  $M \gtrsim 10^{10} h^{-1} M_{\odot}$ , the curve obtained for  $\gamma = 1$  falls in between the results obtained for  $\gamma = 10^{-3}$  and  $\gamma = 10^{-6}$ . This is due to the complex behavior of the fifth force, associated with these oscillatory phases and their different redshifts, that lead to different orderings between the models depending on the measured quantity.

### C. Convex models

We show in Fig. 9 the evolution of the matter density contrast  $\delta_{<}$  given by the spherical collapse dynamics for the convex models, as was done in Fig. 7 for the concave models. In agreement with the results found in section IX C, large masses again follow the  $\Lambda$ -CDM behavior, whereas small masses show a very fast amplification phase around  $a_{\alpha}$ . This significantly accelerates the collapse of small scales.

The initial condition, measured by the linear density contrast threshold  $\delta_{<L}^{\Lambda\text{-CDM}}$ , required to reach a nonlinear density contrast  $\delta_{<} = 200$  today, is shown in Fig. 10.

At large mass we recover the  $\Lambda$ -CDM linear density threshold, whereas at small mass we obtain a much smaller linear density threshold. This is required to compensate the faster growth found at low mass in Fig. 9.

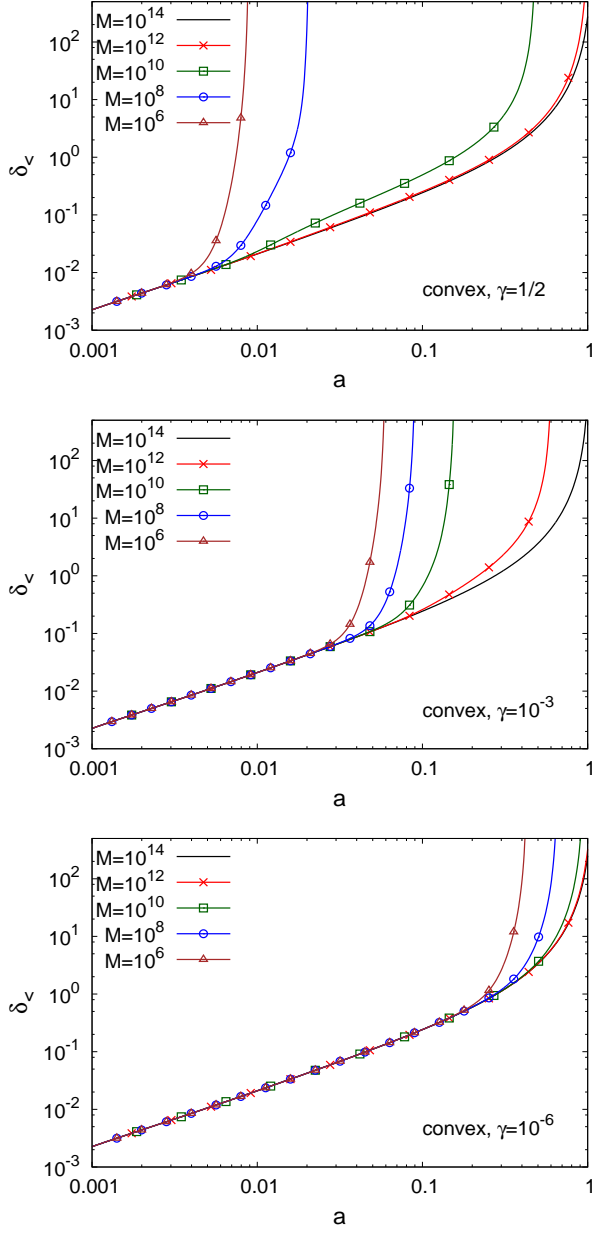


FIG. 9: Evolution with time of the nonlinear density contrast  $\delta_v(a)$  for several masses, from  $M = 10^{14}$  to  $10^6 h^{-1} M_\odot$  from bottom to top, with the same initial condition that corresponds to the  $\Lambda$ -CM linear density threshold today  $\delta_{<L}^{\Lambda\text{-CDM}} = 1.6$ . The different panels are the convex models with  $\gamma = 1/2, 10^{-3}$ , and  $10^{-6}$ , from top to bottom.

Again, the dependence on  $\gamma$  is not simple and for  $M \gtrsim 10^{10} h^{-1} M_\odot$ , the curve obtained for  $\gamma = 1$  falls in between the results obtained for  $\gamma = 10^{-3}$  and  $\gamma = 10^{-6}$ . As compared with the linear power spectrum shown in Fig. 6, where the cases  $\gamma = 10^{-3}$  and  $10^{-6}$  gave similar results, this again shows that different measured quantities can lead to a different ordering between the models.

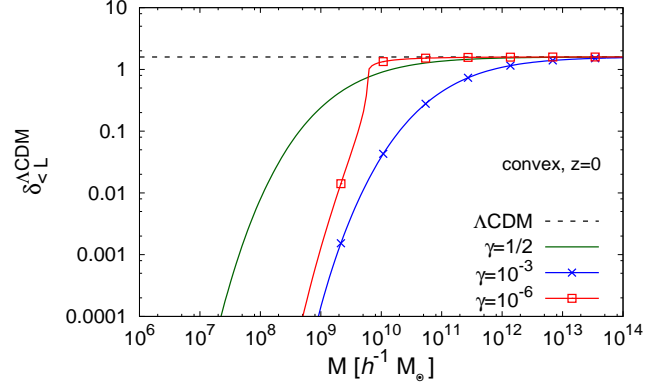


FIG. 10: Initial linear density contrast, as measured by  $\delta_{<L}^{\Lambda\text{-CDM}}$ , that gives rise to a nonlinear density contrast  $\delta_{<} = 200$  at  $z = 0$ , as a function of the halo mass  $M$ .

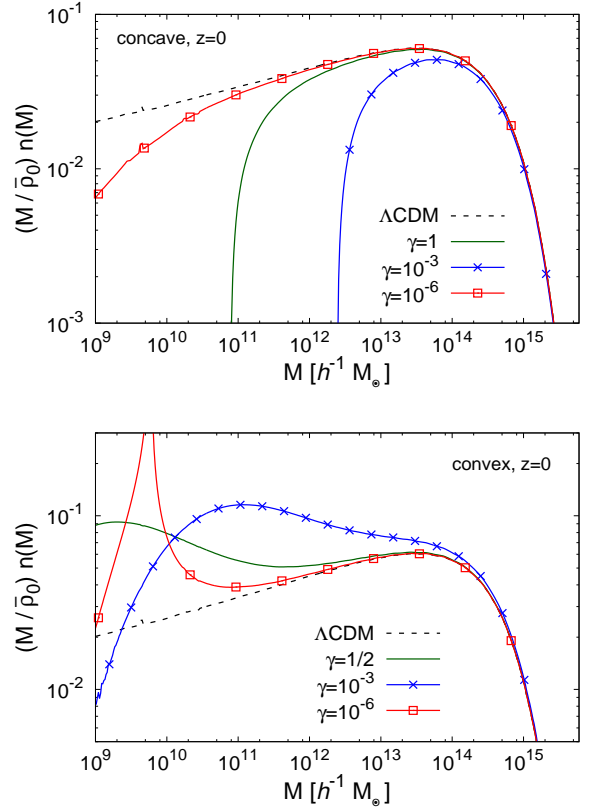


FIG. 11: Halo mass function at  $z = 0$  for the concave and convex models, and for the  $\Lambda$ -CDM reference.

## D. Halo mass function

Following a Press-Schechter approach [30], we write the comoving halo mass function as

$$n(M) \frac{dM}{M} = \frac{\bar{\rho}_0}{M} f(\nu) \frac{d\nu}{\nu}, \quad (214)$$

where the scaling variable  $\nu(M)$  is defined as

$$\nu(M) = \frac{\delta_{<L}^{\Lambda\text{CDM}}(M)}{\sigma(M)}, \quad (215)$$

and  $\delta_{<L}^{\Lambda\text{CDM}}(M)$  is again the initial linear density contrast (extrapolated up to  $z = 0$  by the  $\Lambda$ -CDM linear growth factor) that is required to build a collapsed halo (which we define here by a nonlinear density contrast of 200 with respect to the mean density of the Universe). The variable  $\nu$  measures whether such an initial condition corresponds to a rare and very high overdensity in the initial Gaussian field ( $\nu \gg 1$ ) or to a typical fluctuation ( $\nu \lesssim 1$ ). In the Press-Schechter approach, we have  $f(\nu) = \sqrt{2/\pi} \nu e^{-\nu^2/2}$  [30]. Here we use the same function as in [31]. Then, the impact of the modified gravity only arises through the linear threshold  $\delta_{<L}^{\Lambda\text{CDM}}(M)$ , as we assume the same initial matter density power spectrum as for the  $\Lambda$ -CDM reference at high redshift.

We display the halo mass function in Fig. 11. For both concave and convex models we recover the  $\Lambda$ -CDM large-mass tail, in agreement with the convergence to the  $\Lambda$ -CDM threshold in Figs. 8 and 10. At low mass, the halo mass function is smaller/greater for the concave/convex models than the  $\Lambda$ -CDM reference, in agreement with the higher/lower thresholds in Figs. 8 and 10.

For the concave model, the mass function defined by Eq.(214) actually becomes negative below  $10^{11} h^{-1} M_\odot$  for  $\gamma = 1$ , and at a higher or lower mass for  $\gamma = 10^{-3}$  and  $10^{-6}$ . This is due to the fast increase of  $\delta_{<L}^{\Lambda\text{CDM}}(M)$  at low mass, which makes  $\nu$  increase at lower mass (in this range), instead of decreasing, and gives a change of sign for  $d\nu/dM$ . Of course, this means that the prediction (214) is not physical at low mass. This is because at low mass structure formation no longer follows the standard hierarchical picture. Because of the damping of density perturbations on small scales, found in Figs. 3 and 7, small scales do not collapse first. Then, smaller-mass objects would form (if they do) in a top-down scenario, where larger masses,  $\gtrsim 10^{11} h^{-1} M_\odot$ , collapse first and next fragment into smaller substructures, as in a hot dark matter scenario. In contrast, for the convex model the hierarchical pattern of structure formation is even stronger than in the  $\Lambda$ -CDM cosmology, because the growth of matter perturbations is increasingly fast on smaller scales. The spike at  $5 \times 10^9 h^{-1} M_\odot$  for the convex model with  $\gamma = 10^{-6}$  is due to the sudden change of  $\delta_{<L}^{\Lambda\text{CDM}}(M)$  at this mass scale found in Fig. 10. In practice, we do not expect the Press-Schechter picture, based on the spherical collapse, to provide a reliable prediction of such sharp features, and this peak is probably

smoothened by perturbations from the spherical collapse and mergers. However, we can expect a greater abundance of halos around this mass scale than for the  $\Lambda$ -CDM cosmology.

## XI. NEWTONIAN AND FIFTH-FORCE REGIMES

### A. Clusters and galaxies

We study in this section how the fifth force compares to Newtonian gravity on the scales of large cosmological structures such as galaxies and clusters. As in [14], we can associate to the Newtonian force the circular velocity  $v_N^2$  at radius  $r$ ,

$$F_N = -\frac{v_N^2(r)}{r}, \quad v_N^2 = \frac{\mathcal{G}_N M(<r)}{r}, \quad (216)$$

and to the fifth force a characteristic velocity  $c_s^2$  with

$$F_A = \pm \frac{c_s^2}{r}, \quad c_s^2 = c^2 \left| \frac{d \ln A}{d \ln \rho} \frac{d \ln \rho}{d \ln r} \right|, \quad (217)$$

so that the force ratio  $\eta$  reads as

$$|\eta| = \left| \frac{F_A}{F_N} \right| = \frac{c_s^2}{v_N^2}. \quad (218)$$

To keep the ratio  $\eta$  below unity in typical astrophysical and cosmological structures, we need  $c_s^2 \lesssim v_N^2 \lesssim 10^{-6} c^2$ . This implies again that the coupling function in Eq.(217) must be small,  $|\delta \ln A| \lesssim 10^{-6}$ , and we recover the constraint (106).

Let us now consider typical cosmological structures, such as clusters and galaxies, in the low-redshift Universe at  $z \simeq 0$ . In the low-density regime, we have from Eq.(193)

$$\rho \ll \rho_\alpha : \quad c_s^2 \sim c^2 \alpha \hat{\rho}^{\mu_- / (1-\mu_-)}, \quad (219)$$

and

$$z \simeq 0 : \quad v_N^2 \sim (H_0 R)^2 \gamma \hat{\rho} / \alpha, \quad (220)$$

for objects of rescaled density  $\hat{\rho}$  and radius  $R$ . This gives

$$\eta \sim \left( \frac{\alpha c}{\sqrt{\gamma} H_0 R} \right)^2 \hat{\rho}^{-(1-2\mu_-)/(1-\mu_-)}. \quad (221)$$

For the particular case  $\mu_- = 1/2$  this yields

$$\mu_- = \frac{1}{2} : \quad \eta \sim \frac{1}{\gamma} \left( \frac{\alpha}{10^{-6}} \right)^2 \left( \frac{3h^{-1} \text{kpc}}{R} \right)^2. \quad (222)$$

Thus, at low  $z$  for  $\alpha = 10^{-6}$  and  $\gamma = 1$  the fifth force is negligible on extragalactic scales, such as cluster sizes ( $1h^{-1} \text{Mpc}$ ) and beyond, while it becomes of order of the Newtonian force on galactic scales, around  $3h^{-1} \text{kpc}$ . For

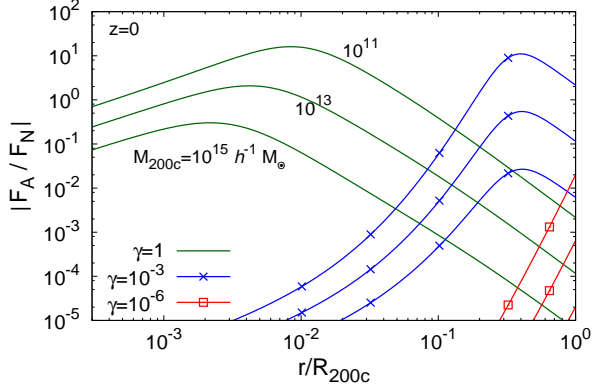


FIG. 12: Absolute value of the ratio  $\eta = F_A/F_N$ , as a function of the radius  $r$ , within spherical halos. We display the halo masses  $M_{200c} = 10^{15}, 10^{13}$  and  $10^{11} h^{-1} M_{\odot}$ , from bottom to top, at  $z = 0$ . The concave and convex models have the same amplitude  $|\eta|$  but opposite signs, for  $\gamma = \{1, 10^{-3}, 10^{-6}\}$  and  $\gamma = \{1/2, 10^{-3}, 10^{-6}\}$ .

$\gamma = 10^{-6}$ , Eq.(222) would suggest that the fifth force would be important on Mpc scales, associated with clusters, but this is not the case because for such a value of  $\gamma$  virialized structures with a density contrast greater than 200 are no longer in the low-density regime (219). We give a more detailed analysis in Fig. 12 below.

The scale dependence  $R^{-2}$ , which amplifies the fifth force on small scales, is related to the  $k^2$  dependence in the factor  $\epsilon(k, a)$  in Eq.(202), which governs the evolution of linear cosmological matter perturbations. This is due to the fact that the fifth-force potential depends on the density,  $\rho \propto \nabla^2 \Psi_N$ , instead of the gravitational potential  $\Psi_N$ .

## B. Spherical halos

Let us now study the behavior of the fifth force inside spherical halos. For simplicity we consider power-law density profiles,

$$\rho(r) \sim \rho_{\alpha} \left( \frac{r}{r_{\alpha}} \right)^{-\gamma_p}. \quad (223)$$

For a Navarro-Frenk-White (NFW) density profile [32], we have  $\gamma_p = 1$  in the inner parts of the halos. In the high-density regime, we have from Eq.(190)

$$\rho \gg \rho_{\alpha} : c_s^2 \sim c^2 \alpha \hat{\rho}^{-\mu_+ / (\mu_+ - 1)}, \quad (224)$$

while  $v_N^2 \propto \rho r^2$ . Then, we find that in the power-law density profile (223) the ratio  $\eta$  behaves as

$$r \ll r_{\alpha} : \eta \propto r^{-2 + \gamma_p (2\mu_+ - 1) / (\mu_+ - 1)}. \quad (225)$$

In particular, the fifth force becomes negligible at the center of the halo if we have

$$\eta \rightarrow 0 \text{ for } r \rightarrow 0 \text{ if } \gamma_p > 1 - \frac{1}{2\mu_+ - 1}. \quad (226)$$

Thus, the fifth force always becomes negligible inside NFW halos, for any exponent  $\mu_+$ . This screening is due to the fact that at high densities the scalar-field kinetic term goes to the constant  $\tilde{\chi}_+$ , for the models introduced in section VII B, which means that the coupling function also goes to the constant  $A_+ = A(\tilde{\chi}_+)$ . Because a constant coupling function does not generate any fifth force (which is proportional to  $\nabla \ln A$ ), this leads to a suppression of the fifth force at high densities. Within a halo with a radial density profile, the efficiency of this damping depends on the growth rate of the density at smaller radii. Thus,  $\eta$  goes faster to zero at small radii in Eq.(225) for a larger slope  $\gamma_p$ .

We show the amplitude of the force ratio  $\eta$  in Fig. 12. As for  $\epsilon_1(a)$  shown in Fig. 2, the concave and convex models with  $\gamma = \{1, 10^{-3}, 10^{-6}\}$  and  $\gamma = \{1/2, 10^{-3}, 10^{-6}\}$  give the same amplitude and opposite signs for  $\eta(r)$  within a given halo. This is because the functions  $d\lambda/d\ln \rho$  of Eqs.(171) and (171) have the same amplitude and opposite signs while the normalized densities  $\hat{\rho}$  are exactly or almost equal.

At large radii, where  $\rho \ll \rho_{\alpha}$ , we have the  $r^{-2}$  relative decrease of the fifth force as in Eq.(222), whereas at small radii, we have the decrease given by Eq.(225). At the transition between the small-radii and large-radii regimes, we have  $\hat{\rho} \simeq 1$  and  $r \simeq r_{\alpha}$ . From Eq.(221) we obtain

$$r_{\alpha} \propto (\gamma/\alpha)^{-1/\gamma_p} \text{ and } \eta(r_{\alpha}) \propto \alpha^{2-2/\gamma_p} \gamma^{2/\gamma_p - 1}, \quad (227)$$

where we assumed that the power-law (223) holds up to the halo radius  $R_{200c}$ . For  $\gamma_p = 2$ , which corresponds to the typical slope at intermediate radii, this yields  $\eta(r_{\alpha}) \propto \alpha$ . This agrees with Fig. 12, where we find that the amplitude of the peak of  $\eta$ , at the transition between the small- and large-radii regimes, does not depend much on  $\gamma$ , while its location  $r_{\alpha}$  grows roughly as  $1/\sqrt{\gamma}$  for smaller  $\gamma$ .

In agreement with the analysis of Eq.(222) above, the fifth force is negligible for massive halos such as clusters of galaxies, but becomes important for smaller galactic halos. In particular, we find that the fifth force becomes significantly greater than the Newtonian gravity at intermediate radii for halos of mass  $\lesssim 10^{11} h^{-1} M_{\odot}$ . This suggests that these models, with  $\gamma \gtrsim 10^{-4}$ , are actually ruled out by observations, which are consistent with Newtonian gravity on galactic scales. This constraint disappears for models with  $\gamma \lesssim 10^{-4}$ , because the peak of  $|\eta|$  at  $r_{\alpha}$  does not exist as it would be pushed outside of the halo in the figure. This is because virialized halos have a large overdensity, of order  $200/\Omega_m$  at the virial radius, so that they entirely fall in the high-density regime of the coupling function  $\ln A$  (and even more so at higher redshift). Then, the peak associated with the transition be-

tween the high-density and low-density regimes is never reached.

For the convex models with  $\gamma \gtrsim 10^{-4}$ , where the fifth force amplifies the formation of structures, this problem may be circumvented by nonlinearities. Indeed, the fifth force could lead to the fragmentation of the system into smaller and denser substructures, where the fifth force would next become negligible because of the screening mechanism described in section XID below, due to the locality of the fifth force. This would not change the spherically-averaged properties of the halo but inhomogeneities would be significant and would invalidate the mean-field analysis used in Eq.(225) and Fig. 12, because of the local and nonlinear character of the fifth force, which is not self-averaging.

For the concave models, this nonlinear process is unlikely to solve the problem found in Fig. 12 at low mass for  $\gamma \gtrsim 10^{-4}$ . Indeed, because the fifth force is now repulsive and acts like a standard polytropic pressure, instead of promoting the fragmentation of the system and the building of inhomogeneous nonlinear structures, it prevents the collapse and tends to smooth density profiles. Therefore, a mean-field analysis, where we neglect substructures, should be a good approximation, and we can expect the problem found in Fig. 12 to be real. A related issue is that the large repulsive fifth force found in Fig. 12 suggests that halos of mass  $\lesssim 10^{11} h^{-1} M_\odot$  and moderate densities cannot form in the first place, as the collapse is stopped by the fifth force. This means that concave models with  $\gamma \gtrsim 10^{-4}$  are probably ruled out by observations.

### C. Fifth-force dominated regime

We now study more generally which regions in the planes  $(\rho, R)$  or  $(M, R)$ , for matter structures of global density  $\rho$ , radius  $R$ , and mass  $M$ , are dominated by the fifth force. Writing  $M = 4\pi\rho R^3/3$ , we obtain from Eq.(218)

$$|\eta| \sim \frac{2}{\Omega_{\text{m}0}} \frac{\bar{\rho}_0}{\rho} \left( \frac{c}{RH_0} \right)^2 \left| \frac{d \ln A}{d \ln \rho} \right|. \quad (228)$$

Then, the fifth force is greater than Newtonian gravity if we have

$$|\eta| \geq 1 : \quad R^2 \leq \left( \frac{c}{H_0} \right)^2 \frac{2}{\Omega_{\text{m}0}} \frac{\bar{\rho}_0}{\rho} \left| \frac{d \ln A}{d \ln \rho} \right|. \quad (229)$$

Although for convenience we write the right-hand side in terms of the cosmological quantities  $H_0$ ,  $\bar{\rho}_0$  and  $\Omega_{\text{m}0}$  at  $z = 0$ , this expression does not depend on redshift nor on cosmology. Moreover, it is only a function of the density  $\rho$ . Then, in a density-radius plane  $(\rho, R)$ , the domain where  $|\eta| \geq 1$  is given by the area under the curve  $R_\eta(\rho)$ , where  $R_\eta(\rho)$  is the density-dependent radius defined by the right-hand side in Eq.(229).

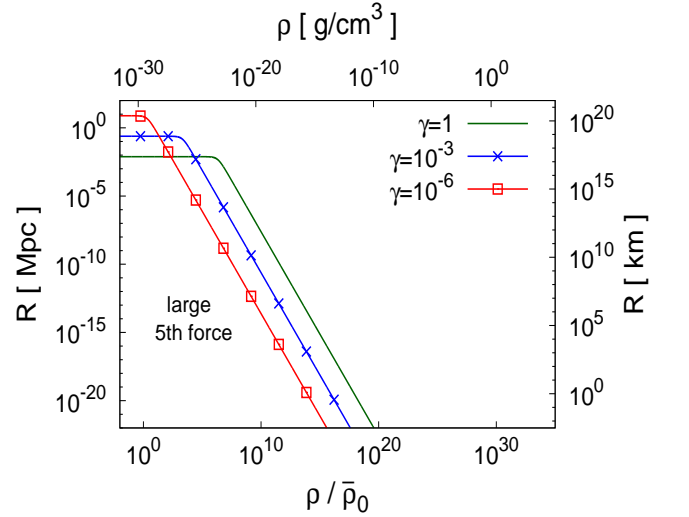


FIG. 13: Domain in the density-radius plane where the fifth force is greater than Newtonian gravity. This domain is identical for the concave and convex models with  $\gamma = \{1, 10^{-3}, 10^{-6}\}$  and  $\gamma = \{1/2, 10^{-3}, 10^{-6}\}$ . The horizontal axis is the typical density of the structure,  $\rho$ , given in units of the mean matter cosmological density today,  $\bar{\rho}_0$ , in the bottom-border scale, and in units of  $\text{g}\cdot\text{cm}^{-3}$  in the top-border scale. The vertical axis is the typical radius of the structure,  $R$ , given in Mpc in the left-border scale and in km in the right-border scale.

At low densities, we obtain from Eq.(193)

$$\rho \ll \rho_\alpha : \quad R_\eta(\rho) \sim R_\alpha \left( \frac{\rho}{\rho_\alpha} \right)^{(2\mu_- - 1)/(2 - 2\mu_-)}, \quad (230)$$

where we defined

$$R_\alpha = \frac{\alpha c}{\sqrt{\gamma} H_0}, \quad R_\alpha \sim 10 \text{ kpc for } \alpha = 10^{-6}, \gamma = 1. \quad (231)$$

Thus, if  $\mu_- = 1/2$ , at low densities we obtain a constant radius threshold, of order  $R_\alpha$ . If  $\mu_- < 1/2$  the threshold  $R_\eta(\rho)$  increases at lower densities. At high densities, we obtain from Eq.(190)

$$\rho \gg \rho_\alpha : \quad R_\eta(\rho) \sim R_\alpha \left( \frac{\rho}{\rho_\alpha} \right)^{-(2\mu_+ - 1)/(2\mu_+ - 2)}. \quad (232)$$

Thus, the threshold  $R_\eta(\rho)$  decreases at high densities. As analysed for the behavior (225) of the fifth force inside spherical halos, this decrease of the fifth-force regime at high densities is due to the convergence to a finite value  $A_+ = A(\tilde{\chi}_+)$  of the coupling function, as a constant coupling function  $A$  does not generate a fifth force. This analysis agrees with the results displayed in Fig. 13. The transition radius and density scale as  $R_\alpha \propto \alpha/\sqrt{\gamma}$  and  $\rho_\alpha \propto \gamma/\alpha$ .

To simplify the comparison with astrophysical structures, it is convenient to display the fifth-force domain

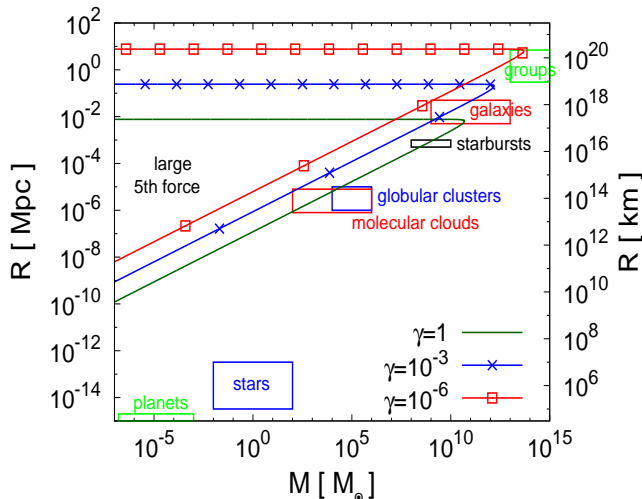


FIG. 14: Domain in the mass-radius plane where the fifth force is greater than Newtonian gravity. This domain is identical for the concave and convex models with  $\gamma = \{1, 10^{-3}, 10^{-6}\}$  and  $\gamma = \{1/2, 10^{-3}, 10^{-6}\}$ . The horizontal axis is the typical mass of the structure,  $M$ , given in units of the solar mass. The vertical axis is the typical radius of the structure,  $R$ , given in Mpc in the left-border scale and in km in the right-border scale. The rectangles show the typical scales of various astrophysical structures.

(229) in the mass-radius plane ( $M, R$ ). The low-density branch (230) writes as

$$\rho \ll \rho_\alpha : R_\eta(M) \sim R_\alpha \left( \frac{M}{M_\alpha} \right)^{-(1-2\mu_-)/(4\mu_- - 1)}, \quad (233)$$

where we defined

$$M_\alpha = \rho_\alpha R_\alpha^3, \quad M_\alpha \simeq \left( \frac{\alpha}{10^{-6}} \right)^2 \gamma^{-1/2} 10^{10} M_\odot, \quad (234)$$

while the high-density branch (232) reads as

$$\rho \gg \rho_\alpha : R_\eta(M) \sim R_\alpha \left( \frac{M}{M_\alpha} \right)^{(2\mu_+ - 1)/(4\mu_+ - 1)}. \quad (235)$$

If  $\mu_- > 1/4$ , the fifth-force domain is a triangle in the  $(\ln M, \ln R)$  plane that extends down to  $M \rightarrow 0$  and has a right corner at the maximum mass  $M_\alpha$ . Then, objects more massive than  $M_\alpha$  are not dominated by the fifth force, whatever their size. We display this diagram in Fig. 14, along with typical cosmological and astrophysical structures.

In agreement with section XI A, the fifth force is negligible for clusters and groups (at their global scale), while it is of the same order as Newtonian gravity for galaxies if  $\gamma \gtrsim 10^{-4}$ . It is interesting to note that various galactic structures, from the molecular clouds and extended starburst regions, to the overall extent of low-mass galaxies, as well as the small old globular clusters, all lie close

to the boundary of the fifth-force region if  $\gamma \gtrsim 10^{-3}$ . Thus, in agreement with Fig. 12, these objects may provide strong constraints on the models considered in this paper.

## D. Screening on astrophysical scales and in the laboratory

### 1. Screening mechanism

Alternative theories to General Relativity are strongly constrained, or even ruled out, by Solar System tests, based on the trajectories of planets around the Sun (measurements by the Cassini satellite [33]) or the motion of the Moon around the Earth (Lunar Laser Ranging experiment [34]). To remain consistent with these data, modified-gravity scenarios often involve nonlinear screening mechanisms that ensure convergence to General Relativity in small-scale and high-density environments (typically by suppressing the gradients of the scalar field or its coupling to matter). In our case, as for the ultralocal models described in [14] that obey the same equations of motion, if we consider stars, planets and moons as isolated objects in the vacuum, the screening is provided by the definition of the model itself and is 100% efficient. Indeed, because the fifth force is exactly local, as  $\mathbf{F}_A = -c^2 \nabla \ln A(\rho)$  only depends on the local density and its gradient, the impact of the Sun onto the motion of the Earth through the fifth force is exactly zero. Therefore, the Sun is completely “screened” as viewed from the Earth by the fifth force, as well as all planets and moons of the Solar System. Then, the trajectories of astrophysical objects in the Solar System are exactly given by the usual Newtonian gravity, or more accurately General Relativity, and all Solar Systems tests of gravity are satisfied, to the same accuracy as General Relativity.

This screening mechanism, which is the one of the ultralocal models [14], is different from the screening mechanisms of usual conformal coupling scenarios, leading to Yukawa interactions with matter. The four usual mechanisms are the chameleon mechanism [7–9], where the field is almost constant and short-ranged in high-density environments because its mass grows with the matter density, the Damour-Polyakov mechanism [10], where the coupling to matter vanishes in high-density environments, the K-mouflage [11, 12] and Vainshtein [13] mechanisms, where gradients of the scalar field are suppressed by the nonlinearities of the kinetic term (i.e., the Lagrangian includes terms of higher order than quadratic over the field derivatives, that involve  $\partial\varphi$  or  $\square\varphi$ ). In contrast, the ultralocal screening does not rely on the suppression of the scalar field gradients, but on their local character. Because of the lack of propagation, the fifth force is essentially short-ranged and insensitive to distant masses. This may be seen as an extreme limit of the chameleon mechanism.

In the case of the models with kinetic conformal cou-

pling that we study in this paper, the scalar-field Lagrangian includes a kinetic term and the equation of motion (66) includes derivative terms and looks like a modified Klein-Gordon equation. However, it admits the ultralocal non-propagating solution (71), which recovers the ultralocal screening mechanism.

## 2. Fifth-force pressure

Even though the fifth force on the Earth is not significantly influenced by the Sun and other planets, it does not vanish as it is sensitive to the local gradient of the matter density. Then, we must check that this local force is small enough to have avoided detection in the laboratory or on the Earth (e.g., at its surface or in the atmosphere). As seen in Eq.(113), the local nature of the scalar field (more precisely of its kinetic term  $\tilde{\chi}$ ) makes the fifth force appear as a polytropic pressure  $p_A(\rho)$ , given by Eq.(114), where  $\rho$  is now the baryonic matter density as the dark matter density and its gradient can be neglected. Since  $\mathcal{M}^4 \sim \bar{\rho}_{\text{de}0}$ , and  $\tilde{\chi} \leq \gamma$  for the models considered in this paper, we obtain for a typical density of  $1 \text{ g/cm}^3$ ,

$$\rho \sim 1 \text{ g.cm}^{-3} : \frac{p_A}{\rho} \sim 3 \times 10^{-13} \gamma \text{ (m/s)}^2. \quad (236)$$

This corresponds to very small velocities and motions, for any  $\gamma \leq 1$ . To compare this pressure with the thermal motions found on the Earth or in the laboratory, we write Eq.(236) as a temperature,

$$\frac{m_p p_A}{\rho k_B} \sim 3 \times 10^{-17} \gamma \text{ K}, \quad (237)$$

where again we chose  $\rho \sim 1 \text{ g/cm}^3$ ,  $m_p$  is the proton mass and  $k_B$  the Boltzmann constant. This gives a very low temperature that is much smaller than the temperature reached by cold-atoms experiments in the laboratory,  $T \sim 10^{-7} \text{ K}$ . Thus, the fifth force can be neglected in the laboratory and on the Earth, and in other astrophysical objects.

## XII. NONLINEAR ANALYSIS OF THE CONVEX MODELS

As we noticed in section XIB, within a mean-field (i.e. spherically-averaged) analysis the fifth force can be greater than Newtonian gravity at intermediate radii in low-mass halos,  $M \lesssim 10^{11} h^{-1} M_\odot$ , if  $\gamma \gtrsim 10^{-4}$ . As in [14], we pointed out that for the convex models this problem may be circumvented by nonlinearities, which could lead to a fragmentation of the system and a screening of the fifth force, due to its locality, as described in section XID. On the other hand, these nonlinearities may also invalidate the analysis of cosmological perturbations presented in section IX. Indeed, this linear analysis assumes that the fifth-force gradients on large cosmological

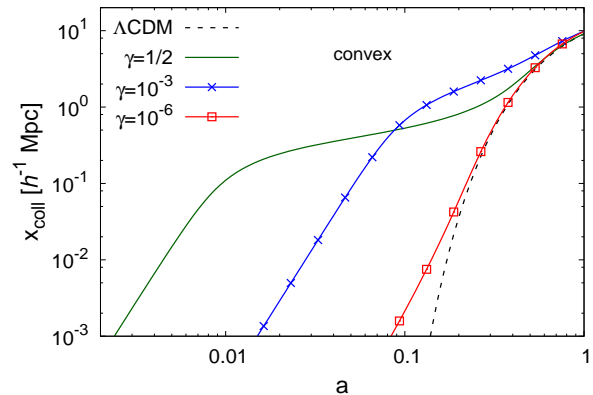


FIG. 15: Nonlinear transition scale  $x_{\text{coll}}(a)$  (in comoving coordinates) as a function of the scale factor  $a$  for the convex models.

scales are set by the large-scale density gradients. This may no longer hold if strong small-scale inhomogeneities develop, which make the fifth force independent of large-scale density gradients.

Following [14], in this section we first obtain the scale associated with the cosmological nonlinear transition. Then, to go beyond perturbation theory and spherically-symmetric approximations, we use a thermodynamical approach to obtain the phase diagram associated with the fifth force. Next, we compare this phase diagram with the trajectories associated with the cosmological nonlinear transition, and with the density profiles inside halos.

### A. Evolution of the cosmological nonlinear transition for the convex model

We show in Fig. 15 the comoving cosmological nonlinear transition scale  $x_{\text{coll}}(a)$ , defined by

$$\Delta_L^2(\pi/x_{\text{coll}}, z) = 1.5 \quad (238)$$

Because of the faster growth of density fluctuations on small scales, analysed in sections IX C and X D, the comoving scale  $x_{\text{coll}}$  is much greater than the  $\Lambda$ -CDM prediction at high redshift. It shows a steady rise for  $a < a_\alpha$ , when the characteristic fifth-force factor  $\epsilon_1(a)$  keeps growing with cosmic time as seen in the lower panel in Fig. 2. For the case  $\gamma = 1/2$ , in the time range  $a_\alpha \lesssim a \lesssim 0.3$ ,  $x_{\text{coll}}$  is roughly constant, which means that the hierarchical formation process stops as no larger structures collapse. This is due to the fast decrease of  $\epsilon_1(a)$ . It means that the fifth force decays with time, so that it cannot generate the collapse of greater structures, and we need to wait until  $a \simeq 0.3$  for Newtonian gravity to take the lead and generate the collapse of larger structures. Then, at low redshift we recover the  $\Lambda$ -CDM behavior. For  $\gamma = 10^{-6}$  this plateau does not exist because

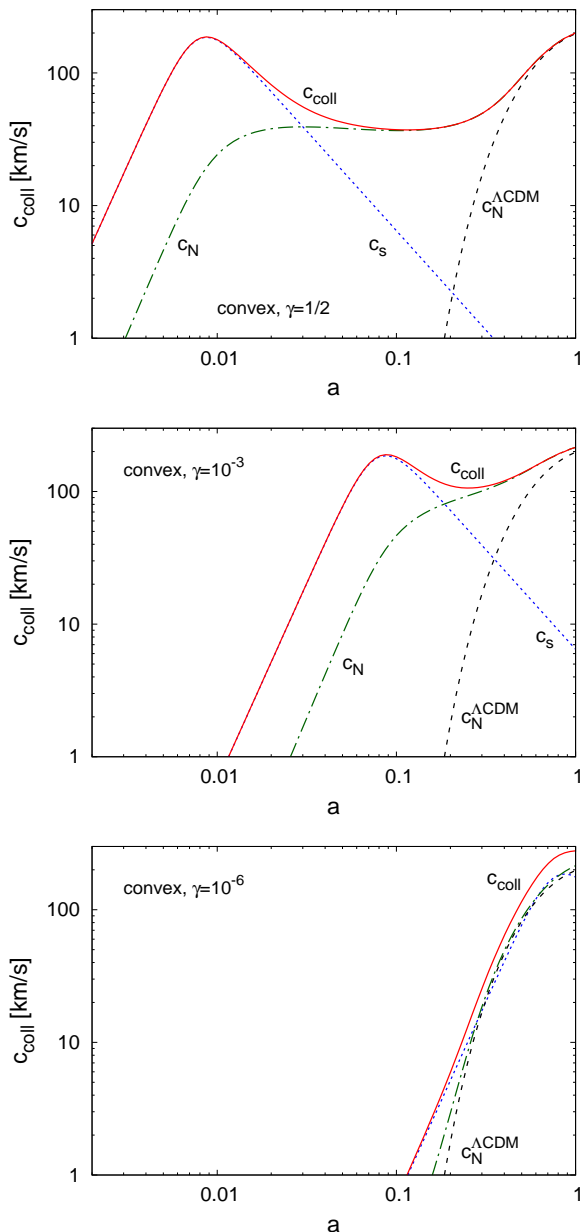


FIG. 16: Collapse velocity scale  $c_{\text{coll}}(a)$  (solid line) for the convex models. The dotted and dot-dashed lines are  $c_s$  and  $c_N$ , whereas the dashed line on the right is the result  $c_{\text{coll}}^{\Lambda\text{-CDM}} = c_N^{\Lambda\text{-CDM}}$  in the case of the  $\Lambda$ -CDM cosmology.

the fifth-force peak occurs at low redshift where Newtonian gravity also becomes dominant. The case  $\gamma = 10^{-3}$  gives an intermediate configuration.

For the thermodynamic analysis presented in section XII B below, we need the initial kinetic energy or typical velocity of the collapsing region. From the evolution equation (117) of the linear density, we define an effective velocity scale  $c_{\text{coll}}$  by

$$c_{\text{coll}}^2(a) = c_s^2 + c_N^2, \quad (239)$$

with

$$c_s^2 = \epsilon_1 c^2, \quad c_N^2 = (1 + \epsilon_1) \frac{3\Omega_m}{2\pi^2} (H a x_{\text{coll}})^2. \quad (240)$$

The factor  $c_s^2$  comes from the pressure-like term  $\epsilon_1 c^2 \nabla^2 \delta$  in Eq.(117), while the term  $c_N^2$  comes from the right-hand side, associated with the usual gravitational force (amplified by the negligible factor  $\epsilon_1$ ). We show our results in Fig. 16. We also display the case of the  $\Lambda$ -CDM cosmology where  $c_{\text{coll}}^{\Lambda\text{-CDM}} = c_N^{\Lambda\text{-CDM}}$  as there is no pressure-like term.

Let us first consider the upper panel with  $\gamma = 1/2$ . The component  $c_s$ , due to the pressure-like term associated with the fifth-force, dominates at high redshift. Its amplitude follows the rise and fall of  $\epsilon_1(a)$  displayed in Fig. 2. This also explains the rise until  $a_\alpha$  and next the stop of  $x_{\text{coll}}(a)$ . The component  $c_N$ , associated with the Newtonian gravity, explicitly depends on the scale  $x_{\text{coll}}(a)$ . It grows with time, along with  $x_{\text{coll}}(a)$ , and dominates at late times,  $a \gtrsim 0.03$ . The plateau for  $0.01 \lesssim a \lesssim 0.3$  follows from the very slow growth of  $x_{\text{coll}}(a)$  found in Fig. 15 in this redshift range. At late times we recover the standard  $\Lambda$ -CDM behavior. Thus, we can distinguish three regimes from Fig. 16. At early times,  $a < 0.01$ , the fifth force dominates and increasingly large scales enter the nonlinear regime. This is the period when the thermodynamic analysis of section XII B below applies and allows us to estimate the behavior of the system in the nonlinear regime. For  $0.01 < a < 0.3$ , the hierarchical process of structure formation stops, as the fifth force decreases and becomes subdominant with respect to Newtonian gravity, which is still weak on these scales. Finally, for  $0.3 < a < 1$ , we recover the  $\Lambda$ -CDM behavior, as Newtonian gravity is dominant and strong enough to generate the collapse of new greater scales, which have never been strongly modified by earlier fifth-force effects.

In the lower panel with  $\gamma = 10^{-6}$ , we find that the deviation from the  $\Lambda$ -CDM velocity scale is much smaller, as the fifth force is negligible at high redshift and only becomes significant at low  $z$ , where however it does not become greater than Newtonian gravity on cosmological scales. This is because Newtonian gravity already gives  $c_N \sim 300$  km/s for the cosmological scales that turn nonlinear today, which is of the same order as the maximum value  $\max(c_s^2) = \max(\epsilon_1) c^2 \simeq \alpha c^2$ . The case  $\gamma = 10^{-3}$  is closer to the case  $\gamma = 1/2$ , as there is a distinct fifth-force era around  $a_\alpha = 0.1$ .

We can note that in the case  $\gamma = 1/2$  this history singles out a characteristic mass and velocity scale, associated with the plateau found in Fig. 16,

$$\gamma = 1/2 : \quad x_* \sim 0.355 h^{-1} \text{Mpc}, \quad c_* \sim 50 \text{ km/s}, \\ M_* \sim 2 \times 10^{10} h^{-1} M_\odot. \quad (241)$$

As in Fig. 14, we recover the scales associated with small galaxies. However, it is not clear whether this could alleviate or worsen some of the problems encountered on

galaxy scales by the standard  $\Lambda$ -CDM scenario. This would require detailed numerical studies that are beyond the scope of this paper.

### B. Thermodynamic equilibrium in the fifth-force regime for the convex model

So far we have implicitly assumed that during the initial phase  $a < a_\alpha$  of structure formation, governed by the fifth force in the cases  $\gamma = 1/2$  and  $10^{-3}$ , the density field remains smooth on cosmological scales, so that a standard linear analysis of matter cosmological perturbations can be applied. This is not obvious because small scales,  $x \leq x_{\text{coll}}(a_\alpha)$ , have already turned nonlinear at high redshift,  $z > z_\alpha$ . Then, the density field could have become strongly inhomogeneous, and the gradient of the fifth-force potential  $\nabla \ln A$  at a given location in space would be unrelated with the gradient of the density field smoothed on cosmological scales. This strong sensitivity to the small-scale distribution of the density field does not arise for the Newtonian gravitational force, because the Newtonian potential is given by the Poisson equation,  $\Psi_N \propto \nabla^{-2} \rho$ , which regularizes the density field, whereas the fifth force potential  $\ln A$  is a direct function of the local density through Eq.(111). This issue only arises in the first stage  $a < a_\alpha$  found in Fig. 15, where new scales enter the nonlinear regime and are dominated by the fifth force.

To address this question we need to go beyond perturbation theory and spherical dynamics, as this is a highly nonlinear and inhomogeneous problem. Following [14], we use a thermodynamic analysis, which provides a simple analytic framework. Assuming that the scales that turn nonlinear because of the fifth force at high redshift reach a statistical equilibrium through the rapidly changing effects of the fluctuating potential, in a fashion somewhat similar to the violent relaxation that takes place for gravitational systems [35], we investigate the properties of this thermodynamic equilibrium. This first requires the study of the phase transitions and of the phase diagram associated with the potential  $\ln A(\rho)$  that defines our model. Because this issue arises from the behavior of the fifth force in the regime where it dominates over Newtonian gravity, we can neglect the latter to investigate this point. Note that contrary to the usual gravitational case, the potential  $\ln A$  is both bounded and short-ranged, so that we cannot build infinitely large negative (or positive) potential energies and a stable thermodynamic equilibrium always exists, and it is possible to work with either micro-canonical, canonical or grand-canonical ensembles. In this respect, a thermodynamic analysis is better suited for such systems than for standard 3D gravitational systems, where the potential energy is unbounded from below and stable equilibria do not always exist, and different statistical ensembles are not equivalent [36].

We refer to [14] for the derivation of the thermodynam-

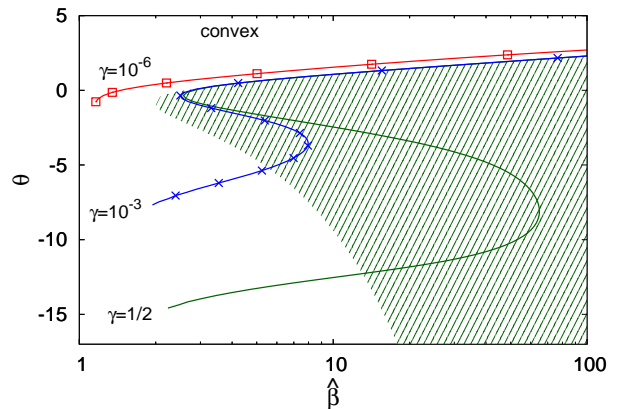


FIG. 17: Thermodynamic phase diagram of the convex models. The shaded area is the region of initial inverse temperature  $\hat{\beta}$  and density  $\theta$  where the system reaches an inhomogeneous thermodynamic equilibrium. The white area corresponds to the homogeneous phase. The solid lines are the cosmological trajectories  $(\hat{\beta}_{\text{coll}}(a), \theta_{\text{coll}}(a))$ , for  $\gamma = 1/2, 10^{-3}$ , and  $10^{-6}$  from bottom to top.

ical diagram associated with the fifth-force potential  $\ln A$ . The main result is that we have a first-order phase transition, between a high-temperature homogeneous phase and a low-temperature inhomogeneous phase. Defining the dimensionless inverse temperature  $\hat{\beta}$  and density  $\theta$ ,

$$\hat{\beta} = \frac{\alpha c^2}{k_B T}, \quad \theta = \ln \hat{\rho}, \quad (242)$$

the inhomogeneous phase is shown by the shaded area in Fig. 17, while the white area is the homogeneous phase. In terms of the normalized inverse temperature  $\hat{\beta}$  and density  $\theta$  the phase diagram no longer depends on the parameters  $\alpha$  and  $\gamma$ , so that all three convex models computed in this paper have the same phase diagram as displayed in Fig. 17. For a given normalized density  $\theta$ , the inhomogeneous phase extends to the right up to infinite  $\hat{\beta}$ , i.e. down to zero temperature  $T$ . The leftmost point of the inhomogeneous phase defines the critical temperature  $T_c$ , which for the convex model (184) is given by

$$\hat{\beta}_c = \frac{15(11 - \sqrt{105})\sqrt{15 + \sqrt{105}}}{4(\sqrt{105} - 3)} \simeq 1.96 \quad (243)$$

At low temperature the high- and low-density boundaries of the inhomogeneous phase obey the asymptotic behaviors

$$\hat{\beta} \rightarrow \infty : \quad \theta_+ \sim \frac{1}{2} \ln(\hat{\beta}), \quad \theta_- \sim -\hat{\beta}. \quad (244)$$

Then, if we consider a region of space with average initial temperature and density,  $(1/\hat{\beta}, \theta)$ , which fall outside of the shaded region, the system remains in the homogeneous phase. If the initial condition falls inside the shaded region, the system becomes inhomogeneous and

splits over domains with density  $\theta_-$  or  $\theta_+$ , with a proportion such that the total mass over the full volume is conserved.

### C. Cosmological trajectory in the phase diagram

The solid curves in Fig. 17 give the cosmological trajectories in the phase diagram associated with the non-linear transition scale,  $x_{\text{coll}}(a)$  of Eq.(238) and Fig. 15, for  $\gamma = 1/2, 10^{-3}$ , and  $10^{-6}$ . To this scale we associate the mean density of the Universe,  $\rho_{\text{coll}}(a) = \bar{\rho}(a)$ , as the transition corresponds to density contrasts of order unity, hence

$$\rho_{\text{coll}}(a) = \bar{\rho}(a), \quad \theta_{\text{coll}}(a) = \ln \left[ \frac{\alpha \bar{\rho}(a)}{\gamma \mathcal{M}^4} \right], \quad (245)$$

and the inverse temperature

$$\beta_{\text{coll}}(a) = \frac{1}{c_{\text{coll}}^2(a)} \quad \text{hence} \quad \hat{\beta}_{\text{coll}}(a) = \frac{\alpha c^2}{c_{\text{coll}}^2(a)}. \quad (246)$$

As cosmic time grows and the density  $\rho_{\text{coll}}(a)$  decreases the cosmological trajectory runs downwards in Fig. 17.

Let us first consider the case  $\gamma = 1/2$ . In agreement with Fig. 16, the inverse temperature  $\hat{\beta}_{\text{coll}}$  first decreases until  $a \simeq 0.01$ , as the velocity  $c_{\text{coll}}$  grows. Next,  $\hat{\beta}_{\text{coll}}$  increases while  $c_{\text{coll}}(z)$  decreases until  $a \simeq 0.2$ , when we recover the  $\Lambda$  – CDM behavior, and  $\hat{\beta}_{\text{coll}}$  decreases again thereafter. We are interested in the first era,  $a < a_\alpha$ , when the hierarchical process of structure formation is governed by the fifth force, and we find that the cosmological trajectory is almost indistinguishable from the upper boundary  $\theta_+(\hat{\beta})$  of the inhomogeneous thermodynamic phase. Indeed, from Eq.(239) and Fig. 16 we have at early times  $c_{\text{coll}} \simeq c_s$ , hence  $\hat{\beta}_{\text{coll}} \simeq \alpha/\epsilon_1$ . Using Eq.(187), we have at high densities, which also correspond to  $a < a_\alpha$ ,  $\epsilon_1 \simeq \alpha/\hat{\rho}^2 = \alpha e^{-2\theta}$ , hence

$$a \ll a_\alpha : \quad \theta_{\text{coll}} \sim \frac{1}{2} \ln(\hat{\beta}_{\text{coll}}), \quad (247)$$

and we recover the asymptote (244) of  $\theta_+(\hat{\beta})$ . This means that, according to the thermodynamic analysis, the cosmological density field does not develop strong inhomogeneities that are set by the cutoff scale of the theory when it enters the fifth-force nonlinear regime. Therefore, density gradients remain set by the large-scale cosmological density gradients and the analysis of the linear growing modes in section IX C and of the spherical collapse in section X C are valid. Of course, on small non-linear scales and at late times, where Newtonian gravity becomes dominant, we recover the usual gravitational instability that we neglected in this analysis and structure formation proceeds as in the standard  $\Lambda$ -CDM case.

For the case  $\gamma = 10^{-3}$  we recover the same S-shape for the cosmological trajectory, but the low-density part is shorter, because the redshift  $z_\alpha$  is lower, and corresponds

to a higher normalized density because of the factor  $\gamma$  in the definition of  $\theta$  in Eq.(245). We again have the high-density behavior (247), which does not depend on  $\gamma$ , and we recover the same conclusions as for  $\gamma = 1/2$ .

For the case  $\gamma = 10^{-6}$  the cosmological trajectory no longer shows the S-shape. This is because  $z_\alpha \sim 1$  and there is no longer an intermediate era where structure formation stops as the fifth force declines while Newtonian gravity increases but remains small, at the scale  $x_{\text{coll}}$ , in agreement with Figs. 15 and 16. Then, the cosmological trajectory always remains in the homogeneous phase.

Therefore, in all cases the analysis of the linear growing modes in section IX C and of the spherical dynamics in section X C are valid.

### D. Halo profiles

We show in Fig. 18 the trajectories over the phase diagram associated with density profiles in spherical halos, with a NFW profile [32]. Within a radius  $r$  inside the halo, the averaged reduced density is

$$\theta_r = \ln \left[ \frac{\alpha \rho(< r)}{\gamma \mathcal{M}^4} \right] = \ln \left[ \frac{\alpha 3M(< r)}{\gamma 4\pi r^3 \mathcal{M}^4} \right], \quad (248)$$

and we write the reduced inverse temperature as

$$\hat{\beta}_r = \frac{\alpha c^2}{\text{Max}(c_s^2, v_N^2)}, \quad (249)$$

where  $v_N$  is the circular velocity (216) associated with the Newtonian gravity while  $c_s$  is the velocity scale (217) associated with the fifth force. We choose the non-analytic interpolation  $\text{Max}(c_s^2, v_N^2)$  instead of the smooth interpolation  $c_s^2 + v_N^2$ , which we used in Eq.(239) for the cosmological analysis, for illustrative convenience. Indeed, the discontinuous changes of slope in Fig. 18 show at once the location of the transition  $|\eta| = 1$  between the fifth-force and the Newtonian gravity regimes. As we move inside the halo, towards smaller radii  $r$ , the density  $\theta_r$  grows and we move upward in Fig. 18.

Let us first consider the case  $\gamma = 1/2$  of the upper panel. The turn-around of  $\hat{\beta}_r$  at  $\theta_r \simeq -4$  corresponds to the NFW radius  $r_s$  where the local slope of the density goes through  $\gamma = 2$  and the circular velocity  $v_N$  is maximum. In agreement with Fig. 12, for high-mass halos,  $M \gtrsim 10^{13} h^{-1} M_\odot$ , Newtonian gravity dominates at all radii and there is no discontinuity in the radial trajectory as the maximum in Eq.(249) is always  $v_N^2$ . Moreover, we are always in the homogeneous phase, so that the subdominant fifth force does not lead to further fragmentation of the system. For low-mass halos,  $M \lesssim 10^{13} h^{-1} M_\odot$ , the fifth force becomes dominant at intermediate radii, between the two discontinuous changes of slope of the radial trajectory. Moreover, a significant part of the outer halo falls in the inhomogeneous thermodynamic phase. This suggests a fragmentation of the system in the outer regions into smaller substructures,

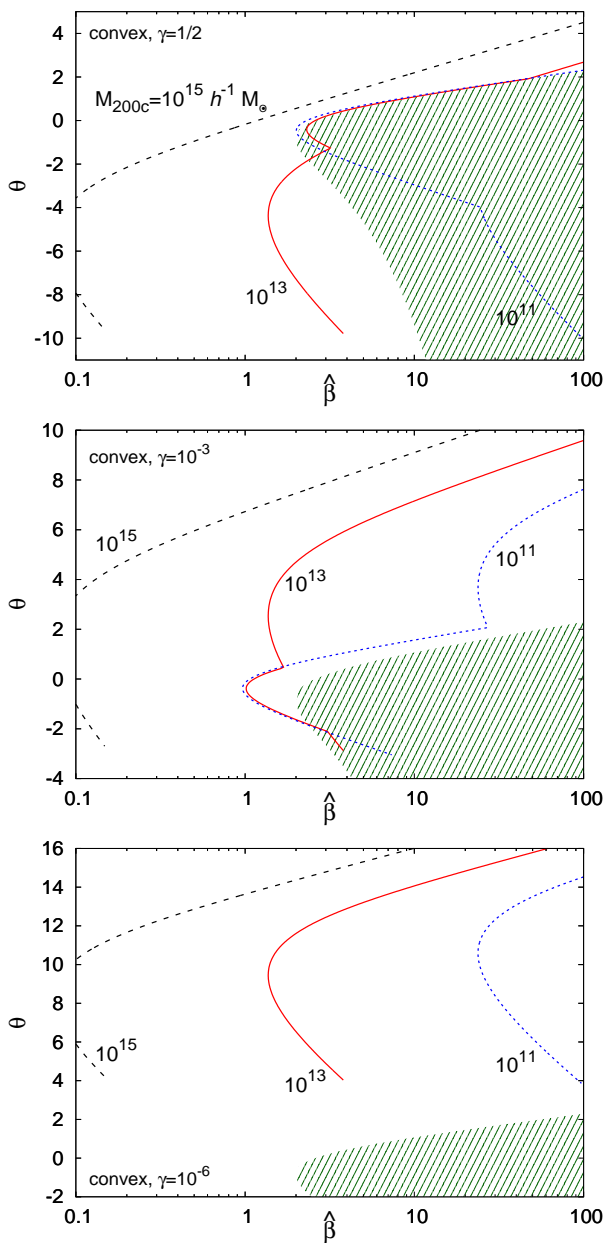


FIG. 18: Radial trajectories ( $\hat{\beta}_r, \theta_r$ ) over the thermodynamic phase diagram inside halos of mass  $M_{200c} = 10^{15}, 10^{13}$  and  $10^{11} h^{-1} M_{\odot}$ , at  $z = 0$  for the convex models.

which could give rise to some observational signatures. This nonlinear process would next lead to a screening of the fifth force, as discussed for the Solar System and the Earth in section XID, because of the ultralocal character of the fifth force and the disappearance of large-scale collective effects.

In the case  $\gamma = 10^{-3}$ , as compared with  $\gamma = 1/2$  the radial trajectories move upward with respect to the phase diagram in the normalized coordinates  $(\hat{\beta}, \theta)$  because of the factor  $\gamma$  in Eq.(248). Then, even for  $M \sim$

$10^{11} h^{-1} M_{\odot}$  most of the radial trajectory is within the homogeneous phase. This suggests that nonlinearities may not lead to a fragmentation of the system and that the spherically-averaged analysis would be valid. Then, because we found in Fig. 12 that for  $M \sim 10^{11} h^{-1} M_{\odot}$  this analysis gives a fifth force that is significantly greater than Newtonian gravity these models are probably ruled out by observations.

In the case  $\gamma = 10^{-6}$  shown in the lower panel, the full radial trajectories are within the homogeneous phase, so that the spherically-averaged analysis is valid for all masses  $M \gtrsim 10^9 h^{-1} M_{\odot}$ . Because we found in Fig. 12 that for these masses this analysis gives a fifth force that is smaller than Newtonian gravity these models are consistent with observations.

### XIII. CONCLUSION

We have investigated the low-energy regime of particle physics models where the standard model particles, e.g. the fermions such as the electron, as well as the dark matter, are coupled to a hidden sector comprising a scalar field charged under an Abelian symmetry. At energies below the symmetry breaking scale, which is taken here to be of the meV order of magnitude, the remaining Goldstone mode couples derivatively to the standard model fields. In particular, it couples to Cold Dark Matter and, on coarse-grained scales larger than 1 mm, the presence of this coupling can have an influence both on the cosmology of the late-time Universe and the astrophysics of large-scale structures.

On the cosmological side, the potential energy in the Goldstone sector can serve as the vacuum energy leading to the late cosmic acceleration. Moreover, the existence of a massless scalar field coupled to matter is not in contradiction with local tests of gravity as the coupling is ultralocal and the fifth force between isolated compact objects vanishes. On the other hand, within extended structures with large-scale density gradients, the coupling between matter and the scalar field can lead to several effects.

First of all, the linear growth of structures on very large scales, larger than 10 Mpc, is either increased if the coupling function  $\ln[A(\tilde{\chi})]$ , where  $\chi$  is the normalized kinetic term of the Goldstone mode, is convex, or decreased if the function is concave. Thus, this class of models can either amplify or damp the formation of large-scale structures. This can be contrasted to many modified-gravity models, such as chameleon or K-mouflage scenarios, where the fifth force is always attractive and amplifies Newtonian gravity (because stability constraints restrict the sign of the coupling parameters).

In the convex case, this could lead to more structure and more clumped objects on nonlinear scales smaller than 10 Mpc. We use a thermodynamical analysis to show that there is no catastrophic formation of very small high-density clumps at high redshifts. In the concave

case, fewer small structures are formed in a way more akin to Warm Dark Matter scenarios. Depending on the value of the model parameters, the dynamics inside halos can also be significantly modified. In the convex case where structure formation is enhanced, in the outer shells of massive halos a thermodynamic phase transition could take place with the formation of two phases containing two different populations of objects. Such a mixing phenomenon is beyond the reach of this article and should be analyzed with numerical simulations. This could provide interesting signatures for these models and we hope to come back to these issues in the near future. In the concave case, the repulsiveness of the fifth force is expected to damp nonlinearities, but if it is too large as compared with Newtonian gravity it would modify the velocity and density profiles of galactic halos.

Thus, as for the ultralocal models, these kinetic conformal coupling models are very close to the  $\Lambda$ -CDM background but can generate significant deviations on nonlinear cosmological scales, which increase on smaller scales. In particular, for realistic models these deviations peak on galactic scales, which could be interesting as the  $\Lambda$ -CDM cosmology encounters some tension with observations on these scales. Both models share the same screening mechanism on small astrophysical scales, due to the ultralocal behavior of the fifth force, which does not propagate. This screening mechanism is different from the usual chameleon, Damour-Polyakov, K-mouflage and Vainshtein screening mechanisms of conformal coupling scenarios with Yukawa interactions to matter.

As compared with the ultralocal models, the kinetic conformal coupling models show two main theoretical and observational differences: a) they can be associated with an Abelian symmetry and Goldstone modes, which gives an additional motivation for the form of the Lagrangian, and b) they can lead to both an attractive or a repulsive fifth force, depending on the choice of the coupling function. For the ultralocal models the case of a repulsive force is theoretically disfavored because the model becomes unstable with respect to the addition of a small positive kinetic term, which is expected in realistic scenarios as it is not forbidden by some symmetry. For the kinetic conformal coupling models studied in this paper this issue does not arise and the sign of the fifth force is not constrained by such stability requirements.

In conclusion, the Goldstone models provide a new screening mechanism of scalar forces in local environments whilst it can lead to interesting effects on both the formation of structure and astrophysics on galactic scales. It would be interesting to analyse the very non-linear regime of these models beyond the analytical treatment that we have given here. For that, numerical simulations are required and we hope to be able to study this scenario in the near future.

## XIV. CONCLUSION

### Acknowledgments

This work is supported in part by the French Agence Nationale de la Recherche under Grant ANR-12-BS05-0002.

### Appendix A: Change of frame and fermions

We consider massive Dirac fermions  $\psi$  in the Jordan frame with the action

$$S_\psi = - \int d^4x \sqrt{-g} (i\bar{\psi}\gamma^\mu\nabla_\mu\psi + m_\psi\bar{\psi}\psi) \quad (\text{A1})$$

and the change of frame

$$g_{\mu\nu} = A^2(\varphi, \tilde{\chi}) \tilde{g}_{\mu\nu}, \quad (\text{A2})$$

where the conformal change of metric is an arbitrary function of  $\varphi$  and  $\tilde{\chi} = -\tilde{g}^{\mu\nu}\partial_\mu\varphi\partial_\nu\varphi/(2M^4)$ . The covariant derivative involves the spin connection and reads

$$\nabla_\mu = \partial_\mu + \frac{1}{4}\gamma^{ab}\omega_{ab\mu}, \quad (\text{A3})$$

where  $a, b$  are Lorentz flat indices raised and lowered with the Minkowski metric  $\eta_{ab}$  while  $\mu$  is a curved index. The  $\gamma^a$  matrices are such that

$$\{\gamma^a, \gamma^b\} = 2\eta^{ab} \quad (\text{A4})$$

and we have introduced the commutator

$$\gamma^{ab} = \frac{1}{2}[\gamma^a, \gamma^b]. \quad (\text{A5})$$

The spin connection is most easily calculated using the Cartan formalism. Defining the vielbeins such that

$$g_{\mu\nu} = \eta_{ab}e_\mu^a e_\nu^b \quad (\text{A6})$$

and the one-form  $e^a = e_\mu^a dx^\mu$ , the torsion-free condition implies that

$$de^a + \omega_b^a \wedge e^b = 0, \quad (\text{A7})$$

and the one-form  $\omega_b^a$  defines the spin connection

$$\omega_b^a = \omega_{b\mu}^a dx^\mu. \quad (\text{A8})$$

Upon changing frame the vielbeins transform as

$$e_\mu^a = A\tilde{e}_\mu^a, \quad (\text{A9})$$

the Dirac matrices become

$$\gamma^\mu = A^{-1}\tilde{\gamma}^\mu, \quad (\text{A10})$$

where  $\gamma^\mu = e_a^\mu \gamma^a$ . We also redefine the Dirac fields as

$$\psi = A^{-3/2}\tilde{\psi}, \quad (\text{A11})$$

which gives

$$\partial_\mu \psi = A^{-3/2} \left( \partial_\mu \tilde{\psi} - \frac{3}{2} \frac{\partial_\mu A}{A} \tilde{\psi} \right). \quad (\text{A12})$$

Using (A7) and defining

$$d\tilde{e}^a + \tilde{\omega}_b^a \wedge \tilde{e}^b = 0, \quad (\text{A13})$$

we find that

$$\omega_{ab} = \tilde{\omega}_{ab} + \frac{\partial_\mu A}{A} (\tilde{e}_b^\mu \tilde{e}_a - \tilde{e}_a^\mu \tilde{e}_b), \quad (\text{A14})$$

which is antisymmetric in  $(ab)$ . As a result we find that

$$\begin{aligned} \gamma^\mu \nabla_\mu \psi &= A^{-5/2} \tilde{\gamma}^\mu \left( \tilde{\nabla}_\mu \tilde{\psi} - \frac{3}{2} \frac{\partial_\mu A}{A} \tilde{\psi} \right. \\ &\quad \left. + \frac{1}{2} \frac{\partial_\nu A}{A} \tilde{e}_b^\nu \tilde{e}_{a\mu} \gamma^{ab} \tilde{\psi} \right), \end{aligned} \quad (\text{A15})$$

and upon using  $\tilde{\gamma}^\mu (\tilde{\gamma}_\mu \tilde{\gamma}^\nu - \gamma^\nu \tilde{\gamma}_\mu) = 6\tilde{\gamma}^\nu$  we find that

$$\gamma^\mu \nabla_\mu \psi = A^{-5/2} \tilde{\gamma}^\mu \tilde{\nabla}_\mu \tilde{\psi}. \quad (\text{A16})$$

As a result the fermionic action becomes

$$S_\psi = - \int d^4x \sqrt{-\tilde{g}} (i\tilde{\psi} \tilde{\gamma}^\mu \tilde{\nabla}_\mu \tilde{\psi} + A(\tilde{\chi}) m_\psi \tilde{\psi} \tilde{\psi}). \quad (\text{A17})$$

In particular, the mass in the Einstein frame can be identified with

$$\tilde{m}_\psi = A m_\psi. \quad (\text{A18})$$

- 
- [1] S. Perlmutter et al. (Supernova Cosmology Project), *Astrophys.J.* **517**, 565 (1999), astro-ph/9812133.
- [2] A. G. Riess et al. (Supernova Search Team), *Astron.J.* **116**, 1009 (1998), astro-ph/9805201.
- [3] J. Goldstone, A. Salam, and S. Weinberg, *Phys. Rev.* **127**, 965 (1962).
- [4] E. J. Copeland, M. Sami, and S. Tsujikawa, *Int.J.Mod.Phys.* **D15**, 1753 (2006), hep-th/0603057.
- [5] C. Will, *Pramana* **63**, 731 (2004).
- [6] J. Khoury (2010), 1011.5909.
- [7] J. Khoury and A. Weltman, *Phys.Rev.Lett.* **93**, 171104 (2004), astro-ph/0309300.
- [8] J. Khoury and A. Weltman, *Phys. Rev.* **D69**, 044026 (2004), astro-ph/0309411.
- [9] P. Brax, C. van de Bruck, A.-C. Davis, J. Khoury, and A. Weltman, *Phys. Rev.* **D70**, 123518 (2004), astro-ph/0408415.
- [10] T. Damour and A. M. Polyakov, *Nucl. Phys.* **B423**, 532 (1994), hep-th/9401069.
- [11] E. Babichev, C. Deffayet, and R. Ziour, *Int.J.Mod.Phys.* **D18**, 2147 (2009), 0905.2943.
- [12] P. Brax and P. Valageas, *Phys. Rev. D* **90**, 023508 (2014), 1403.5424.
- [13] A. Vainshtein, *Phys.Lett.* **B39**, 393 (1972).
- [14] P. Brax, L. A. Rizzo, and P. Valageas, *Phys. Rev. D* **94**, 044027 (2016), 1605.02938.
- [15] J. Gleyzes, D. Langlois, F. Piazza, and F. Vernizzi, *Phys. Rev. Lett.* **114**, 211101 (2015), 1404.6495.
- [16] J. Gleyzes, D. Langlois, F. Piazza, and F. Vernizzi, *JCAP* **1502**, 018 (2015), 1408.1952.
- [17] M. Crisostomi, M. Hull, K. Koyama, and G. Tasinato, *JCAP* **1603**, 038 (2016), 1601.04658.
- [18] G. W. Horndeski, *Int.J.Theor.Phys.* **10**, 363 (1974).
- [19] C. Deffayet, X. Gao, D. Steer, and G. Zahariade, *Phys.Rev.* **D84**, 064039 (2011), 1103.3260.
- [20] J. D. Bekenstein, *Phys. Rev.* **D48**, 3641 (1993), gr-qc/9211017.
- [21] A. Katz and M. Perelstein, *JHEP* **07**, 108 (2014), 1401.1827.
- [22] P. Brax, L. A. Rizzo, and P. Valageas, *Phys. Rev. D* **94**, 023512 (2016), 1605.05946.
- [23] J. R. Klauder, *Beyond Conventional Quantization* (Cambridge University Press, 2005).
- [24] R. J. Rivers, *Path integral methods in quantum field theory* (Cambridge University Press, 1990).
- [25] L. C. Evans, *Partial differential equations*, vol. 19 of *Graduate studies in mathematics* (American Mathematical Society, 2010).
- [26] M. G. Crandall and P.-L. Lions, *Trans. Amer. Math. Soc.* **277**, 1 (1983).
- [27] M. G. Crandall and P.-L. Lions, *Trans. Amer. Math. Soc.* **282**, 487 (1984).
- [28] P. Cannarsa and C. Sinestrari, *Semiconcave functions, Hamilton-Jacobi equations, and optimal control* (Birkhauser Boston, 2004).
- [29] D. Tonon, Ph.D. thesis, SISSA (2011).
- [30] W. H. Press and P. Schechter, *Astrophys. J.* **187**, 425 (1974).
- [31] P. Valageas, *Astr. & Astrophys.* **508**, 93 (2009), 0905.2277.
- [32] J. F. Navarro, C. S. Frenk, and S. D. M. White, *Astrophys. J.* **462**, 563 (1996), astro-ph/9508025.
- [33] B. Bertotti, L. Iess, and P. Tortora, *Nature* **425**, 374 (2003).
- [34] J. G. Williams, S. G. Turyshev, and D. H. Boggs, *Phys.Rev.Lett.* **93**, 261101 (2004), gr-qc/0411113.
- [35] D. Lynden-Bell, *Mon. Not. R. Astr. Soc.* **136**, 101 (1967).
- [36] T. Padmanabhan, *Phys. Rep.* **188**, 285 (1990).